

## ABSTRACT

Title of Document: SCALE MODELING OF STRUCTURAL BEHAVIOR IN FIRE

Ming Wang, Doctor of Philosophy, 2006

Directed By: Peter C. Chang, Associate Professor, Department of Civil and Environmental Engineering

The events of September 11<sup>th</sup> showed the combined effects of fire and structural loading on a high-rise building can be disastrous. Understanding the mechanism of structural damage caused by fire will help engineers design safer infrastructures by providing adequate resistance to failure. Contemporary research in computational fluid dynamics and finite element method have produced great advances to simulate both fire and structural behaviors; however the physical and numerical complexities coupled with a lack of validation may lead to erroneous predictions. Physical modeling is inherently free of such complexities. Full-scale tests show the ability to investigate the combined effect on structures exposed to fire. However, the associated size and cost of the full-scale models are often prohibitive. Using of scaled models mitigates these problems, and it provides an economical tool to reveal weakness of structures in fire.

This dissertation gives a comprehensive study on scale modeling of steel structures in fire. The theory of both the fire and structural scaling is presented.

Design parameters of compartment fires and associated structural response are determined based on length scale relationships derived from the governing equations of heat transfer. However, not all effects can be scaled in a complex system. The strategy is to scale those parameters that are important to the behavior of the structure while the less critical effects may be allowed to deviate from the scaling rules. The use of this partial scaling strategy is developed and tested experimentally. This dissertation discusses and evaluates the accuracy of the use of scaled models in the study of the combined effects of fire and structural loading.

Experimental results show that the practical scaling rules developed in this dissertation can be used to conduct scaled structural fire tests. Similar steel temperature profiles and structural response are obtained from scaled models at different scales. Although the results are not quantitatively perfect, it is feasible to use scaled models to study fire-induced structural behaviors.

SCALE MODELING OF STRUCTURAL BEHAVIOR IN FIRE

By

Ming Wang

Dissertation submitted to the Faculty of the Graduate School of the  
University of Maryland, College Park, in partial fulfillment  
of the requirements for the degree of  
Doctor of Philosophy  
2006

Advisory Committee:

Associate Professor Peter C. Chang, Chair

Professor James G. Quintiere

Associate Professor Chung C. Fu

Assistant Professor Ricardo A. Medina

Associate Professor James A. Milke

© Copyright by  
Ming Wang  
2006

## Dedication

To Song.

To my parents.

## Acknowledgements

First and foremost, I would like to express my gratitude to my advisor and mentor, Dr. Peter Chang, for guiding and supporting me since the first day I set foot onto College Park, Maryland, US. Thank you Dr. Chang! Your insight, knowledge, and enthusiasm inspired me to explore the world of engineering.

Secondly, I am grateful to Dr. James Quintiere. Without your encouragement and support I wouldn't be where I am now.

I would like to thank my committee members Dr. Chung Fu, Dr. Ricardo Medina, Dr. James Milke for their help and time they provided on my research.

I would like to thank my friends Yunyong (Pock) Utiskul, Meng-Wah Yong and Tensei Mizukami for their tireless help on the experiment.

Thank you to Jonathan Perricone and Peter Veloo for working on the project with me and conducting compartment fires.

Supports from US National Science Foundation (under award No. 0301643) and Maryland Fire and Rescue Institute are appreciated.

I would like to express special thanks to all students in ENFP 320 Class in the fall semester of 2004 for their contribution on planning, constructing and testing of the scaled WTC model.

# Table of Contents

Dedication .....	ii
Acknowledgements .....	iii
Table of Contents .....	iv
List of Tables .....	vi
List of Figures .....	vii
Nomenclature .....	ix
Chapter 1: Introduction .....	1
1.1 Overview .....	1
1.2 Objective .....	3
1.3 Structural fire testing .....	4
1.4 Applications of scale modeling .....	7
1.5 Structural behavior in fire .....	8
1.6 Thermal response of structural members .....	11
1.7 Organization of dissertation .....	14
Chapter 2: Scale modeling of compartment fire .....	16
2.1 Background of fire scaling .....	16
2.2 Theoretical development of compartment fire scaling .....	18
2.2.1 Time scale .....	19
2.2.2 Energy equation .....	21
2.2.3 Scaling of fuel (wood cribs) .....	22
2.2.4 Scaling of compartment boundaries .....	26
2.2.5 Strategy of partial scaling .....	30
2.3 Experimental investigation of scaled compartment fires .....	32
2.3.1 Practical approaches .....	32
2.3.2 Design of wood cribs .....	34
2.3.3 Design of compartment walls .....	36
2.3.4 Experimental set-up .....	38
2.3.5 Results of scaled compartmental fires .....	41
Chapter 3: Scale modeling of structures and insulation .....	46
3.1 Theoretical development of structural scaling .....	46
3.2 Testing of scaled frames in oven .....	49
3.3 Theoretical development of insulation scaling .....	52
3.4 Numerical simulation of thermal response of insulated steel .....	56
3.5 Experimental validation of insulation scaling .....	62
3.5.1 Test of insulated steel rods .....	62
3.5.2 Test of insulated steel tubes: comparison of two approaches .....	69
Chapter 4: Scaled model experiments of structures subjected to fire and gravity load .....	76
4.1 Construction of steel frames with insulation .....	77
4.2 Experimental results of frame testing in fire .....	81
4.3 Conclusion .....	83
Chapter 5: Failure prediction by use of scaled models .....	85

5.1 Scale modeling of structural failure.....	86
5.2 Similitude relation of structural failure.....	89
5.2.1 Local buckling .....	89
5.2.2 Elastic buckling.....	90
5.2.3 Lateral torsional buckling .....	91
5.3 Similitude relation of fire, structures, and insulation.....	92
5.4 Methodology of failure prediction by using scaled models.....	94
5.5 Failure tests of beams in scaled compartment fires .....	95
5.6 Conclusion .....	99
Chapter 6: Investigation of World Trade Center Tower 1 collapse based on tests of scaled model.....	100
6.1 Construction of scaled model.....	103
6.1.1 Wood cribs and jet fuel .....	104
6.1.2 Wall and floor materials.....	106
6.1.3 Insulation on steel .....	107
6.2 Test of 1/20-scale model.....	111
6.3 Results and analysis .....	114
6.4 Conclusion and discussion.....	119
Chapter 7: Modeling of restrained steel beam in fire with consideration of local yielding .....	121
7.1 Development of local yielding and deflection .....	123
7.2 Estimation of axial boundary restraint.....	127
7.3 Simplified beam model with pseudo rotational springs.....	132
7.3.1 Beam behavior at small transverse deflection .....	132
7.3.2 Beam behavior with large transverse deflection.....	135
7.3.3 Determination of stiffness of rotational springs.....	138
7.4 Validation of simplified method .....	140
7.5 Conclusion .....	143
Chapter 8: Conclusions and future work .....	145
8.1 Conclusions.....	145
8.2 Suggestion on future work .....	147
Bibliography .....	149

## List of Tables

Table 1.1 ASTM E119 time-temperature curve .....	11
Table 2.1 Scaling rules for wood cribs design .....	26
Table 2. 2 Dimensionless groups and scaling rules for compartment boundaries.....	31
Table 2.3 Design parameters of cribs .....	35
Table 3.1 Summary of scaling rules for insulation .....	57
Table 3.2 Comparison of numerical results and application comments .....	61
Table 3.3 Relative differences of fire and steel temperature between 1/4-scale and 1/8-scale models.....	69
Table 4.1 Dimension of prototype and scaled models, and insulation applied.....	77
Table 5.1 Scaling rules for fire, insulation and structures .....	93
Table 6.1 Wall and floor materials in WTC and scaled model.....	107
Table 6.2 Insulation materials and thickness used in WTC and scaled model .....	111
Table 7.1 Estimation of axial restraints of steel beams in Figure 7.6.....	131

## List of Figures

Figure 1.1 Steel testing building at Cardington, from Kirby [3] .....	5
Figure 1.2 Open car park fire test, from Zhao and Kruppa [12].....	6
Figure 2.1 Relation between free burning rate and crib porosity, from Croce [82] ...	18
Figure 2.2 Schematic drawing of mass flow rate.....	19
Figure 2.3 Schematic drawing of momentum.....	19
Figure 2.4 Model of a compartment fire.....	21
Figure 2.5 Design of a typical wood crib.....	23
Figure 2.6 Heat loss through walls .....	28
Figure 2.7 Thermal properties of Type C Gypsum wallboard, from Harmathy [85] .	33
Figure 2.8 Geometry of the prototype compartment .....	34
Figure 2.9 Burning time of wood cribs as function of vent width and stick thickness, from Perricone [86].....	35
Figure 2.10 Thermal conductivity of Kaowool3000 and Saffil LD Mat .....	37
Figure 2.11 Dimensionless group of conduction verses temperature .....	37
Figure 2.12 Dimensionless group of thickness verses temperature.....	38
Figure 2.13 Configuration of wood cribs for small fires, from Perricone [86] .....	39
Figure 2.14 Configuration of wood cribs for large fires, from Perricone [86] .....	39
Figure 2.15 1/8-scale and 1/4-scale Compartments.....	40
Figure 2.16 Measurement set-up (front walls not installed), from Perricone [86] .....	41
Figure 2.17 Scaled compartment fires .....	42
Figure 2.18 Location of 5 typical hot gas temperature measurement points .....	42
Figure 2.19 Hot gas temperature profiles of small fires .....	43
Figure 2.20 Hot gas temperature profiles of large fires .....	44
Figure 3.1 Beam-column model .....	47
Figure 3.2 Testing of scaled frames in oven .....	50
Figure 3.3 Strain at the mid-span of the beam .....	51
Figure 3.4 Strain at the location close to the end of the beam .....	51
Figure 3.5 2-D finite element model of insulated steel.....	57
Figure 3.6 Temperature curves of full-scale and quarter-scale models .....	58
Figure 3.7 Temperature of steel in full-scale and quarter scale models .....	59
Figure 3.8 Experimental set-up of compartment fire and insulated steel column .....	63
Figure 3.9 Fire temperature profile and steel temperature in the small fire .....	67
Figure 3.10 Fire temperature profile and steel temperature in the large fire .....	68
Figure 3.11 Dimensions of cross sections of scaled tubes.....	70
Figure 3.12 Experimental set-up of scaled insulated tubes.....	71
Figure 3.13 Temperature profiles of steel tubes for small fire (Approach 1).....	72
Figure 3.14 Temperature profiles of steel tubes for small fire (Approach 2).....	73
Figure 3.15 Temperature profiles of steel tubes for large fire (Approach 1).....	74
Figure 3.16 Temperature profiles of steel tubes for large fire (Approach 2).....	75
Figure 4.1 Typical steel frame before insulation is applied.....	78
Figure 4.2 Steel frame with insulation applied .....	78
Figure 4.3 Detail of beam-to-column connection .....	79
Figure 4.4 Insulated frame placed in compartment .....	79

Figure 4.5 Vertical loading applied to frame by hanging weight .....	80
Figure 4.6 Experimental set-up of tests of steel frames.....	81
Figure 4.7 Typical steel temperature profiles in the frames, temperature vs. full-scale time .....	83
Figure 4.8 $\Delta y/L$ of steel beams vs. full-scale time.....	84
Figure 5.1 Beam model with lateral torsional buckling.....	92
Figure 5.2 Schema of methodology for failure prediction.....	95
Figure 5.3 Steel beam before and after insulation applied.....	96
Figure 5.4 Experimental set-up of failure testing .....	96
Figure 5.5 Typical hot gas temperature profiles in two compartment fires.....	98
Figure 5.6 Steel beam temperature profiles v.s. full-scale time.....	98
Figure 6.1 The 1/20-scale floor model.....	104
Figure 6.2 Wood cribs used as the fuel in the model.....	106
Figure 6.3 Schema of insulation thickness adjustment.....	109
Figure 6.4 Scaled truss and column models.....	112
Figure 6.5 Insulated structural models.....	113
Figure 6.6 Layout of locations of structures and temperature measurement.....	113
Figure 6.7 Burning of the 1/20-scale model .....	114
Figure 6.8 Upper layer hot gas temperature profiles plotted in WTC time .....	115
Figure 6.9 Floor heat flux measurement .....	116
Figure 6.10 Steel temperature profiles of long-span trusses (LT) and exterior columns (SC).....	117
Figure 6.11 Steel temperature profiles of short span truss and exterior column .....	118
Figure 7.1 3D restrained beam model and section dimension.....	124
Figure 7.2 Elastic-plastic model of steel.....	125
Figure 7.3 Beam deflection with different axial restraints .....	125
Figure 7.4 Axial forces in the beam with different axial restraints .....	125
Figure 7.5 Axial stress distribution patterns in the beam at elevated temperature ...	127
Figure 7.6 Restrained steel beam in frames.....	129
Figure 7.7 Columns and brace subjected to a horizontal force.....	130
Figure 7.8 Restrained beam model .....	132
Figure 7.9 Stress distribution on the sections at ends .....	134
Figure 7.10 Stress distribution on the section at mid-span .....	135
Figure 7.11 Beam model with pseudo springs.....	138
Figure 7.12 Flow chart of analysis of simplified beam model with pseudo springs	140
Figure 7.13 Mid-span deflection of 5 m steel beam at elevated temperature .....	142
Figure 7.14 Axial force of 5 m steel beam at elevated temperature .....	142
Figure 7.15 Mid-span deflection of 8 m steel beam at elevated temperature .....	142
Figure 7.16 Axial force of 8 m steel beam at elevated temperature .....	143

## Nomenclature

$b_w$	=	Stick thickness
$c_i$	=	Specific heat of insulation
$c_s$	=	Specific heat of steel
$c_w$	=	Specific heat of wall material
$d$	=	Beam shortening due to transverse deflection
$d_1, d_2$	=	Diameter of members
$dT$	=	Increment of temperature
$g$	=	Acceleration of gravity
$h$	=	Depth of beam
$h_c$	=	Coefficient of heat convection
$k_{1L}$	=	Stiffness of translational spring at left end of beam
$k_{1R}$	=	Stiffness of translational spring at right end of beam
$k_{2L}$	=	Stiffness of rotational spring at left end of beam
$k_{2R}$	=	Stiffness of rotational spring at right end of beam
$k_{2M}$	=	Stiffness of rotational spring at middle of beam
$k_C$	=	Stiffness of translational spring at point C
$k_i$	=	Thermal conductivity of insulation
$k_w$	=	Thermal conductivity of wall material
$m$	=	Mass
$\dot{m}$	=	Mass flow rate, burning rate of fuel
$m_i$	=	Mass of insulation
$\dot{m}_f$	=	Mass burning rate, mass loss rate of fuel (wood cribs)
$m_p$	=	Mass of steel in prototype
$m_s$	=	Mass of steel
$n_c$	=	Number of pairs of columns
$n_{br}$	=	Number of bracing members
$n_w$	=	Number of sticks per layer
$p$	=	Pressure
$\dot{q}$	=	Heat loss rate
$\dot{q}''$	=	Heat flux onto object
$\dot{q}_v$	=	Heat loss rate through vent
$\dot{q}_w$	=	Heat loss rate through walls
$\dot{q}_{w,c}$	=	Heat loss rate to walls by convection
$\dot{q}_{w,k}$	=	Heat loss rate through walls by conduction
$\dot{q}_{w,r}$	=	Heat loss rate to walls by radiation

$s$	=	Scale factor (or length scale)
$s_c$	=	Shape constant
$s_w$	=	Stick spacing
$t$	=	Time
$t_r$	=	Reference time (or cribs burning time)
$t_m$	=	Time to reach $T_m$
$u$	=	Gas flow velocity
$v$	=	Element deformation vector
$x$	=	Length in direction of beam axis
$y$	=	Beam transverse deflection
$y_{max}$	=	Maximum transverse deflection of beam
$\tilde{y}_{max}$	=	Initial guess of $y_{max}$
$A$	=	Area (or sectional area)
$A_{br}$	=	Sectional area of bracing member
$A_m$	=	Cross sectional area of scaled model
$A_p$	=	Cross sectional area of prototype
$A_s$	=	Surface area of insulated steel or a fluidal element
$A_s$	=	Exposed surface area of crib
$A_{sf}$	=	Compartment surface area exposed to fire
$A_v$	=	Vertical shafts area within crib
$A_{vent}$	=	Area of vent
$C$	=	Sectional perimeter of steel member
$C_w$	=	Material constant representing species of wood
$D$	=	Sectional perimeter of steel member
$E$	=	Elastic modulus
$E_0$	=	Elastic modulus of steel at room temperature
$E_T$	=	Elastic modulus of steel at elevated temperature
$F$	=	Force
$F_{12}$	=	Radiation view factor
$F_{br}$	=	Axial force in brace
$F_r$	=	Froude number
$I_c$	=	Moment of inertia of column
$L, L_b$	=	Length of beam
$L_{br}$	=	Length of bracing member
$L_c$	=	Length of column
$L_w$	=	Length of stick
$M, M_1, M_2$	=	Moment, moment at end 1, moment at end 2
$M_0$	=	Moment at mid-span due to external loading

$M_{1,2}$	=	Moment at ends due to external loading
$M_{tot}$	=	Total moment
$N$	=	Power of convection factor
$N_w$	=	Number of layers
$P$	=	Axial loading
$P_E$	=	Elastic buckling loading
$P_{or}$	=	Porosity factor
$\dot{Q}$	=	Heat generation rate
$R$	=	Burning rate of cribs
$R_r$	=	Free burning rate of cribs
$S$	=	Conduction shape factor
$T$	=	Temperature
$T_{1/4}$	=	Temperature measured in 1/4-scale model
$T_{1/8}$	=	Temperature measured in 1/8-scale model
$T_\infty$	=	Ambient temperature, room temperature
$T_i$	=	Mean temperature of insulation
$T_s$	=	steel temperature
$T_f$	=	hot gas temperature or fire temperature
$T_m$	=	Maximum temperature
$T_{surf}$	=	Surface temperature of insulation
$T_w$	=	Temperature of compartment walls
$V$	=	Volume
$\alpha$	=	Coefficient of thermal expansion of steel
$\alpha_s$	=	Absorption of surface
$\chi$	=	Section yielding index
$\chi_{L,R}$	=	Yielding index at end section of beam
$\chi_M$	=	Yielding index at middle section of beam
$\delta_i$	=	Thickness of insulation
$\delta_T$	=	Thermal thickness of walls
$\delta_w$	=	Thickness of walls
$\varepsilon$	=	Strain
$\varepsilon_f$	=	Emissivity of flame
$\varepsilon_g$	=	Gas emissivity
$\varepsilon_s$	=	Surface emissivity
$\varphi$	=	A tolerance
$\lambda$	=	Deflection profile factor
$\theta$	=	Angle between beam and brace
$\rho$	=	Density

$\rho_i$	=	Density of insulation
$\rho_w$	=	Density of wall material
$\rho_{wd}$	=	Density of wood
$\rho_\infty$	=	Density of air at ambient temperature
$\sigma$	=	Stress
$\sigma_g$	=	Stefan-Boltzmann constant
$\sigma_m$	=	Mechanical stress induced by gravity load
$\sigma_t$	=	Thermal induced stress
$\sigma_{tot}$	=	Total stress in a beam
$\sigma_{y,T}$	=	Yield strength of steel at elevated temperature
$\sigma_{y,20^\circ C}$	=	Yield strength of steel at 20 °C
$\tau$	=	Shear force per unit area
$\Delta$	=	Horizontal deflection
$\Delta_L$	=	Axial deflection of beam at left end
$\Delta_R$	=	Axial deflection of beam at right end
$\Delta H_f$	=	Heat of combustion of fuel (wood cribs)
$\Pi$	=	Dimensionless groups

# Chapter 1: Introduction

## 1.1 Overview

This dissertation is a comprehensive investigation of scale modeling implemented to study structural behavior in fire. Scale modeling has been widely used by engineers and researchers to predict the performance of infrastructures, such as bridges, high-rise buildings, offshore platform, and dams. Testing of scaled structural models has been proved to be efficient and economic to studying the static and dynamic behavior of structures under various loading (gravity, wind, earthquake, and ocean wave). Scale modeling applied in fire research can be found through its general history. Scaling criteria of important parameters such as fire power, heat flux, combustion product concentration involved in fire phenomena have been developed. Scaled fire experiments have been used as an effective tool to study fire behaviors under various scenarios. This research is to couple the scaling theories of both structures and fire and extend to structural fire testing at reduced scales. It provides a tool for engineers to analyze complex systems and it offers an economical way of testing that can reveal important issues involved in “structures in fire.”

This research starts with fundamentals, giving a review of scaling theory used in fire research and structural engineering, and introducing the important contribution of theoretical and experimental study of scaled compartment fires and scaled structural fire resistance testing. The theoretical part of this research consists of the compartment fires scaling and the structural scaling. Scaling rules for designing fuels,

compartment boundaries, structures, structural loading, fire-proof material on structures are developed and presented. The experimental part of this research starts with fundamental tests such as burning of wood cribs, testing of insulated steel columns so that the scaling rules are validated. One important experiment is the testing of steel framed structures in scaled fire at different scales, in which the behaviors of the spatial structures are investigated. The accuracy of using scaled models for structural fire testing is discussed. Testing of scaled steel beam models is conducted to demonstrate lateral torsional buckling failure under combined structural loading and fire loading. The feasibility of using scaled models to predict fire-induced structural failure is investigated.

A 1/20-scale model of the 96<sup>th</sup> floor of World Trade Center Tower 1 is constructed and tested based on scaling rules developed in this research. This is an example of applying small-scale models to investigate real-world disasters. This dissertation provides a detailed description of constructing and testing of the World Trade Center (WTC) floor model, and the testing results are compared to analytical results and visual evidences compiled in NIST report on the investigation of the collapse of WTC towers.

In the last part of the dissertation, a simplified method is proposed to estimate the boundary constraint of restrained steel beams in a frame structure with inclusion of bracing members. The development of local yielding in the restrained steel beam is found to play an important role for the transverse deflection and axial forces. A simplified beam model with pseudo rotational springs is introduced, and it can be used to predict the structural behavior of restrained steel beam in fire with

consideration of local yielding. The proposed beam model can be easily adopted in structural design, and it can dispense with the large computational efforts which are ineluctable in the finite element plastic zone method.

## 1.2 Objective

The testing of scaled models significantly reduces the expense from a full-scale fire and structural testing, and it eliminates limitations of studying structures under fire in laboratories where large structures under combined effect are impracticable. This research explores how to perform small scale structural fire tests while pursuing the law of similitude: while this is not entirely possible. Errors may be generated because not all effects can be scaled at the same time. The objectives of this research are to:

- provide the theory of scale modeling coupled with both structures and compartment fires,
- introduce the strategies of partial scaling and simplifying processes for practical applications,
- present scaling rules and experimental techniques which engineers and researchers can follow so as to build and test scaled models to study fire-induced structural performance,
- evaluate the accuracy of the use of scaled models in the study of the combined effect of fire and structural loading,

- understand the behavior of a restrained steel beam at elevated temperature, and propose a simplified beam model with pseudo springs to predict the development of deflection and axial force in the beam.

### 1.3 Structural fire testing

The events of September 11th showed the combined effects of fire and structural loading on a high-rise building can be disastrous. Federal Emergency Management Agency (FEMA) [1] conducted investigations to study the performance of the buildings at the World Trade Center site and developed an understanding of the response of each affected building. Recommendations on improving design guidance and tools have also been given by FEMA.

*These recommendations have a broader scope than the important issue of building concepts and design for mitigating damage from terrorist attacks, and also address the level at which resources should be expended for aircraft security, how the fire protection and structural engineering communities should increase their interaction in building design and construction, possible considerations for improved egress in damaged structures, the public understanding of typical building design capacities, issues related to the study process and future activities, and issues for communities to consider when they are developing emergency response plans that include engineering response (Federal Emergency Management Agency [1], page 4).*

Understanding the mechanism of structural damage caused by fire will help engineers design safer infrastructures by providing adequate resistance to failure. Contemporary research in computation fluid dynamics has produced great advances; however the physical and numerical complexities of combustion coupled with a lack

of validation may lead to erroneous predictions. Physical modeling is inherently free of such complexities. One of the best known experiments was the Cardington tests [2-5] which show the ability to investigate the combined effect on structures exposed to fire. An 8-storey composite framed structure was built as a platform, as shown in Figure 1.1, so that people can conduct large-scale structural testing using both “natural” fires and non-standard gas fires. The full-scale or large-scale experimental data thereby are used to validate and modify computational models [6-8] which are developed to be applied to a wider range of buildings than just composite framed structures of Cardington test building. The experimental results from the full-scale experiments along with numerical analysis results [9, 10] can build a better understanding on the behaviors of both structural response [11] and fire [5].

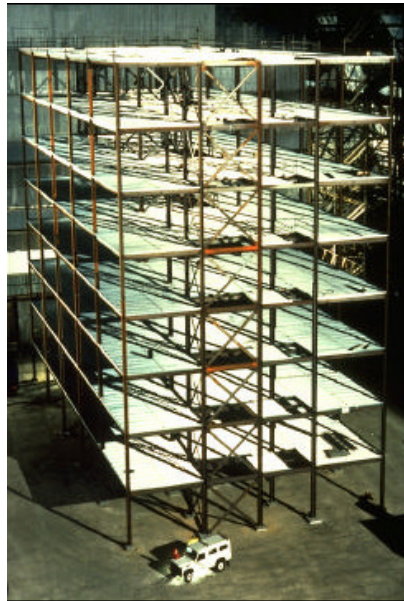


Figure 1.1 Steel testing building at Cardington, from Kirby [3]



Figure 1.2 Open car park fire test, from Zhao and Kruppa [12]

Another well-known full-scale structural fire testing is the open car park fire test [12] conducted by CTICM (France, the coordinator), ARBED (Luxembourg) and TNO (Netherlands). Cars were burned in an open car park, as shown in Figure 1.2, so that both fire behavior and structural performance were investigated. This full-scale experiment provides convincing evidence that “fire protection of the steel structure is not necessary to obtain overall stability” for this type of car park structure.

The results from this full-scale experiment are reliable since it is a reproduction of a real fire in a building. However, the associated size and cost of the full-scale or large-scale models are often prohibitive. Most researchers are limited to studying the behavior of individual structural components in a furnace instead of testing a typical spatial structure. The ASTM E119 [13] Standard Fire Test is used to evaluate the performance of a construction assembly under a controlled high temperature environment, and the corresponding test results, usually in the form of a Fire Resistance Rating (FRR), give a guideline to structural fire safety design. However, the standard fire test does not intend to predict the performance of a structural system in a real fire. It can only provide information of the relative response of constructed assemblies when they are subjected to a standard fire curve.

The current Fire Resistance Rating (FRR) based design method can not be used to predict structural behaviors in a real-world fire.

An integrated design tool is needed to predict the heating conditions in a fire, the heating process in structural members, and the response of structural systems. Sophisticated computational models are usually used for the purpose. The coupling of finite element models (e.g. ANSYS [14]) and computational fluid dynamics Modeling (e.g. FDS [15]) are capable of simulating both fire and structural behaviors. However, the computing effort and the lack of experimental validation limit their use in the practical design situations. One approach to mitigate these problems is to use scaled models to study the behavior of structures exposed to a real fire.

#### 1.4 Applications of scale modeling

Small-scale modeling in engineering research and experiments is attractive. If the scaling is done correctly, it can potentially reduce the cost of experiments significantly while providing valuable information [16-21]. For example, wind tunnel tests [22] are widely used to investigate the dynamic characteristics of wind-induced vibration of large civil infrastructures such as long-span suspension bridges, high-rise skyscrapers, and television masts. Shake tables are frequently used to study structural behavior under earthquake [23]. Although the Reynolds number is generally not possible to be scaled strictly in wind tunnel experiments, the results are still useful to predict the wind-induced load and response. Shake table tests usually give higher frequencies in small-scale models, and concrete aggregates cannot be scaled, however, the results can still reveal the dynamic characteristics of a structure. Tests of

scaled models conducted in laboratories reveal important information of how a structure performs under complex hazardous environments such as windstorm, earthquake, and fire. Possible failure scenarios and weak points in a structure can thereby be uncovered. This provides researchers and engineers an effective and economical tool to study the mechanism involved in a complex system which is usually difficult to simulate accurately with current analytical and computational tools.

Buckingham's  $\Pi$ -theorem [24] has been widely used by engineers and researchers to develop specific scaling rules for engineering applications. Scale modeling for various engineering problems can be found in references [16, 23, 25-30]. For a complex system which contains many parameters, it is usually not possible to preserve the effects of all the parameters in a scaled model. Experience and insight are necessary to identify the important parameters and those that are less critical. The strategy of partial scaling sometimes has to be used to design scaled models. The key idea of scale modeling is to obtain reasonable accuracy from practicable approaches. This is the art of scaling. This dissertation introduces some simplifying processes and the strategy of partial scaling in order to make the scaled structural fire testing practicable.

### 1.5 Structural behavior in fire

The situations of a structure exposed to fire are relatively complex since the temperature and changing boundary restraint play important roles for the stress distribution and magnitude in the structure. Steel weakens as the temperature

increases, and the properties of construction steel at elevated temperatures have been well studied. Additional stress is produced when the thermal expansion of the structure is constrained because of the boundary restraint provided by the adjacent structures. The stress in the structure is therefore increased, and at the same time, the yielding strength of the material decreases due to material degradation. This combination of loading and material degradation results in local yielding that differs from the typical yield zone created by bending moment at room temperature. This will be discussed in Chapter 7.

Many commercial softwares such as ANSYS [14], ABAQUS [31], VULCAN [32, 33], and SAFIR [34, 35] can perform the combined thermal and structural analysis. The solution obtained from these simulation packages requires the input of loading such as temperature profile, heat flow rate, heat flux, and heat generation rate, that are usually chosen by researchers according to previous empirical data and their experience. Such computational predictions must be validated by experimental data. Without experimental verification, computational tools are limited to understanding relative changes of the structures' behavior as parameters are varied.

The fundamental principles and the descriptions of the key phenomena that govern the behavior of composite framed structures in fire were presented by Usmani *et al* [36]. The key events that define the response of a steel framed structure were discussed by Usmani and Lamont [11]. Structural behavior under different heating regimes obtained by considering thermal gradient and mean temperature applied to concrete slabs was presented by Sanad *et al* [37, 38]. The structural design approach with consideration of slab/beam membrane action was presented by Bailey [39]. The

development of the research toward the use of unprotected steel structures was reviewed by Wang and Kodur [40]. Performance of unprotected steel beams and steel composite frames subjected to severe fire was examined by Wastney [41], and the question of whether thermal protection is necessary for all structures was asked. Fire resistance of structural members was investigated by conducting standard fire tests and parametric study by using validated numerical models [42, 43]. Liu *et al* [44] studied the effect of boundary restraint on steel beams at high temperature by conducting testing in a furnace. Yang *et al* [45] conducted experiments to investigate the loading capacity of fire-resisting steel columns under elevated temperature with different width-to-thickness ratios. The performance of steel connections in fire was studied by experiments and computational modeling [46, 47]. Numerical and analytical modeling has been developed to predict structural performance in fire for various structural types: steel frames [48-54], concrete structures [55, 56], composite [57-59], masonry structures [60], connections [61].

Complex numerical modeling is not easy to be adopted in engineering practice because of its complexity. For example, the finite element plastic zone method is usually used to obtain the development of local yielding in a structure. However, this method requires fine meshes in the structural model and nonlinear analysis. In Chapter 7, a simplified beam model with pseudo springs is proposed. It can be used to predict deflections and axial forces in a restrained beam at elevated temperature with only linear analysis. Other simplified methods such as [62, 63] are favorable in structural design to predict structural behaviors in fire.

## 1.6 Thermal response of structural members

Standard fire curves have been used as the thermal environment input for structural members in fire testing. ASTM E119 [13] curve is one of the most widely used specification for structural fire-resistant tests. It is defined by a number of discrete points, as shown in Table 1.1. This curve can also be obtained approximately by the equation [64] :

$$T = 750[1 - e^{-3.79553\sqrt{t}}] + 170.41\sqrt{t} + T_{\infty} \quad (1.1)$$

where  $t$  is time in hour. Slight difference exists among standard fire curves of different countries, but they are defined in a similar way. The use of standard fire curves is not intended to represent a real fire environment. The standard fire curves do not take into account important factors involved in a compartment fire such as geometries, ventilation, fuel load, and boundary properties. These temperature profiles provide a testing standard so that the relative thermal response of structural members can be compared.

Table 1.1 ASTM E119 time-temperature curve

Time ( <i>minutes</i> )	ASTM E119 Temperature ( $^{\circ}$ C)
0	20
5	538
10	704
30	843
60	927
120	1010
240	1093
480	1260

Reliable structural fire safety analysis requires more realistic and accurate fire input. Barnett [65] proposed a “natural fire curve,” BFD curve. It is defined as:

$$T = T_{\infty} + T_m e^{-\kappa} \quad (1.2)$$

where  $\kappa = (\log t - \log t_m)^2 / s_c$ .  $T_{\infty}$  is the ambient temperature.  $T_m$  is the maximum temperature.  $t_m$  is the time to reach  $T_m$ .  $s_c$  is the shape constant that is related to the dimensions of the compartment. Therefore, the determination of a natural fire curve depends on the values of  $T_{\infty}$ ,  $T_m$ ,  $t_m$  and  $s_c$  which can be obtained by analyzing a specific fire scenario. This provides engineers with a tool to establish a natural fire for design purposes. Another parametric temperature-time curve for compartment fire can be found in Eurocode [66], and the fire curve depends on the input of enclosure area, opening height, and thermal properties of compartment boundaries.

Lennon and Moore [5] discusses the natural fire safety concept by analyzing the fire temperature measured from full-scale tests at Cardington. The improved method to characterize a natural fire can help engineers predict structural responses under a specific fire more accurately.

Milke [67] gave an overview of engineering methods to evaluate fire resistance of structural members. Numerous research has been carried out to study thermal response of structural members exposed to fires. Wickstrom [68] discuss the fundamental heat transfer concept in fire testing, and recommendations on how to define and measure heat transfer in fire testing were given. Lamont *et al* [69] used a finite element heat transfer model, HADAPT [70], to simulate the heat transfer in the composite steel and concrete slabs, and the predicted structural temperature compared

to the measured temperature from large compartment fire tests. The overprediction of steel temperature was found to be due to the inadequacy of a modeling moisture vaporization. Study on heat transfer in insulated steels was conducted in [71, 72], and improved approaches were proposed for engineering design. Wang [73] conducted investigation of a strategy of applying partial fire protection to composite beams. Wickstrom and Hadziselimovic [74] presented a theoretical analysis of expressing a thermal protection layer on a concrete structure in terms of an equivalent concrete layer, and the finite element temperature analysis computer program, TASEF [75], was used for the analyses. Ryder et al [76] conducted investigation of the fire resistance reduction due to thermal insulation loss by using FIRES-T3 [77]. Structural behavior caused by two different compartment fire scenarios (“long-cool” and “short-hot”) were investigated by Lamont *et al* [78] by using finite element analyses. Those analyses of heat transfer help us build better understanding on the effects of structural geometries, thermal insulation on structures, and different fire behaviors.

Fire tests are always needed to validate computer models. With consideration of reduced cost and ease of operation, small-scale fire tests are alternatives to full-scale tests if the scaling relations can be properly formed. Fire in a scaled compartment model should be representative to a full-scale compartment fire. Structural temperature should be independent of scales. So the thermal insulation on structures must be determined appropriately so that the effect of heat transfer in structural members is similar to that of the prototype. This requires the development of the scaling theory of both fire and structure.

## 1.7 Organization of dissertation

In this dissertation, Chapter 1 gives an overview of the background on structural fire testing, scale modeling and structural response to fire. The motivation and objectives of the research are presented. Chapter 2 of the dissertation gives detail description of scale modeling of compartment fire. Scaling rules of the design parameters for wood cribs and compartments are developed. Tests of scaled compartment fires at two scales are conducted to validate the proposed scaling rules. Chapter 3 presents the development of scale modeling for structures and fire-proof materials. Practical approaches are introduced and their accuracies are compared by both numerical and experimental results. In Chapter 4, tests of insulated steel frames at two scales are conducted. The accuracy of using scaled models is evaluated by comparing both the thermal and structural responses under fires. Chapter 5 focuses on the discussion of failure prediction by using scaled models. The failure criteria and similitude relations of important parameters involved in a fire-induced failure are discussed. Chapter 6 shows an example of using a scaled model to investigate a real-world disaster: the collapse of World Trade Center (WTC) Tower 1. The 1/20-scale model of the 96<sup>th</sup> floor in WTC1 is designed based on the scaling theory and practical approaches discussed in Chapters 2, 3, 4, and 5. The accuracy of the scaled test is evaluated by comparing the testing results to analytical results and visual evidences compiled in the NIST report on the investigation of the collapse of WTC towers [79]. Chapter 7 proposes a simplified beam model with pseudo springs which can be used to predict the structural behavior of a restrained steel beam exposed to fire. The simplified model eliminates the complexity of nonlinear analysis (*i.e.*, finite element

plastic zone method) while it can still simulate the effect of the gradual local yielding in the restrained beam. Moreover, the catenary action of the beam can be captured in the proposed simplified model.

## Chapter 2: Scale modeling of compartment fire

### 2.1 Background of fire scaling

Gross and Robertson [80] of the National Bureau of Standards were one of the first researchers to conduct experiments to scale wood crib fires in enclosures. Their attempt was based on matching the Froude number because they recognized that the fire plume flow was governed by the buoyancy force [80]:

$$F_r = \frac{u}{\sqrt{gs}} \quad (2.1)$$

It was recognized that the gas flow velocity ( $u$ ) is proportional to the square root of the length scale ( $s$ ). In their experiment, the scaling rules applied in the design phase were basically geometric relationships, and the same compartment wall material was used for all scales. The results obtained from different scales did not compare well because other important factors involved in a compartment fire such as ventilation condition and boundaries were not taken account of.

A more thorough investigation of scaling of wood crib fires in enclosures was undertaken by Heskestad [81] by using the theory of burning of densely packed cribs developed by Block [82]. The burning rate of wood crib fires was found to be related to the flow rate of air through the internal structure of wood cribs. Porosity factor of wood cribs,  $P_{or}$ , was defined, and it is the function of the exposed surface area of crib ( $A_s$ ), vertical shafts area within crib ( $A_v$ ), stick spacing ( $s_w$ ) and stick thickness ( $b_w$ ) [81]:

$$P_{or} = \left( \frac{A_v}{A_s} \right) s_w^{1/2} b_w^{1/2} \quad (2.2)$$

The free burning rate of wood cribs was found to be related to porosity factor:

$$\frac{R_r}{A_s b_w^{1/2}} = f(P_{or}) \quad (2.3)$$

Experimental data [83] demonstrated this relation as shown in Figure 2.1. This provided a fundamental knowledge to design wood cribs for compartment fires at different scales. Recognizing the importance of the heat loss through vents and enclosure boundaries, Heskestad [81] suggested the scaling for the material properties of the compartment walls, and the scaling rules were derived from the governing equation of conduction in walls. The time scale they used was defined as the fire duration which was determined from the burning rate of wood cribs [81]:

$$t_r = \frac{m}{R} \sim b_w^{3/2} \quad (2.4)$$

That means the time scale relies on the scaling of crib stick thickness. This time scale will not be suitable in a transient system where time scale is the most fundamental relation. The change of all other parameters is mapped to the time scale. Therefore, the scale relation of time needs to be determined first so that it can be used to determine the scale relations of other parameters. In this research, the time scale is derived from the fundamental physics concept of fluid flow.

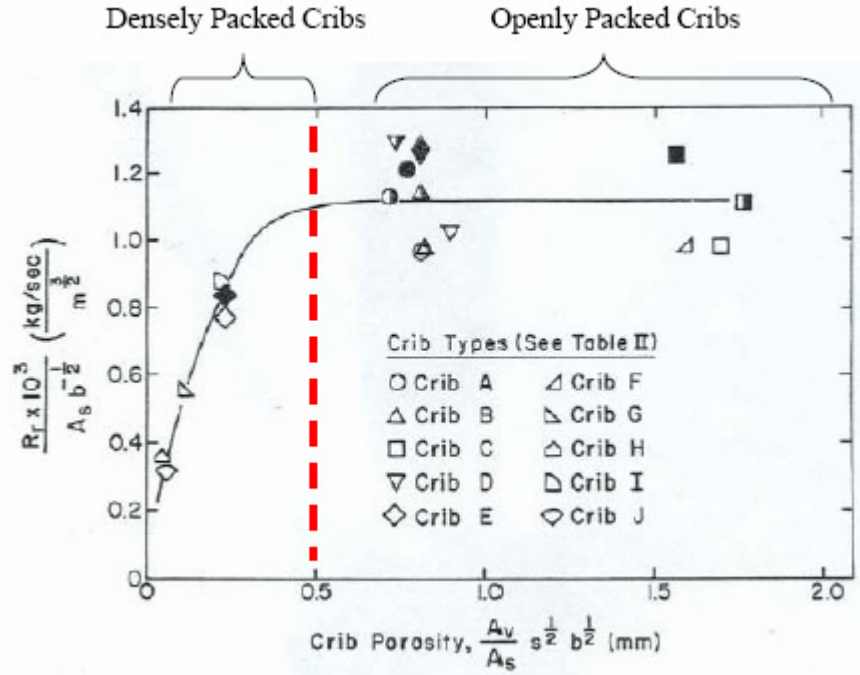


Figure 2.1 Relation between free burning rate and crib porosity, from Croce [83]

## 2.2 Theoretical development of compartment fire scaling

Dimensional analysis will be used in this research to develop the scale relations of important parameters involved in fire phenomena. In this dissertation, “~” is used to denote dimensional equality, and “^” is used to denote dimensionless

variable. Dimensionless variables are expressed as a ratio form, for example,  $\hat{T} = \frac{T}{T_\infty}$ ,

$\hat{\rho} = \frac{\rho}{\rho_\infty}$ , and  $\hat{t} = \frac{t}{t_r}$  represent the dimensionless temperature, density and time,

respectively.  $s$  is the scale factor, or the geometric length scale, *i.e.*, ratio of prototype to scale model length scale.

### 2.2.1 Time scale

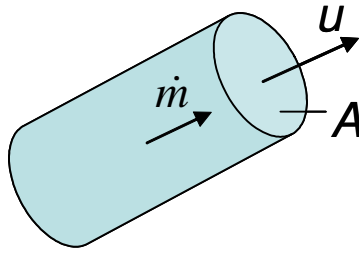


Figure 2.2 Schematic drawing of mass flow rate

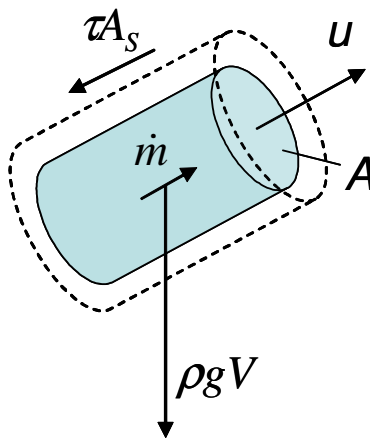


Figure 2.3 Schematic drawing of momentum

Mass flow rate of a fluid element as shown in Figure 2.2 can be defined as:

$$\dot{m} = \rho u A \quad (2.5)$$

Consider a form of the vertical momentum equation with a buoyancy term and the pressure, the conservation of momentum can be expressed as:

$$\rho V \frac{du}{dt} + \dot{m} u \sim (\rho - \rho_\infty) g V + p A + \tau A_s \quad (2.6)$$

as shown in Figure 2.3. In a natural convection condition where there is no forced flow, the hot gas flow is driven by the buoyancy which is induced by the change of

hot gas density. The pressure in the compartment is nearly constant. So the momentum flux term can be related to the buoyancy force:

$$\dot{m}u \sim (\rho - \rho_{\infty})gV \quad (2.7)$$

By using the perfect gas law under constant pressure ( $\frac{\rho - \rho_{\infty}}{\rho_{\infty}} = \frac{T - T_{\infty}}{T_{\infty}}$ ) and the definition of mass flow rate in Equation (2.5), Equation (2.7) can be written in terms of the length scale,  $s$ ,:

$$\rho u^2 s^2 \sim \frac{T - T_{\infty}}{T_{\infty}} \rho_{\infty} g s^3 \quad (2.8)$$

So the scale relation for mass flow velocity can be obtained:

$$u \sim \sqrt{gs} \quad (2.9)$$

Furthermore, equating the momentum term with buoyancy gives a time scale:

$$t \sim \sqrt{\frac{s}{g}} \Rightarrow t \sim s^{1/2} \quad (2.10)$$

This time scale is different from the characteristic time used by Heskestad [81] and Croce [83, 84] in which time scale is derived from the burning time of wood cribs ( $t \propto b^{3/2}$ ,  $b$  is stick thickness of wood crib). In this research, the time scale is derived based on the fundamental physics concept. This time scale is the basic scaling relation used to develop scaling rules governed in a compartmental fire.

## 2.2.2 Energy equation

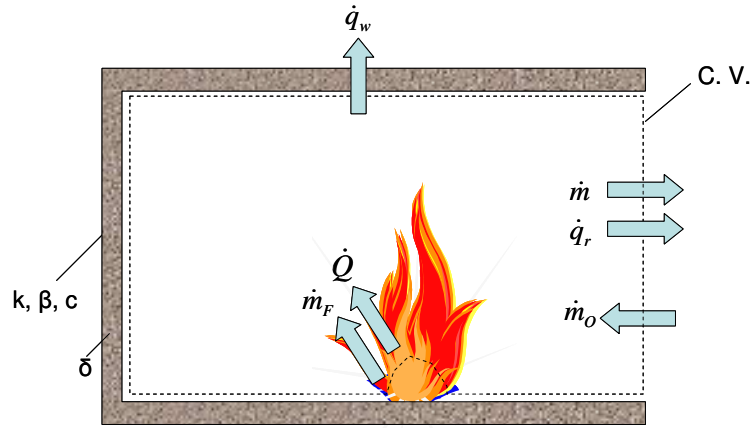


Figure 2.4 Model of a compartment fire

The model depicted in Figure 2.4 shows the fire phenomenon in a compartment. The model displays the fire burning in the compartment with a room vent. The hot gas temperature in the compartment is dependent on the difference between the heat generation rate from the fire ( $\dot{Q}$ ) and the heat loss rate through the compartment boundaries ( $\dot{q}$ ). This relation is expressed in the energy conservation equation:

$$\rho_{\infty} c_p V \frac{dT}{dt} + \dot{m} c_p (T - T_{\infty}) \sim \dot{Q} - \dot{q} \quad (2.11)$$

Making Equation (2.11) dimensionless,

$$\rho_{\infty} c_p \hat{V} s^3 \frac{d\hat{T} T_{\infty}}{d\hat{t} \sqrt{s/g}} + \frac{d\hat{\rho} \rho_{\infty}}{d\hat{t} \sqrt{s/g}} c_p (\hat{T} T_{\infty} - T_{\infty}) \sim \hat{Q} - \hat{q} \quad (2.12)$$

where  $\hat{V} = \frac{V}{s^3}$  since the compartment dimension is geometrically scaled. Equation

(2.12) can be written as:

$$\hat{V} \frac{d\hat{T}}{d\hat{t}} + \frac{d\hat{\rho}}{d\hat{t}} \hat{V} (\hat{T} - 1) \sim \frac{\dot{Q}}{\rho_{\infty} c_p T_{\infty} \sqrt{g} s^{5/2}} - \frac{\dot{q}}{\rho_{\infty} c_p T_{\infty} \sqrt{g} s^{5/2}} \quad (2.13)$$

So two dimensionless groups ( $\Pi$  terms) can be obtained:

$$\Pi_{gen} = \frac{\dot{Q}}{\rho_{\infty} c_p T_{\infty} \sqrt{g} s^{5/2}} \quad (2.14)$$

$$\Pi_{los} = \frac{\dot{q}}{\rho_{\infty} c_p T_{\infty} \sqrt{g} s^{5/2}} \quad (2.15)$$

Since the acceleration of gravity ( $g$ ) is not practicable to change and  $g \sim s^0$ , the heat generation rate and heat loss rate are scaled according to

$$\dot{Q} \sim s^{5/2} \quad (2.16)$$

$$\dot{q} \sim s^{5/2} \quad (2.17)$$

### 2.2.3 Scaling of fuel (wood cribs)

The heat generation rate can be expressed as a product of the mass burning rate of the fuel and its heat of combustion:

$$\dot{Q} \approx \dot{m}_f \Delta H_f \quad (2.18)$$

If similar fuel is used in the models ( $\Delta H_f \sim s^0$ ), the mass burning rate of the fuel should be scaled according to:

$$\dot{m}_f \sim s^{5/2} \quad (2.19)$$

Equation 2.19 provides a basis to determine the fuel in scaled models. Wood cribs are considered as the fuel for scaled models in this research because the burning of wood cribs is able to represent the burning of contents in a building room in which wood furniture is considered as the main combustible material. According to Block's

theoretical model [82], the burning rate of wood cribs can be related to the design parameters:

$$\dot{m}_f = C_w A_s b_w^{-1/2} \quad (2.20)$$

$C_w$  is a material constant representing the species of wood. This relation is only suitable for the burning of openly packed cribs. As shown in Figure 2.1, the burning rate of the cribs remains relatively constant when the porosity factor ( $P_{or}$ ) is bigger than 0.5. The regime with  $P_{or} > 0.5$  is defined as the burning of openly packed cribs, and the regime with  $P_{or} < 0.5$  is defined as the burning of densely packed cribs. Only openly packed wood cribs are considered in this research in order to simplify the relation between the burning rate and the configuration of cribs. Therefore, Equation 2.20 can be applied in the design of cribs.

Figure 2.5 shows a typical wood crib, and its design parameters are stick length ( $L_w$ ), stick thickness ( $b_w$ ), spacing between sticks ( $s_w$ ), number of layers ( $N_w$ ) and number of sticks per layer ( $n_w$ ). For each stick, its cross section is assumed to be square. The total surface area of a wood crib can be expressed as:

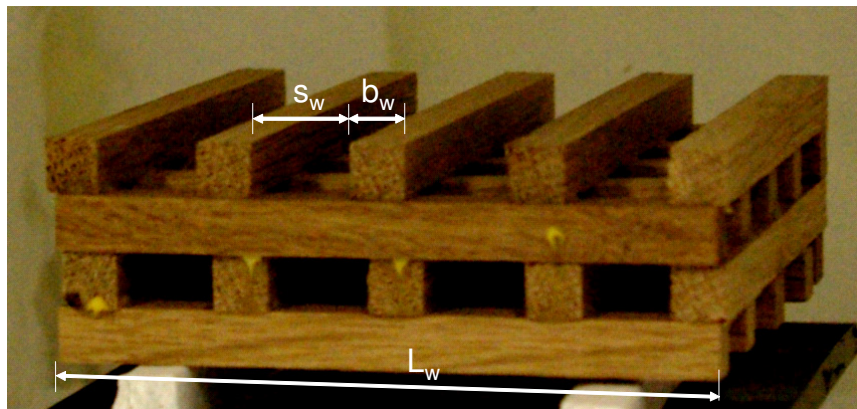


Figure 2.5 Design of a typical wood crib

$$A_s = (4b_w L_w N_w n_w + 2N_w n_w b_w^2) - (2n_w^2 b_w^2 + 2(N_w - 2)n_w^2 b_w^2) \quad (2.21)$$

Furthermore, it can be written in terms of  $4b_w L_w N_w n_w$ :

$$A_s = 4b_w L_w N_w n_w \left( 1 + \frac{b_w}{2L_w} \left( 1 + \frac{n_w}{N_w} - n_w \right) \right) \quad (2.22)$$

From Equation 2.22, the relation between  $A_s$  of a wood crib and its design parameters can be approximately written as:

$$A_s \propto b_w L_w N_w n_w \quad (2.23)$$

From Equation 2.19, 2.20 and 2.23, the following relation can be obtained:

$$b_w^{1/2} L_w N_w n_w \sim s^{5/2} \quad (2.24)$$

since  $C_w \sim s^0$ . Write the design parameters of wood crib in the form of powers of  $s$

(i.e.,  $b_w \sim s^{b'}$ ,  $L_w \sim s^{L'}$ ,  $N_w \sim s^{N'}$  and  $n_w \sim s^{n'}$ ):

$$s^{b'/2} s^{L'} s^{N'} s^{n'} \sim s^{5/2} \quad (2.25)$$

So, the algebra equation for calculating the powers can be written as:

$$b'/2 + L' + N' + n' = 5/2 \quad (2.26)$$

The vertical shaft area can be written as:

$$A_v = (L_w - n_w b_w)^2 \quad (2.27)$$

Substitute Equation 2.23 and 2.27 into Equation 2.2,

$$\frac{(L_w - n_w b_w)^2 s^{1/2} b_w^{1/2}}{b_w L_w N_w n_w} \sim P \quad (2.28)$$

By preserving the porosity factor ( $P_{or}$ ), two more algebra equations can be obtained:

$$2L' + s'/2 = 5/2 \quad (2.29)$$

$$2b' + 2n' + s'/2 = 5/2 \quad (2.30)$$

The burning time of a wood crib can be written as the ratio of the total wood mass and the mass burning rate:

$$t_r = \frac{m_f}{\dot{m}_f} \sim s^{1/2} \quad (2.31)$$

The total mass of a wood crib can be written in terms of the design parameters:

$$m_f = N_w n_w b_w^2 L_w \rho_{wd} \quad (2.32)$$

Substitute Equation 2.32, 2.20, 2.23 into Equation 2.21,

$$\frac{N_w n_w b_w^2 L_w \rho_{wd}}{C_w b_w L_w N_w n_w b_w^{-1/2}} \sim s^{1/2} \Rightarrow \frac{b_w^{3/2} \rho_{wd}}{C_w} \sim s^{1/2} \quad (2.33)$$

If the similar fuel is used in the scaled model as that of prototype ( $C_w \sim \rho_{wd} \sim s^0$ ),

the value of  $b'$  can be determined ( $b_w \sim s^{b'}$ ):

$$b' = 1/3 \quad (2.34)$$

The length of wood sticks,  $L_w$ , can be written in terms of  $b_w$  and  $s_w$  by

looking at the geometry of a wood crib as shown in Figure 2.5:

$$L_w = n_w b_w + (n_w - 1) s_w \quad (2.35)$$

From Equation 2.35, the last algebra equation for calculating the values of

$b', s', L', N'$ , and  $n'$  can be obtained:

$$b' = s' \quad (2.36)$$

Five equations have been formed to determine the five unknowns:

$$\begin{cases} b'/2 + L' + N' + n' = 5/2 \\ 2L' + s'/2 = 5/2 \\ 2b' + 2n' + s'/2 = 5/2 \\ b' = 1/3 \\ b' = s' \end{cases} \quad (2.37)$$

The solution of Equation 2.37 is:  $b' = 1/3$ ,  $s' = 1/3$ ,  $L' = 7/6$ ,  $b' = 1/3$ ,  $N' = 1/3$  and  $n' = 5/6$ . So the scaling rules for the design parameters of wood cribs are shown in Table 2.1.

Table 2.1 Scaling rules for wood cribs design

Design parameters	Scaling rules
Thickness of wood sticks, $b_w$	$b_w \sim s^{1/3}$
Spacing between wood sticks, $s_w$	$s_w \sim s^{1/3}$
Length of wood sticks, $L_w$	$L_w \sim s^{7/6}$
Number of layers, $N_w$	$N_w \sim s^{1/3}$
Number of wood sticks per layer, $n_w$	$n_w \sim s^{5/6}$

#### 2.2.4 Scaling of compartment boundaries

The heat loss rate ( $\dot{q}$ ) is determined by the boundary conditions of a compartment fire. The scaling relation of the heat loss rate in Equation 2.17 ( $\dot{q} \sim s^{5/2}$ ) will be the basis to determine the design parameters of compartment boundaries. The heat loss through the compartment boundaries consists of the heat loss through ventilation by radiation,  $\dot{q}_v$ , and heat loss through walls,  $\dot{q}_w$ .

$$\dot{q} = \dot{q}_v + \dot{q}_w \quad (2.38)$$

#### Heat loss through vent

Considering a control volume of the enclosure gas phase as shown in Figure 2.4, the heat loss through vent by radiation can be expressed as:

$$\dot{q}_v = A_{vent} \sigma_g \left[ \varepsilon_g (T^4 - T_\infty^4) + (1 - \varepsilon_g) (T_w^4 - T_\infty^4) \right] \quad (2.39)$$

where  $A_{vent}$  is the area of vent,  $\varepsilon_g$  is the gas emissivity,  $\sigma_g$  is the Stefan-Boltzmann constant,  $T_w$  is the temperature of compartment walls. If the walls in fire is assumed to be blackbodies, the gas emissivity can be written as [85]:

$$\varepsilon_g \sim 1 - e^{-\kappa s} \quad (2.40)$$

where  $\kappa$  is the absorption coefficient of gas. Substitute Equation 2.40 into Equation 2.39,

$$\dot{q}_v \sim A_{vent} \left[ (T^4 - T_\infty^4) + e^{-\kappa s} (T_w^4 - T_\infty^4) \right] \quad (2.41)$$

If the heat loss rate through vent is scaled ( $\dot{q}_v \sim s^{5/2}$ ), both the area of vent and the absorption coefficient of gas should be scaled. However, the same fuel (wood cribs) will be used in scaled models, so it is difficult to scale  $A_{vent}$  and  $\kappa$  so as to maintain  $\dot{q}_v \sim s^{5/2}$ .

The compartment model considered in this research is an enclosure with a small vent. Therefore, the heat loss through the vent by radiation is considered to be small compared to the heat loss through the compartment walls. The strategy in this research is to preserve the most important factors involved in a compartment fire, and the heat loss through vent by radiation is not preserved. For a fire burning in an open space or in an enclosure with large vent, the scaling rules for  $A_{vent}$  and  $\kappa$  need to be obtained.

### **Heat loss through compartment walls**

The heat loss through compartment walls can be described in Figure 2.6. Heat is transferred to the exposed surface of walls via the parallel paths of both radiation

and convection. The heat loss is then transferred through the walls and lost to the ambient environment.

$$\dot{q}_w = \dot{q}_{w,k} = \dot{q}_{w,r} + \dot{q}_{w,c} \quad (2.42)$$

$\dot{q}_{w,k}$  is the heat loss rate through walls by conduction.  $\dot{q}_{w,r}$  and  $\dot{q}_{w,c}$  are the heat loss rate to walls by radiation and convection, respectively.

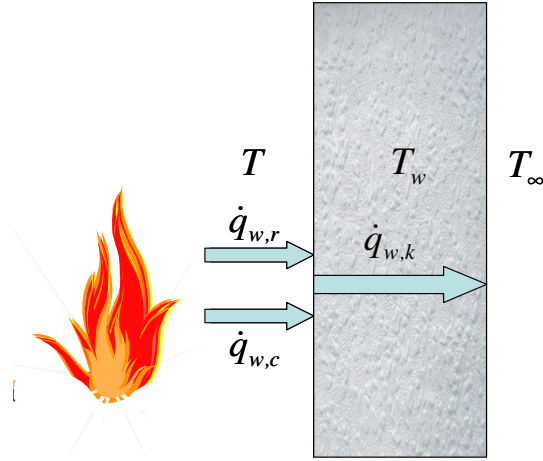


Figure 2.6 Heat loss through walls

The total heat loss through compartment boundaries is the summation of the heat loss through vent and the heat loss through walls. As stated previously, the heat loss through vent is considered to be small comparing to the heat loss through walls for a compartment with a small vent. So the scaling rules can be obtained:

$$\dot{q} \approx \dot{q}_w = \dot{q}_{w,k} = \dot{q}_{w,r} + \dot{q}_{w,c} \Rightarrow \dot{q}_w \sim \dot{q}_{w,k} \sim (\dot{q}_{w,r} + \dot{q}_{w,c}) \sim s^{5/2} \quad (2.43)$$

Consider the heat loss by conduction:

$$\dot{q}_{w,k} \sim \frac{k_w}{\delta_T} A_{sf} (T_w - T_\infty) \quad (2.44)$$

where  $k_w$  is the thermal conductivity of walls,  $A_{sf}$  is the surface area exposed to fire.

$\delta_T$  is a thermal thickness. If the compartment wall is thermally thin,  $\delta_T = \delta_w$  can be

used.  $\delta_w$  is the thickness of compartment walls. If the wall is thermally thick,  $\delta_T$  can be written as [85]:

$$\delta_T \sim \left[ \left( \frac{k_w}{\rho_w c_w} \right) t \right]^{1/2} \quad (2.45)$$

Substitute Equation 2.45 into Equation 2.44, and use the scaling rules in Equation 2.43,

$$\dot{q}_{w,k} \sim \frac{k_w}{\left[ \left( \frac{k_w}{\rho_w c_w} \right) t \right]^{1/2}} A_{sf} (T_w - T_\infty) \sim (k_w \rho_w c_w)^{1/2} s^{7/4} \sim s^{5/2} \quad (2.46)$$

as the compartment is geometrically scaled ( $A_{sf} \sim s^2$ ), and  $t \sim s^{1/2}$ . Therefore, by preserving the effect of conduction the design parameters of compartment boundaries can be scaled according to:

$$k_w \rho_w c_w \sim s^{3/2} \quad (2.47)$$

Equation 2.44 and 2.45 can also be substituted into Equation 2.15 to obtain a dimensionless group ( $\Pi$  term):

$$\Pi_{w,k} = \frac{(k_w \rho_w c_w)^{1/2} s^2 T_\infty}{\rho_\infty c_p T_\infty \sqrt{g} s^{5/2}} \sim \frac{\text{conduction}}{\text{enthalpy flow}} \quad (2.48)$$

Next, let's look at the heat loss by convection:

$$\dot{q}_{w,c} \sim h_c A_{sf} (T - T_w) \quad (2.49)$$

where  $h_c$  is the heat convection coefficient.  $h_c$  needs to be scaled according to

$$h_c \sim s^{1/2} \quad (2.50)$$

if  $\dot{q}_{w,c}$  is preserved ( $\dot{q}_{w,c} \sim s^{5/2}$ ). Similarly, a dimensionless group can also be obtained

by substituting Equation 2.49 into Equation 2.15:

$$\Pi_{w,c} = \frac{h_c s^2 T_\infty}{\rho_\infty c_p T_\infty \sqrt{g} s^{5/2}} \sim \frac{\text{convection}}{\text{enthalpy flow}} \quad (2.51)$$

The heat loss rate by radiation can be written as:

$$\dot{q}_{w,c} \sim A_{sf} \sigma_g \varepsilon_g (T^4 - T_w^4) \quad (2.52)$$

Substitute Equation 2.52 into Equation 2.15,

$$\Pi_{w,r} = \frac{s^2 \sigma_g \varepsilon_g T_\infty^4}{\rho_\infty c_p T_\infty \sqrt{g} s^{5/2}} \sim \frac{\text{radiation}}{\text{enthalpy flow}} \quad (2.53)$$

Preserving  $\Pi_{w,r}$  gives scaling rules:

$$\varepsilon_g \sim s^{1/2} \text{ or } T_\infty \sim s^{1/6} \quad (2.54)$$

The dimensionless groups for wall thickness can be written as:

$$\Pi_{w,\delta} = \frac{\delta_w}{\left[ \left( \frac{k_w}{\rho_w c_w} \right) s^{1/2} \right]^{1/2}} \sim \frac{\text{wall thickness}}{\text{thermal thickness}} \quad (2.55)$$

Four dimensionless groups can be preserved to determine the boundaries in a scaled compartment fire:  $\Pi_{w,k}$ ,  $\Pi_{w,c}$ ,  $\Pi_{w,r}$  and  $\Pi_{w,\delta}$ .

### 2.2.5 Strategy of partial scaling

Complete scaling requires preserving all the four dimensionless groups in Equation 2.48, 2.51, 2.53 and 2.55, as summarized in Table 2. 2. The preservation of conduction calls for the change of wall materials. The preservation of convection calls for the change of heat convection coefficient, but this is difficult to implement. The preservation of radiation requires either a change of gas emissivity or a change of ambient temperature. Changing ambient temperature is possible. However, if the

scale factor is relatively small, (*i.e.*,  $s = 1/8$  and  $T_\infty = 25^\circ C$ , the ambient temperature in a 1/8-scale model needs to be changed to  $(1/8)^{1/6}(273+25)K = 211K = -62^\circ C$ ). This is very difficult to obtain in typical lab environment. Changing gas emissivity is possible by using different fuels in scaled models. However, similar fuel is assumed to be used in scaled models when the scaling rules for wood cribs design are derived. Instead, the strategy of partial scaling is employed.

Table 2. 2 Dimensionless groups and scaling rules for compartment boundaries

Dimensionless groups	Scaling rules	Application
$\Pi_{w,k} = \frac{(k_w \rho_w c_w)^{1/2} s^2 T_\infty}{\rho_\infty c_p T_\infty \sqrt{g} s^{5/2}} \sim \frac{\text{conduction}}{\text{enthalpy flow}}$	$k_w \rho_w c_w \sim s^{3/2}$	Change wall material
$\Pi_{w,c} = \frac{h_c s^2 T_\infty}{\rho_\infty c_p T_\infty \sqrt{g} s^{5/2}} \sim \frac{\text{convection}}{\text{enthalpy flow}}$	$h_c \sim s^{1/2}$	Change gas flow
$\Pi_{w,r} = \frac{s^2 \sigma_g \varepsilon_g T_\infty^4}{\rho_\infty c_p T_\infty \sqrt{g} s^{5/2}} \sim \frac{\text{radiation}}{\text{enthalpy flow}}$	$\varepsilon_g \sim s^{1/2}$ or $T_\infty \sim s^{1/6}$	Change fuel or ambient temperature
$\Pi_{w,\delta} = \frac{\delta_w}{\left[ \left( \frac{k_w}{\rho_w c_w} \right) s^{1/2} \right]^{1/2}} \sim \frac{\text{wall thickness}}{\text{thermal thickness}}$	$\delta_w \sim \left( \frac{k_w}{\rho_w c_w} \right)^{1/2} s^{1/4}$	Adjust thickness

The key idea of using scaled models to represent a prototype is to develop practicable approaches by preserving the important factors so that a reasonable accuracy can be obtained. In order to make the partial scaling, it is necessary to identify dominant effects and those that are negligible under typical conditions. This

requires insight and experience on the governing factors in engineering problems. In the scaling of compartment boundaries, the heat loss through vent can be insignificant comparing to the heat loss through compartment walls. This assumption is appropriate because the compartment model considered in this research is an enclosure with very small vent. If the vent is relatively large or if the fire is burning in an open space, this assumption is no longer proper, and the heat loss through vent must be taken into account.

Preserving  $\Pi_{w,c}$  and  $\Pi_{w,r}$  leads to practical difficulties. In a compartment fire model as illustrated in Figure 2.6, the effect of conduction is the biggest thermal resistor for heat transferring through compartment walls. Therefore, the strategy of partial scaling is to preserve the conduction effect,  $\Pi_{w,k}$ , and  $\Pi_{w,c}$  and  $\Pi_{w,r}$  are allowed to vary between models and prototype.

## 2.3 Experimental investigation of scaled compartment fires

### 2.3.1 Practical approaches

“Small fire” and “large fire” scenarios are considered in this research. “Small fire” is defined as a fire with 15-*minute* burning time, and “large fire” is defined as a fire with 60-*minute* burning time. The burning time is defined as the duration between starting of the fire to the time at which flame is not visible. Experiments at two scales (1/8 and 1/4) are designed. The prototype is a building room with 3.7m×3.7m floor and 2.44 m height (inside dimensions). The wall material of the prototype is assumed to be Type C Gypsum wallboard, and its thermal properties are shown in Figure 2.7.

Its density is  $678 \text{ kg/m}^3$ . The thickness of the compartment walls in the prototype is  $15.9 \text{ mm}$ . The vent width of the prototype is  $0.5 \text{ m}$ , and the height of the vent is  $2.44 \text{ m}$ .

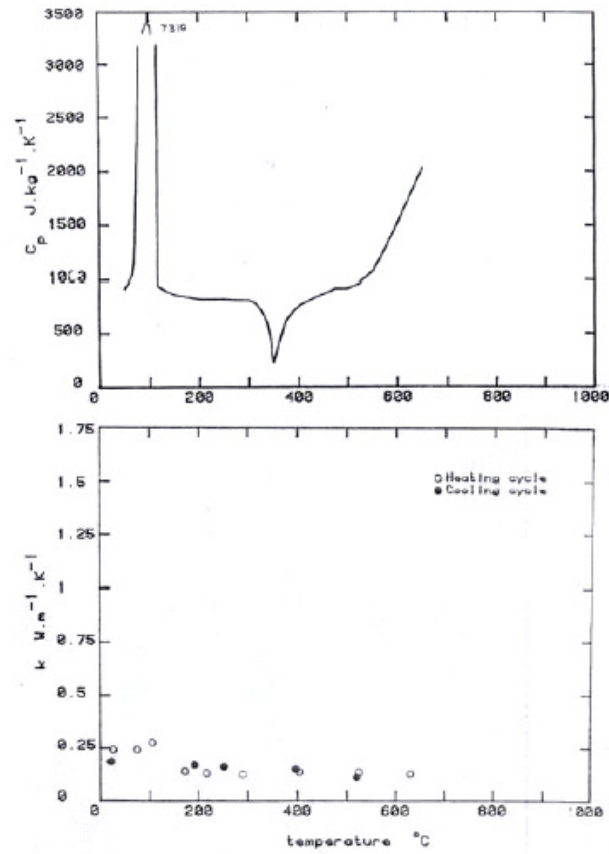


Figure 2.7 Thermal properties of Type C Gypsum wallboard, from Harmathy [86]

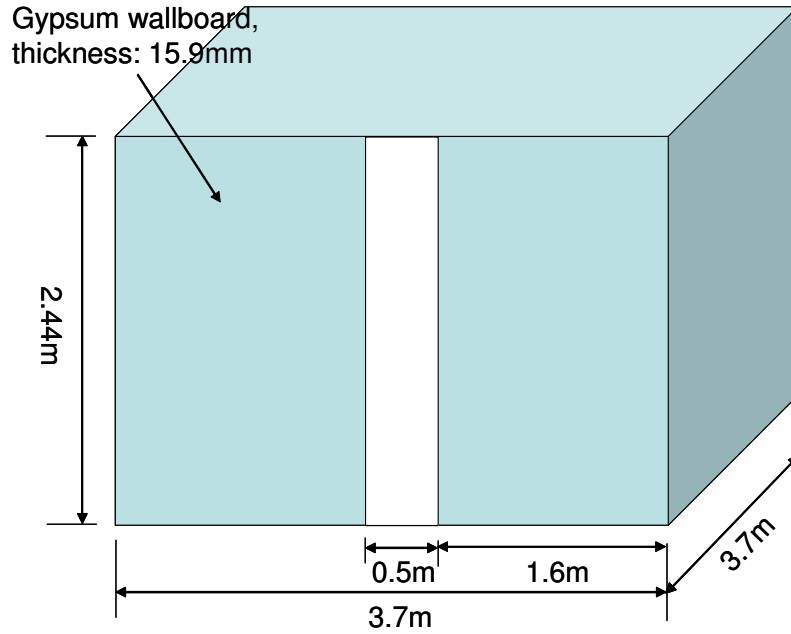


Figure 2.8 Geometry of the prototype compartment

### 2.3.2 Design of wood cribs

In order to ensure the burning time of wood cribs to be 15 *minutes* and 60 *minutes* for the two fire scenarios, the wood stick thickness of the prototype should be determined. The calculation results conducted by Perricone [87] are plotted in Figure 2.9. White oak with density of  $720 \text{ kg/m}^3$  is used as the wood due to its high density and availability. Wood stick thickness of 45 *mm* is chosen for the large fire scenario, and thickness of 19.1 *mm* is chosen for the small fire scenario. According to the scaling rules in Table 2.1, the design parameters of cribs for small-scale compartments are determined and shown in Table 2.3.

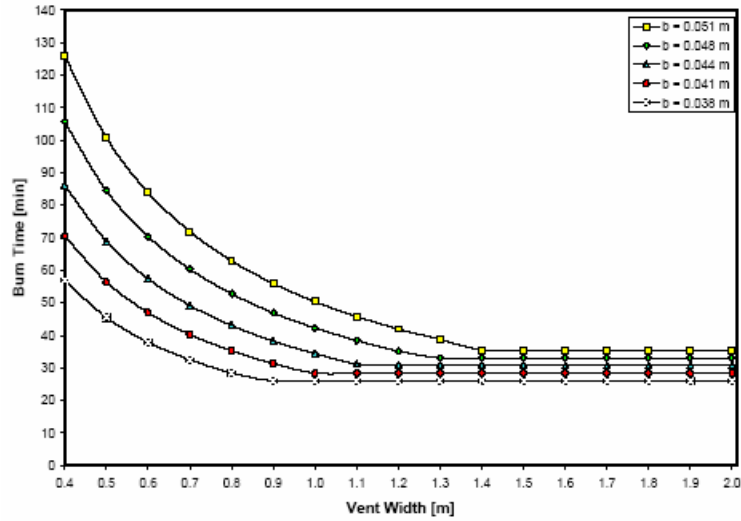


Figure 2.9 Burning time of wood cribs as function of vent width and stick thickness, from Perricone [87]

Table 2.3 Design parameters of cribs

Small fire scenario					
scale	$N_w$	$n_w$	$b_w$ (mm)	$L_w$ (mm)	$P_{or}$
1	8	28	19.1	1257	0.70
1/4	5	9	12.0	250	0.68
1/8	4	5	9.5	111	0.71
Large fire scenario					
1	8	28	44.5	2335	0.73
1/4	5	9	28.0	463	0.68
1/8	4	5	22.2	206	0.72

### 2.3.3 Design of compartment walls

Since the wall materials are usually temperature dependent, it is difficult to find a material whose thermal properties can match the scaling rules for every temperature points. A single material, therefore, cannot accurately represent the wall material throughout the experiment. The strategy in this research is to pick the expected mean temperature of compartment walls which can be predicted by using C.I.B. data [88]. For the compartment fires considered in this research, the mean temperature of walls is in the range of 400 °C to 600 °C. So the wall materials for scaled models can be determined for this specific temperature range. This material is reasonably representative to the prototype through the entire experiment.

Saffil LD mat [89] was used as the wall material to built the 1/8-scale compartment and Kaowool 3000 [90] for 1/4-scale compartment. The density of Saffil LD mat is 208 kg/m<sup>3</sup>, and the density of Kaowool 3000 is 40 kg/m<sup>3</sup>. Their specific heat are similar to that of Type C gypsum board used in the prototype, 1.0 J/kgK. Figure 2.10 shows the thermal conductivity of Kaowool 3000 and Saffil LD Mat 2.5#. These two materials are chosen by preserving  $\Pi_{w,k}$  and  $\Pi_{w,\delta}$ , and the availability. The thickness of the compartment wall of 1/8-scale model is 34 mm, and the thickness of the compartment wall of 1/4-scale is 13 mm. Figure 2.11 plots the values of  $\Pi_{w,k}$  at elevated temperatures, and Figure 2.12 plots the values of  $\Pi_{w,\delta}$  at elevated temperatures.

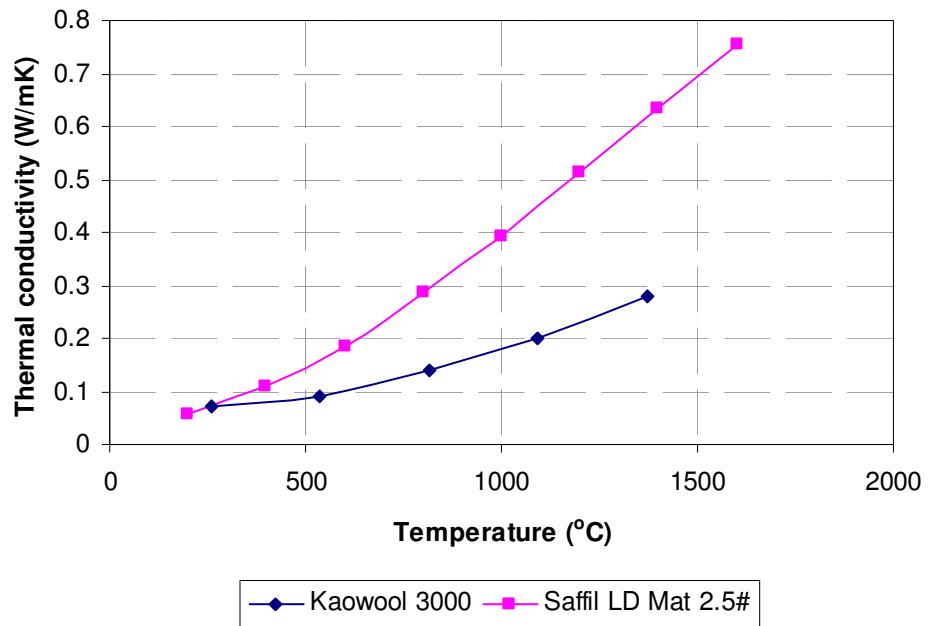


Figure 2.10 Thermal conductivity of Kaowool3000 and Saffil LD Mat

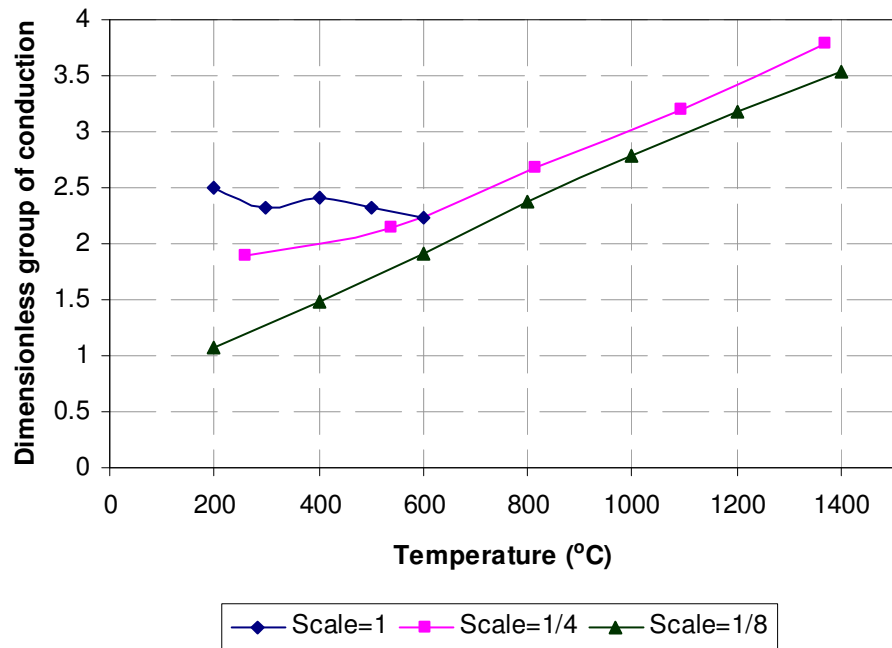


Figure 2.11 Dimensionless group of conduction verses temperature

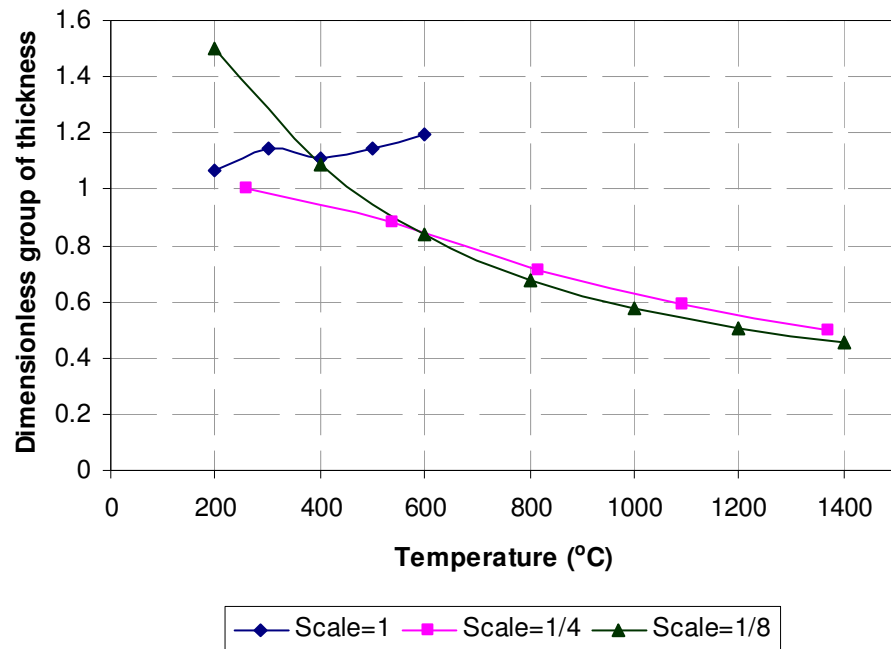
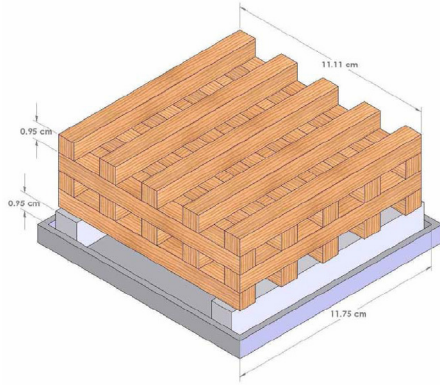


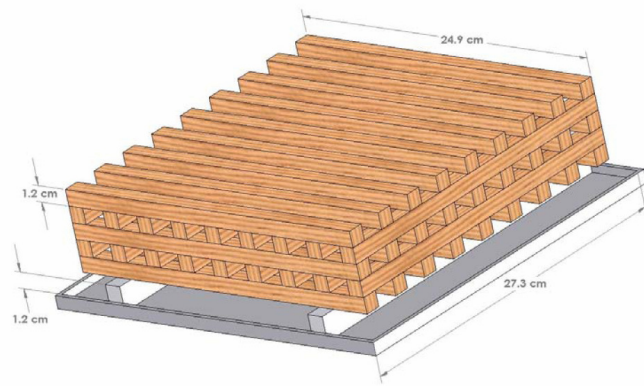
Figure 2.12 Dimensionless group of thickness verses temperature

### 2.3.4 Experimental set-up

Compartment fires at two scales (1/4 and 1/8, comparing to a 3.7m×3.7m×2.4m room prototype as shown in Figure 2.8) are conducted. For each scaled compartment, two different wood crib designs, one to represent a small fire and the other to represent a large fire are made to represent a building fire of 15-*minute* and one-hour durations, respectively. The details of the experimental set-up of scaled compartment fires can be found in Perricone [87].

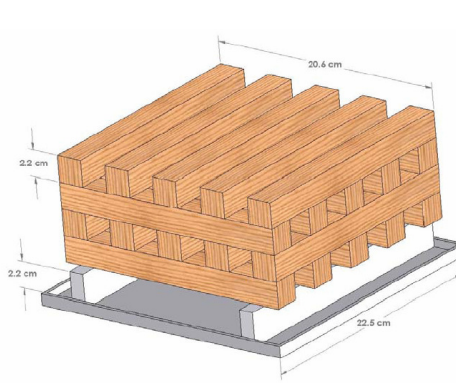


1/8-scale

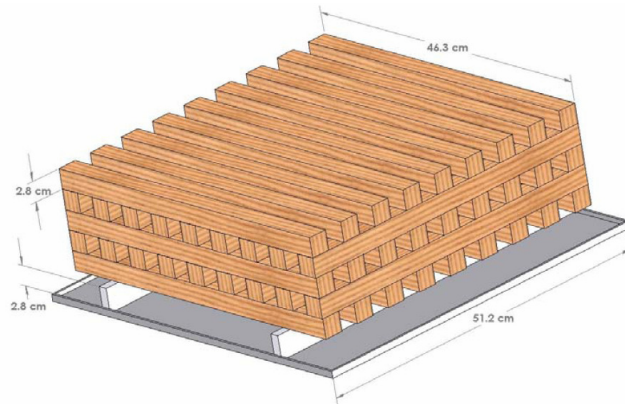


1/4-scale

Figure 2.13 Configuration of wood cribs for small fires, from Perricone [87]

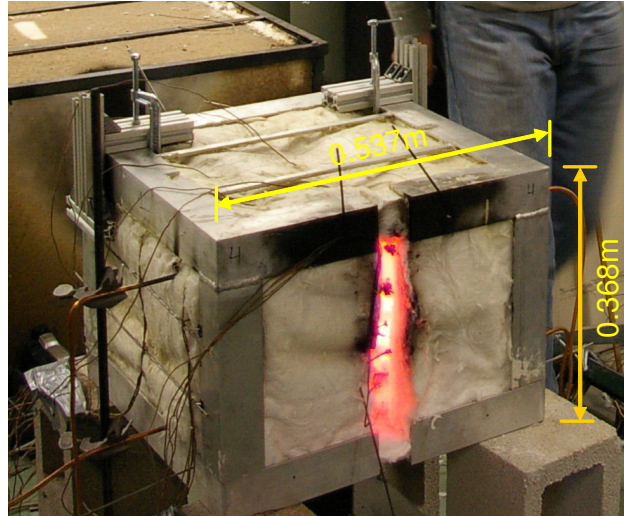


1/8-scale

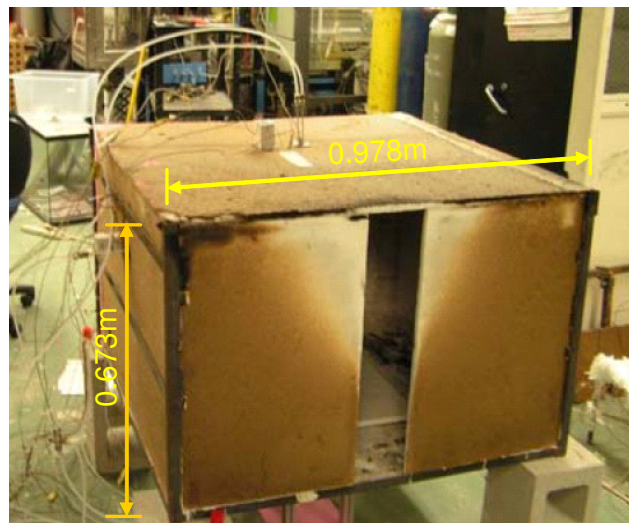


1/4-scale

Figure 2.14 Configuration of wood cribs for large fires, from Perricone [87]



**1/8-scale**



**1/4-scale**

Figure 2.15 1/8-scale and 1/4-scale Compartments

The configuration of wood cribs designed for small and large fires are illustrated in Figure 2.13 and Figure 2.14, respectively. The size of the pans used for initial ignition is also shown in these figures. The full-scale compartment dimension ( $3.7m \times 3.7m \times 2.4m$ ) is the inside space size. For the design of scaled compartments, the inside space dimension is geometrically scaled. Figure 2.15 shows the compartments used to conduct the experiments.

For each compartment-fire test, the wood mass loss rate is measured by a load cell. Hog gas temperature in the enclosure and temperature at vent at different elevation are measured by K-type thermocouples. Heat flux on the compartment walls is also measured by using heat flux sensors [91]. Figure 2.16 illustrates the schematic drawing of the typical experimental measurement set-up.

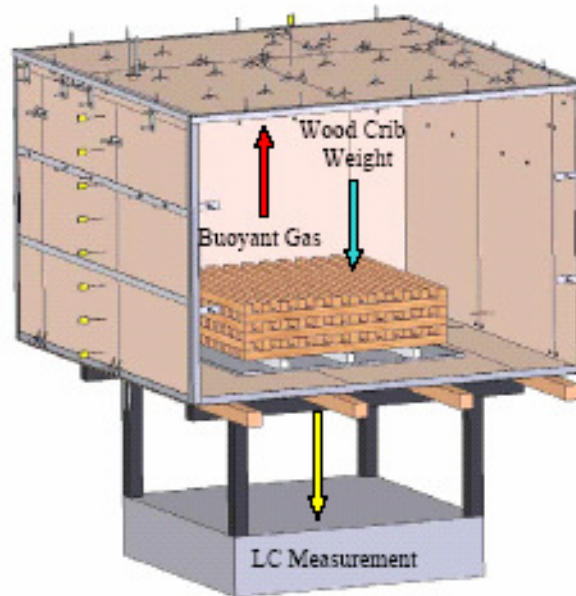


Figure 2.16 Measurement set-up (front walls not installed), from Perricone [87]

### 2.3.5 Results of scaled compartmental fires

Figure 2.17 shows the burning of two scaled fires. The burning time of wood cribs should be scaled according to  $t \sim s^{1/2}$ . The temperature in the compartment should be independent of scales,  $T \sim s^0$ . These two relations are fundamental scaling relations for the scaled fire experiments.



1/8-scale fire



1/4-scale fire

Figure 2.17 Scaled compartment fires

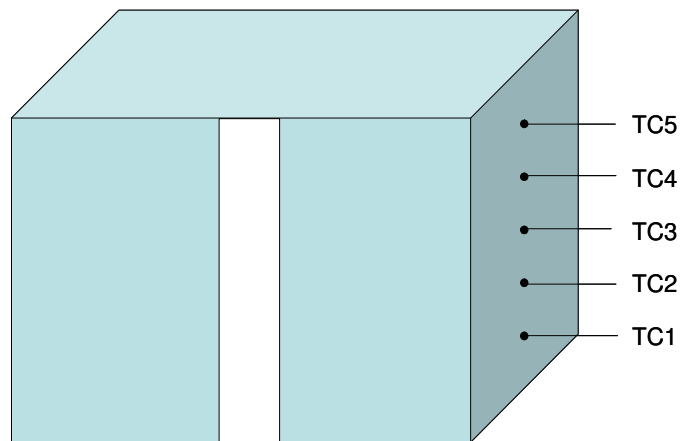


Figure 2.18 Location of 5 typical hot gas temperature measurement points

Figure 2.18 shows the location of the hot gas temperature measurement points. Those points locate insides of the compartment, and they are 2.5 *cm* away from the surface of the compartment wall. Those five thermocouples are placed at different elevation but equally spaced.

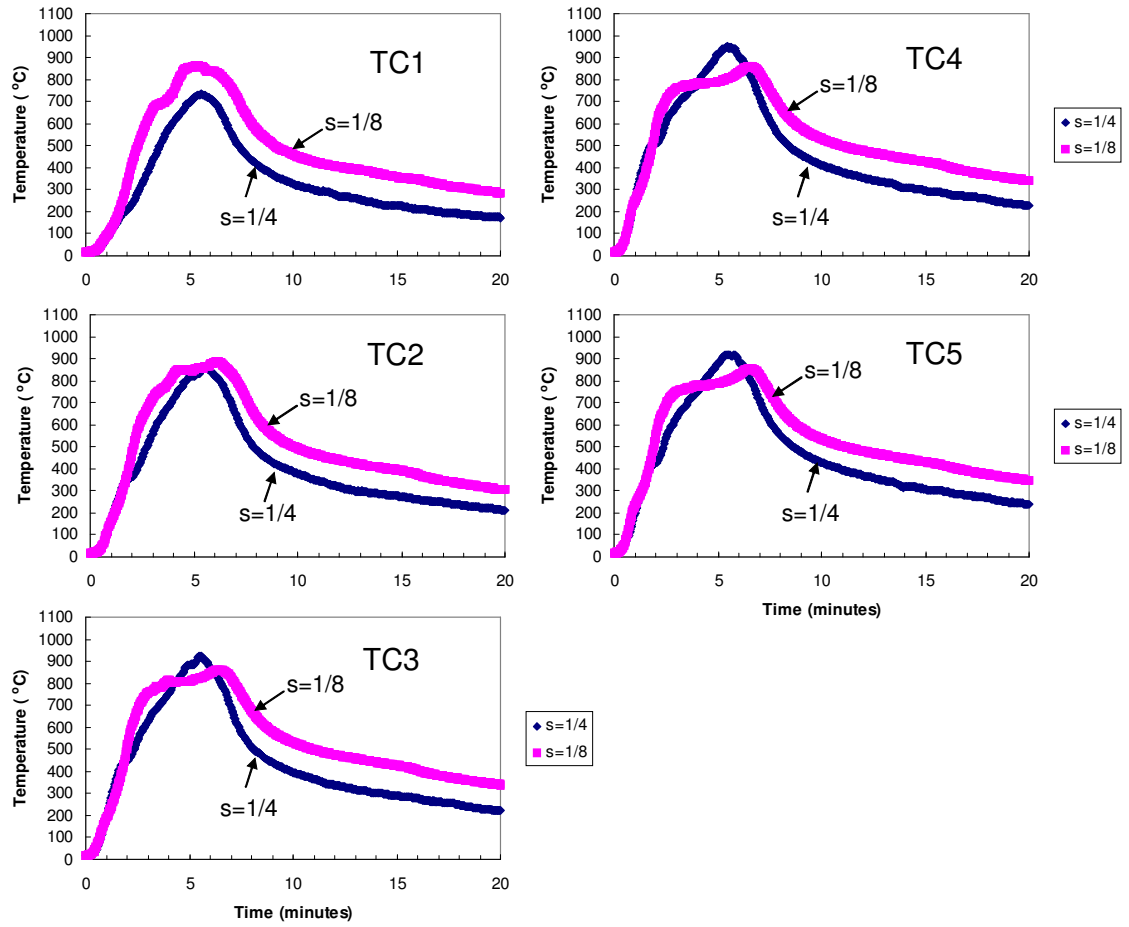


Figure 2.19 Hot gas temperature profiles of small fires

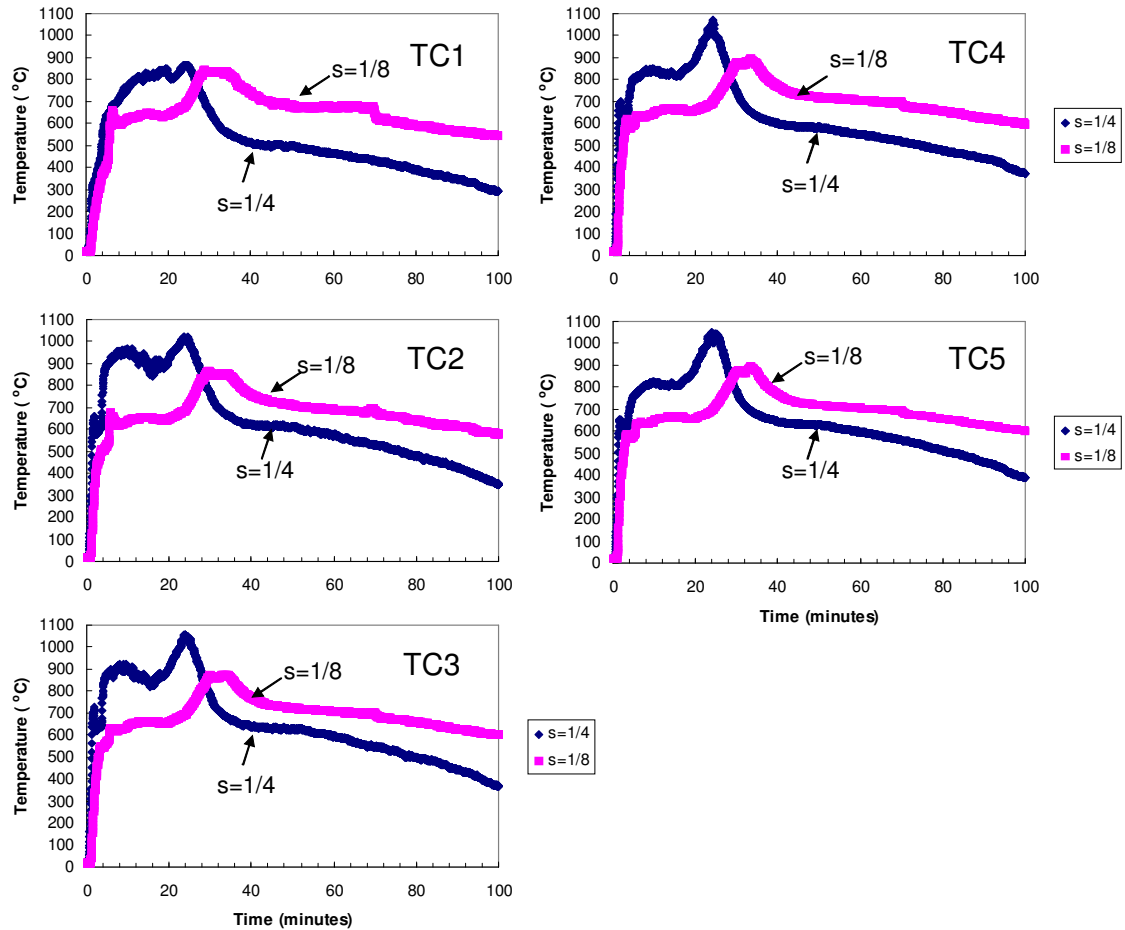


Figure 2.20 Hot gas temperature profiles of large fires

Figure 2.19 and Figure 2.20 show the hot gas temperature profiles for the small fires and large fires, respectively. They are plotted in prototype time scale ( $t_p = t_s / s^{1/2}$ ). The results show that the similarity of the compartment fires at two different scales is obtained successfully. The maximum fire temperature and the time-temperature curves compared well at different scales. However, there is a shift in the temperature profiles in the large fires as shown in Figure 2.20. The hot gas temperature in the 1/4-scale model reaches a relatively stable high temperature (800 to 900 °C) in the early burning stage (4 to 20 minutes, full-scale time); however, in

the same time range, the hot gas temperature in the 1/8-scale model remains a relatively low temperature (600 to 700 °C). This inaccuracy may be due to the assumption that the heat loss through vent by radiation is negligible. The experimental fire tests show that extremely large fire flame was observed spreading out of the vent in the large fires. The effect of the heat loss through the vent may have been important in the large fire experiments. Therefore, neglecting the heat loss through the vent may have generated errors.

More experimental data measured from the scaled compartment fires, such as heat flux onto walls, burning rate of wood cribs, and species concentration, can be found in references [87, 91]. For steel structures with fire-proof material, the hot gas temperature profiles are the most important data which are used to calculate the thermal response of the structures. The fires conducted in the two scaled compartments provide the environmental inputs for scaled structures, and the structural fire tests will be conducted by in these two compartments.

## Chapter 3: Scale modeling of structures and insulation

The scaling of compartment fires has been developed and validated in Chapter 2. This provides a platform to study structural response of structures exposed to a scaled fire. This chapter starts with the development of structural scaling which introduces basic scaling rules for design of structural geometry, structural loading and boundary conditions. Steel structures wrapped with protective insulation are considered in this research. So it is crucial to scale the insulation properly in order to obtain similar steel temperature profiles in scaled models. This chapter introduces the theoretical scale modeling of insulation and demonstrates the techniques of practical approaches to determine the insulation material used in scaled structures.

### 3.1 Theoretical development of structural scaling

If an object is exposed to a fire, the temperature change of the object can be related to the heat flux onto the object:

$$mc \frac{dT}{dt} \sim \dot{q} \quad (3.1)$$

where  $m$  is the mass of the object.  $m \sim s^3$  if the object is geometrically scaled.

$\dot{q} \sim s^{5/2}$  according to Equation 2.17.  $c \sim s^0$  since the same material is used in scaled models. So Equation 3.1 can be written as:

$$s^3 s^0 \frac{dT}{dt} \sim s^{5/2} \quad (3.2)$$

The temperature in the object should be independent of scales, so the time scale for the object is derived:

$$t \sim s^{1/2} \quad (3.3)$$

This time scale is the same as the one used in the scaled fire tests.

The structural scaling criteria can be derived from the governing equations, and one-dimensional form of stress in a structural member is used, without loss of generalization:

$$\varepsilon = \frac{\partial v}{\partial x} \quad (3.4)$$

$v$  is a deformation vector in  $x$  direction. Structural members are geometrically scaled ( $x \sim s$ ). If deformation is scaled as  $v \sim s$ , the strain is then scaled according to  $\varepsilon \sim s^0$ . That means the strain in both prototype and models keeps constant.

Stress can be related to strain or force:

$$\sigma = \varepsilon E, \quad \sigma = \frac{\partial F}{\partial x \partial y} \quad (3.5)$$

Since the same material is used in both prototype and models ( $E \sim s^0$ ), stress and force are scaled according to:

$$\sigma \sim s^0 \text{ and } F \sim s^2 \quad (3.6)$$

If a beam-column model is considered as shown in Figure 3.1, the equilibrium of bending resistance and external moment can be written as:



Figure 3.1 Beam-column model

$$-EI \frac{d^2 y}{dx^2} = Py + M_1 + (M_2 - M_1) \frac{x}{L} \quad (3.7)$$

$y$  is the transverse deflection.  $E$  is the elastic modulus.  $P$  is the axial force which can be induced by the elevated temperature of the beam.  $M$  is the applied moment at the ends.  $L$  is the length of the beam. In the scaled model, the deflection shape should be similar to that of the prototype. That means  $\frac{dy}{dx} \sim s^0$ . If the model is geometrically scale ( $x \sim s$ ), the scaling for the transverse deflection is

$$y \sim s \quad (3.8)$$

For a geometrically scaled model,  $A \sim s^2$ ,  $V \sim s^3$  and  $I \sim s^4$ . If the material in the model is the same as that in the prototype (*i.e.*,  $E \sim s^0$ ;  $\rho \sim s^0$ ), the scaling laws for mass is  $m \sim s^3$ . By putting these relations into Equation 3.7,

$$-s^0 s^4 \frac{s}{s^2} \sim Ps \sim M_1 \sim (M_2 - M_1) \frac{s}{s} \quad (3.9)$$

So the scaling laws for force and moment are

$$P \sim s^2 \text{ and } M \sim s^3 \quad (3.10)$$

The axial force,  $P$ , in the beam-column is determined by the combined effect of beam shortening due to vertical deflection and resistance to thermal expansion due to elevated temperature [62].

$$P = K\Delta L = K \left( \int_0^L \left[ 1 + \left( \frac{dy}{dx} \right)^2 \right]^{1/2} dx - L - \alpha(T - T_\infty)L \right) \quad (3.11)$$

$K$  is the end axial stiffness, and it is determined by the stiffness of the remaining structural system connected to the beam. The scale relation for  $\Delta L$  is  $\Delta L \sim s^l$ . So the end axial stiffness should be scaled according to:

$$K \sim s \quad (3.12)$$

Therefore, the boundary constraint on a scaled model needs to be designed according to Equation 3.12 in order to keep the deformation and axial forces to be scaled properly.

### 3.2 Testing of scaled frames in oven

The theory of structural scaling shows that the strain/stress should be independent of scales if the external structural loading is scaled according to Equation 3.10. The scaling theory holds true in elevated temperature if the same material is used in both the prototype and models ( $E \sim s^0$ ). Testing of aluminum frames at two scales (2/3 and 1) is conducted in an oven to validate this point.

Figure 3.2 shows the experimental set-up of the testing in an oven. The two aluminum frames are geometrically scaled. The height of the columns in the prototype is 45.7 cm, and the length of the beams is 22.9 cm. The height of the columns in the 2/3-scale model is 30.5 cm, and the length of the beams is 15.2 cm. 19.0mm×19.0mm×1.6mm aluminum angles are used as the columns and beams in the prototype, and 12.7mm×12.7mm×1.1mm aluminum angles are used in the 2/3-scale model. The frames are loaded by adding weight on the beams. The total weight on the prototype frame is 50.8 kg, and the weight on the 2/3-scale frame is 22.7 kg. Figure 3.3 and Figure 3.4 show the strain measurement of at the mid-span and the location close to the end of the beam, respectively. The testing results show that the strain measurements in the beams at two different scales compare well. This experiment

demonstrates that the structural response at elevated temperature can be simulated by using a small-scale model if correct scaling rules are used.



Figure 3.2 Testing of scaled frames in oven

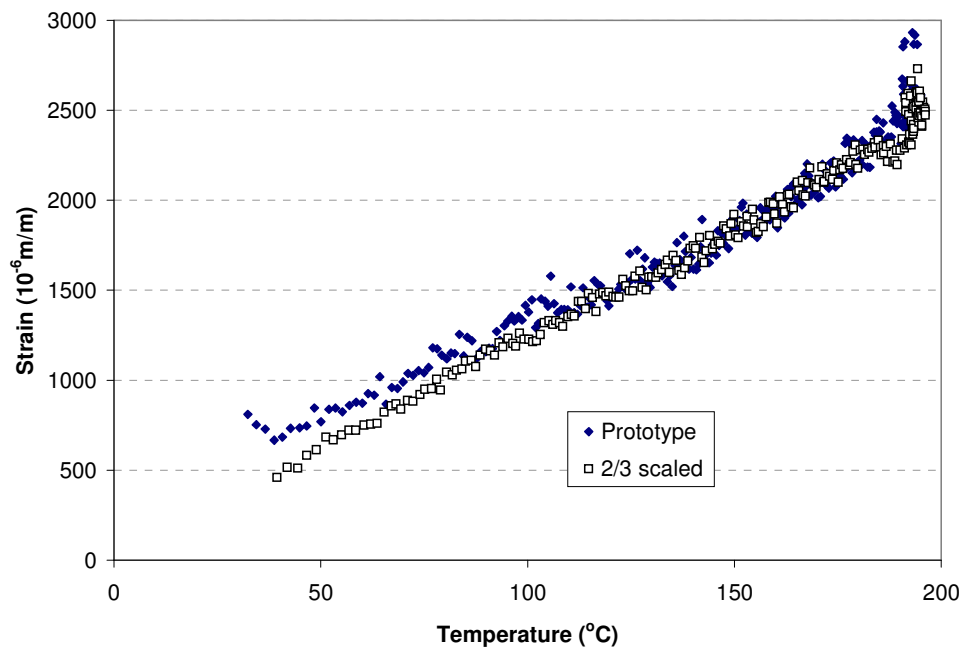


Figure 3.3 Strain at the mid-span of the beam

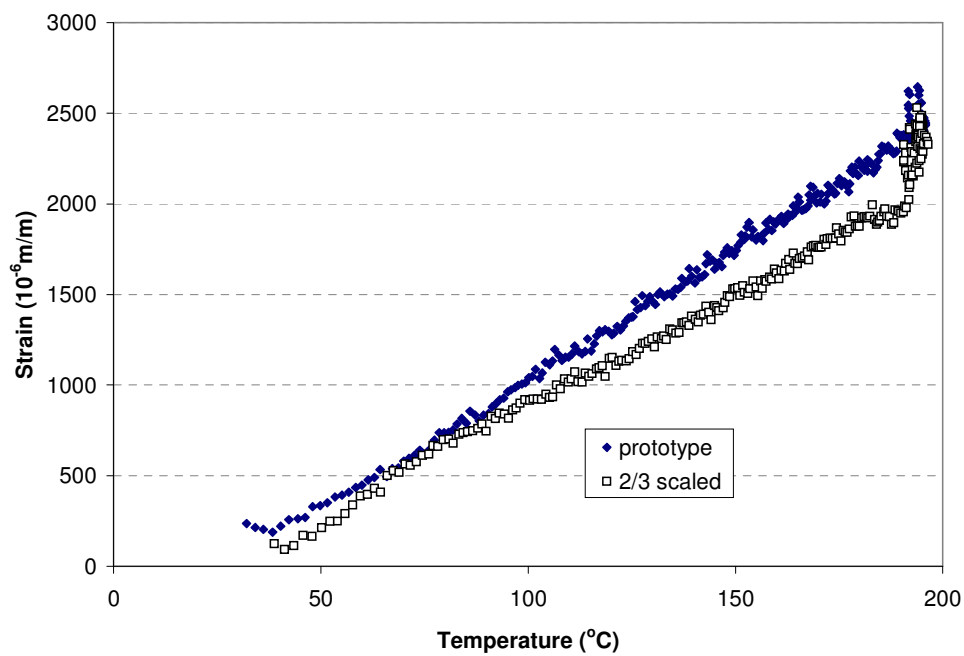


Figure 3.4 Strain at the location close to the end of the beam

### 3.3 Theoretical development of insulation scaling

A scaled insulated structure in a scaled fire compartment is considered. Conduction dominates the heat transfer through solids in most compartment fire scenarios, under these conditions the governing equation can be written as:

$$m_s c_s \frac{dT_s}{dt} + m_i c_i \frac{dT_i}{dt} \sim \frac{k_i}{\delta_i} A_s (T_f - T_s) \quad (3.13)$$

Heat is stored in both the structural material (*e.g.*: steel) and the insulation. The temperature in steel can be considered to be uniform since the thermal conductivity of steel is much higher than that in the insulation. Another simplifying assumption is that the hot gas temperature is equal to the insulation surface temperature as the radiation and convection have small thermal resistances at the solid boundaries.

To determine the amount of insulation in a scaled model, Equation 3.13 must be preserved at different scales. Different scaling approaches can be derived by assuming that the heat capacity of the insulation is negligible or not.

#### **Consider the heat capacity of insulation**

If the heat capacity of insulation is not negligible, the relation of insulation properties for scaled model can be obtained by writing Equation 3.13 using dimensionless ratios. To make the equation dimensionless, temperature and time are

written in terms of the ratios  $\frac{T}{T_\infty} = \hat{T}$ , and  $\frac{t}{t_r} = \hat{t}$ . And rearranging terms, Equation

3.13 becomes:

$$\begin{aligned} \frac{k_i}{\delta_i} &\sim \left(\frac{m_s c_s}{t_r A_s}\right) \frac{d\hat{T}_s}{d\hat{t}} \left(\frac{l}{\hat{T}_f - \hat{T}_s}\right) \frac{T_\infty}{T_\infty} + \left(\frac{m_i c_i}{t_r A_s}\right) \frac{d\hat{T}_i}{d\hat{t}} \left(\frac{l}{\hat{T}_f - \hat{T}_s}\right) \frac{T_\infty}{T_\infty} \\ &\sim \frac{m_s c_s}{t_r A_s} + \frac{m_i c_i}{t_r A_s} \end{aligned} \quad (3.14)$$

The mass of insulation,  $m_i$ , can be approximately written as:

$$m_i \approx DL\delta_i\rho_i \quad (3.15)$$

Substitute Equation 3.15 into Equation 3.14,

$$\frac{k_i}{\delta_i} \sim \frac{m_s c_s}{s^{5/2}} + \frac{DL\delta_i\rho_i c_i}{s^{5/2}} \quad (3.16)$$

where  $D$  is sectional perimeter of the insulated steel member,  $L$  is the length of the steel member. There are two terms in Equation 3.16: the term corresponding to steel

$\left(\frac{m_s c_s}{s^{5/2}}\right)$ , and the term corresponding to insulation  $\left(\frac{DL\delta_i\rho_i c_i}{s^{5/2}}\right)$ . Preserving the

insulation term in Equation 3.16 implies that

$$\frac{k_i}{\delta_i} \sim \frac{DL\delta_i\rho_i c_i}{s^{5/2}} \quad (3.17)$$

Solving for  $\delta_i$ , then

$$\delta_i^2 \sim s^{1/2} \frac{k_i}{\rho_i} \sim s^{1/2} \quad (3.18)$$

Since the thermal conductivity is approximately proportional to its density for most insulation materials ( $k_i \sim \rho_i$ ), and  $L \sim D \sim s^1$ ,  $c_i \sim s^0$ . So the insulation thickness in the scaled model can be determined:

$$\delta_i \sim s^{1/4} \quad (3.19)$$

For a geometrically scaled structure,  $m_s \sim s^3$ . From the steel term in Equation 3.16, the scaling rule for insulation material properties can be determined by substituting Equation 3.19 into Equation 3.16:

$$k_i \sim \rho_i \sim s^{3/4} \quad (3.20)$$

Equation 3.20 implies that the insulation does not scale geometrically. Instead, adjustment must be made to the thickness and/or the thermal properties of the insulation material so that the scaling law in Equation 3.21 can be satisfied.

Equation 3.20 suggests that the density of the insulation can be changed. While this is a possible solution, changing the property of the insulation can be impracticable. For example, Equation 3.20 shows that the density is proportional to the scale factor. Therefore, lighter insulating materials are needed for small-scale models. Since insulating materials used for full-scale structures are usually light-weight materials, the lighter insulating material for scaled models may not exist. One alternative is to use the same insulation for scaled model as it is used in the prototype, which implies  $k_i \sim \rho_i \sim s^0$ . Then Equation 3.16 becomes

$$\frac{l}{\delta_i} \sim \frac{m_s}{s^{5/2}}, \quad \frac{l}{\delta_i} \sim \frac{\delta_i}{s^{1/2}} \quad (3.21)$$

Using the insulation term, the scaling rule for insulation thickness must follow  $\delta_i \sim s^{1/4}$ . Using the steel term and the insulation scaled according to  $\delta_i \sim s^{1/4}$  the mass of steel must be scaled to

$$m_s \sim s^{9/4} \quad (3.22)$$

A geometrically scaled steel structure, however, has  $m_s \sim s^3$ . Compensation for this difference in mass can be made by adding a heat sink to the structure such that the mass of the heat sink is:

$$\Delta m = (s^{9/4} - s^3)m_p \quad (3.23)$$

This can be achieved by attaching additional steel,  $\Delta m$ , to the steel structural elements under the insulation.

### **Neglect the heat capacity of insulation**

Insulation material usually is very light weight, so  $m_i c_i$  are often much smaller than  $m_s c_s$ , the mass and specific heat of steel. Hence, the heat capacity of the insulation can be neglected for structures with light-weight and thin insulation. Then Equation 3.13 can be written as:

$$m_s c_s \frac{dT_s}{dt} \sim \frac{k_i}{\delta_i} A_s (T_f - T_s) \quad (3.24)$$

Writing temperature and time in terms of the ratios  $\frac{T}{T_\infty} = \hat{T}$ , and  $\frac{t}{t_r} = \hat{t}$ , and

rearranging terms, Equation 3.24 becomes:

$$\frac{k_i}{\delta_i} \sim \left( \frac{m_s c_s}{t_r A_s} \right) \frac{d\hat{T}_s}{d\hat{t}} \left( \frac{1}{\hat{T}_f - \hat{T}_s} \right) \frac{T_\infty}{T_\infty} \quad (3.25)$$

In Equation 3.25,  $A_s \sim s^2$  is applied as geometry is preserved. Similarly,  $m_s \sim s^3$ .  $c_s$  does not vary significantly for typical insulation materials. Therefore the insulation on the scaled model must have the relation:

$$\frac{k_i}{\delta_i} \sim \frac{m_s c_s}{t_r A_s} \sim \frac{s^3 s^0}{s^{1/2} s^2} \sim s^{1/2} \quad (3.26)$$

If the same insulation material is used in the scaled model ( $k_i \sim s^0$ ), the thickness of insulation must be scaled according to:

$$\delta_i \sim s^{-1/2} \quad (3.27)$$

### 3.4 Numerical simulation of thermal response of insulated steel

Three approaches have proposed to choose insulating material on scaled structural models. According to Equation 3.27, only the thickness of insulation needs to be scaled. In this approach, the same insulation is used in scaled models as that of the prototype. The second approach uses a different insulating material with properties according to Equation 3.20, and the thickness of the insulation is scaled according to Equation 3.19. A third approach uses the same insulation, but adds heat sinks according to Equation 3.23 in addition to the thickness adjustment. Table 3.1 lists the scaling rules for determining insulating materials on scaled structural members.

Table 3.1 Summary of scaling rules for insulation

	Thermal conductivity $k_i$	Density $\rho_i$	Thickness $\delta_i$	Additional mass $\Delta m$
Approach 1 (with thickness change only)	$s^0$	$s^0$	$s^{-1/2}$	---
Approach 2 (with material change)	$s^{3/4}$	$s^{3/4}$	$s^{1/4}$	---
Approach 3 (with heat sink)	$s^0$	$s^0$	$s^{1/4}$	$s^{9/4} - s^3$

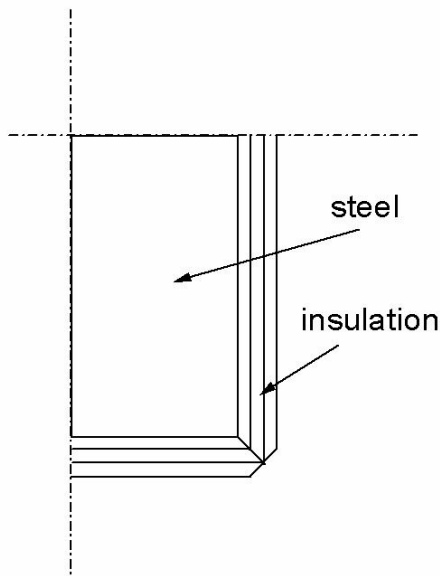


Figure 3.5 2-D finite element model of insulated steel

Numerical simulations are conducted to compare the accuracy of the three approaches listed in Table 3.1. An insulated steel rectangle solid bar with a prototype cross sectional dimension of  $100\text{mm} \times 25\text{mm}$  heated externally according to ASTM E119 standard time-temperature curve [13] is simulated in the heat transfer code

FIRES-T3 [77]. Figure 3.5 shows the rectangle 2-D finite element model used. A quarter-scale model is also simulated in FIRES-T3. The ASTM E119 curve is used to represent the hot gas temperature on the insulated structural members. For the quarter-scale model, the time of the temperature curve is scaled according to  $t \sim s^{1/2}$ . Figure 3.6 shows the temperature curves for the prototype and the quarter-scale model. The ASTM E119 curve used in the numerical simulation is not intended to represent temperature profiles of real-world fires. It is adopted here to quickly compare the three approaches listed in Table 3.1. The same fire boundary conditions such as the effect of convection and radiation between the insulation surface and the hot gas are used in the simulation. The same convection coefficient and emissivity of gas are applied to both the prototype and the scaled models. The resulting temperature profiles adjusted to the prototype time scale are shown compared to the prototype temperature in Figure 3.7.

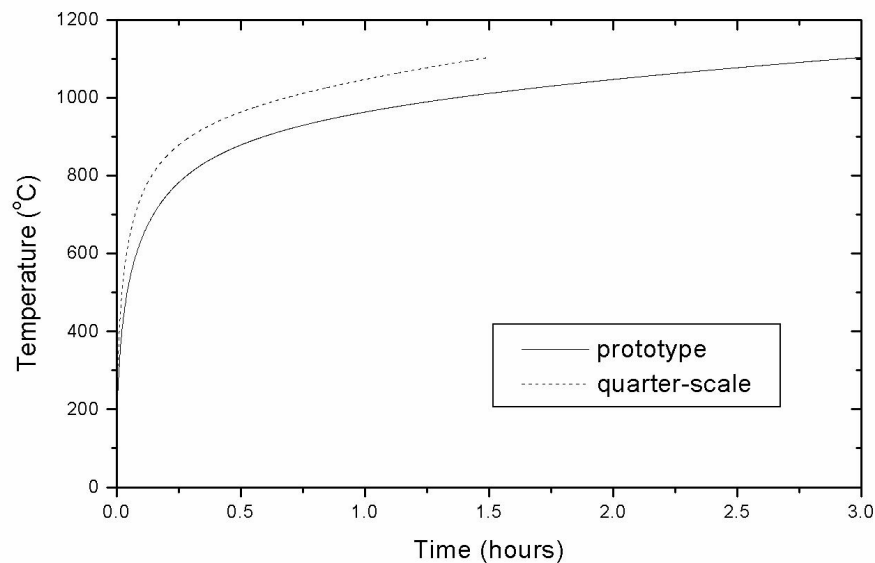


Figure 3.6 Temperature curves of full-scale and quarter-scale models

In order to show that geometric scaling leads to erroneous thermal effect prediction, a scaled model with geometrically scaled insulation is simulated. The results shown compared to the previous approaches.

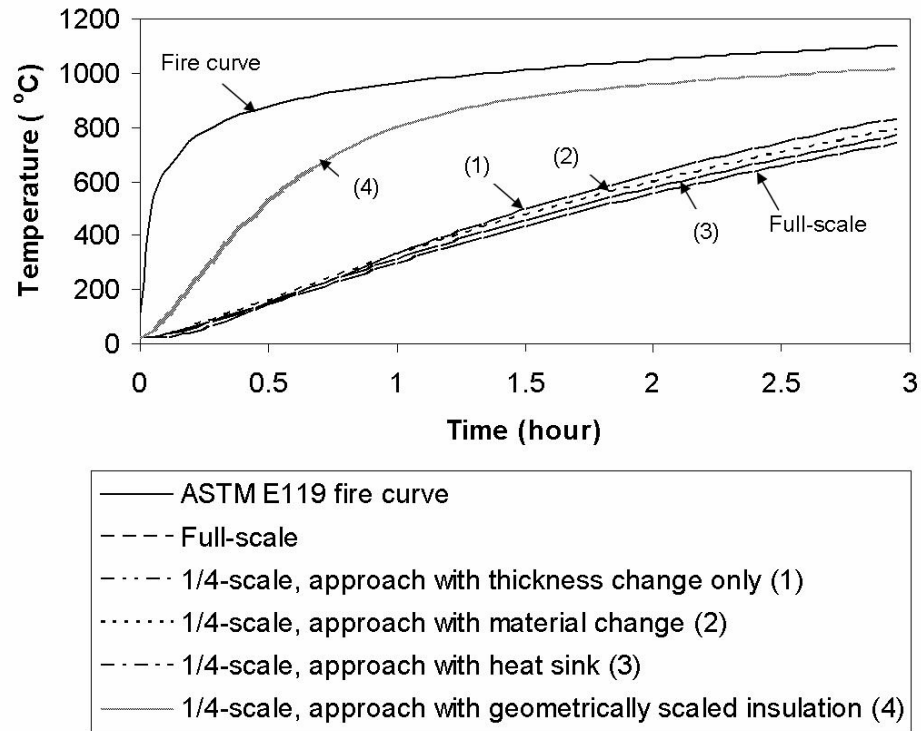


Figure 3.7 Temperature of steel in full-scale and quarter scale models

$$\begin{aligned}
 &((1): k_i \sim \rho_i \sim s^0, \delta_i \sim s^{-1/2}; (2): k_i \sim \rho_i \sim s^{3/4}, \delta_i \sim s^{1/4}; \\
 &(3): k_i \sim \rho_i \sim s^0, \delta_i \sim s^{1/4}, \Delta m = (s^{9/4} - s^3)m_p; (4): k_i \sim \rho_i \sim s^0, \delta_i \sim s)
 \end{aligned}$$

Figure 3.7 shows the time-history of the steel temperature for both the full-scale and the quarter-scale models. The results are plotted in prototype time scale for easy comparison. The results show that scaled model with the same insulation materials but different thicknesses result in a temperature profile that is similar to that of the prototype. Scaling of the insulation material properties and adding heat sinks

are both effective in emulating the prototype material behavior. Figure 3.7 also shows that the scaled model with geometrically scaled insulation results in a structural temperature that is significantly different from that of the prototype.

Table 3.2 shows the comparison of numerical results in the form of errors at 1-hour, 2-hour and 3-hour. The approach with geometrically scaled insulation compares poorly to the prototype. Listing this result here does not imply that geometrical scaling of insulation is an approach used by experimentalists. It is listed only to show that geometrically scaling the insulation thickness can lead to grossly erroneous results. Geometric scaling of the insulation should be avoided. The other three approaches listed above are derived from the basic heat transfer equation where the heat transfer mechanism is dominated by conduction. The results in Table 3.2 show that following the laws of similitude by changing the material properties of the insulation results in reasonably good temperature predictions. Using heat sink to produce the appropriate thermal mass is another effective approach of scale modeling. In practical situations, however, neither the change in insulation nor the addition of heat sink is always possible. By using the simplifying assumption that the thermal mass of the insulation material being small compared to the thermal mass of the structure, it is possible to use the same insulation material on the scaled model. Only the thickness of the insulation is changed. Numerical simulation results are shown in Table 3.2, where errors compared to the prototype temperature show the relative accuracy of the different approaches of scale modeling. The relative ease of the approaches is also indicated. Changing the thickness of the insulation is by far the

easiest approach. While the error is greater than the other approaches, it is within 14% of the prototype.

Table 3.2 Comparison of numerical results and application comments

	Approach 1 with thickness change only	Approach 2 with material change	Approach 3 with heat sink	Approach with geometric. scaled insulation
Error (1hr)	11.6%	11.1%	5.4%	172%
Error (2hr)	13.4%	8.2%	4.2%	74.3%
Error (3hr)	12.2%	7.0%	3.5%	37.8%
Appl.	Easy	Difficult <sup>1</sup>	Moderate <sup>2</sup>	Avoid

<sup>1</sup> *Practically, it is difficult to find the different insulation material to satisfy the scaling.*

<sup>2</sup> *When scale is small, the mass of heat sink can be much bigger than the geometrically scaled mode, and it is not practical to add heat sink to the scaled model without changing the surface area.*

The temperature profiles used in the numerical simulation are not necessarily representative to real-world fires. Moreover, the temperature profile for the small-scale model is generated based on the ASTM E119 curve while compressing the time according to  $t \sim s^{1/2}$ . Therefore, the results obtained from the numerical simulation are based on the ideal case in which the temperature profile of the small-scale model is identical to that of the prototype under the same time scale. This numerical simulation provides a comparison of the different approaches developed in this dissertation. Experimental investigation using scaled compartment fires is presented next.

### 3.5 Experimental validation of insulation scaling

#### 3.5.1 Test of insulated steel rods

The numerical simulations in the previous section provide a quick check for the different approaches of scaling developed in this dissertation. The approach with a change in thickness is the easiest approach to implement since the same insulation material can be used in both the prototype and the scaled model. Even the simplest approach generated simulation results within 14% of the prototype temperature. Experiments are performed to validate these findings. The experiment is conducted in two compartment fires with scale factors of 1/8 and 1/4 (comparing to a 3.7m×3.7m×2.4m room as prototype). The design of the fuel (wood cribs) and compartment material follows the theory presented in the Chapter 2. Two small-scale fires are designed to emulate a building fire. With two different wood crib designs, both small fire and large fire are made to represent a building fire with approximate 15-minute and one-hour durations, respectively. Figure 3.8 shows the experimental set-up of the compartment and insulated steel column. Saffil LD mat [89] with thermal conductivity  $k_0 = 0.11 \text{ W / mK @ } 400^\circ \text{ C}$  and density  $\rho_0 = 40 \text{ kg / m}^3$  is used as insulation in both models. The thickness of insulation follows  $\delta_i \sim s^{-1/2}$ . So the thickness in 1/8-scale model is 36 mm (1.4 inch) and 25 mm (1.0 inch) for 1/4-scale model which represent the thickness of 13 mm (0.5 inch) in the prototype. The 1/8-scale steel column is a 305-mm (12-inch) rod with 6.4-mm (0.25-inch) diameter, and the 1/4-scale steel column is a 610-mm (24-inch) rod with 12.8-mm (0.5-inch) diameter. Three K-type thermal couples are attached to the steel vertically with equal

spacing. A series of K-type thermal couples are placed in the zones away from direct flame contact in order to measure the hot gas temperature in the compartment.

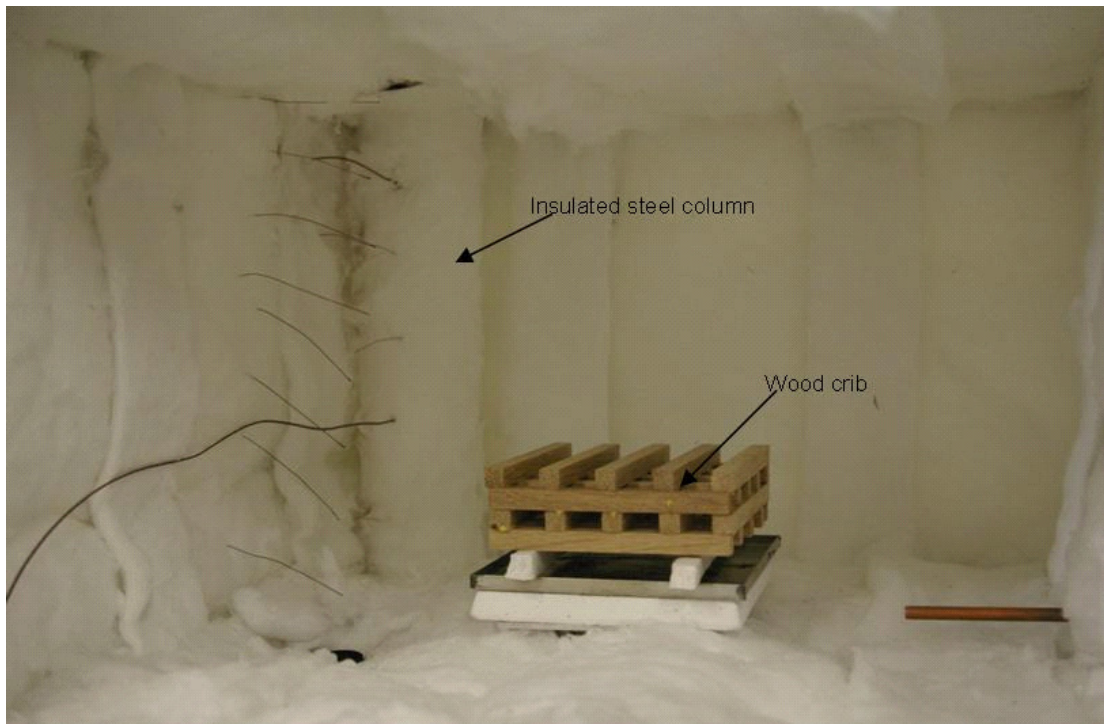


Figure 3.8 Experimental set-up of compartment fire and insulated steel column

Figure 3.9 and Figure 3.10 show the temperature profile of hot gas in the compartment for both small and large fires. The time shown in the figures is scaled to full-scale time for easy comparison. The temperature measurement of steel is also shown in Figure 3.9 and Figure 3.10. Results show the steel temperature profiles measured in 1/8-scale fire and 1/4-scale fire are similar. The numerical simulation is conducted in FIRES-T3 by using the fire temperature profiles measured in the compartment fires. The results from the experiments are not intended to verify the results from the numerical simulation here because the boundary conditions used in the simulation might not be identical to that of the compartment fires. The numerical simulation here is to show the difference of steel temperatures due to difference of the

fire temperatures. In the numerical simulation, identical boundary conditions such as effect of convection and radiation are applied to both the prototype and the scaled models. The nonlinear heat transfer from fire is used in FIRES-T3 and it is modeled as [77]:

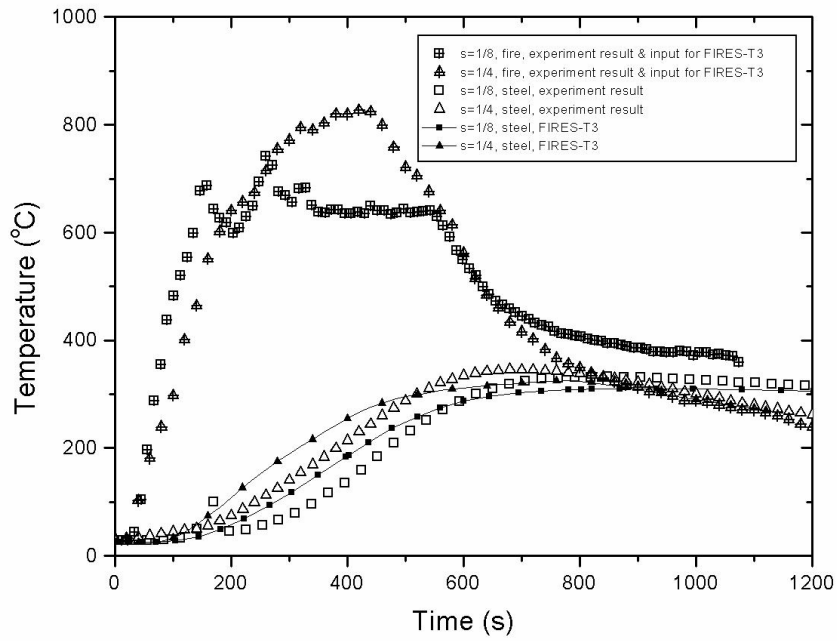
$$\dot{q}'' = h_c(T_f - T_{surf})^N + F_{12}\sigma(\alpha_s\varepsilon_f T_f^4 - \varepsilon_s T_{surf}^4) \quad (3.28)$$

In the numerical simulation, the identical fire boundary conditions are applied to the models at different scales:  $h_c = 0.27$ ,  $N = 1.25$ ,  $F_{12} = 1.0$ ,  $\sigma_g = 1.7 \times 10^{-9}$ ,  $\alpha_s = 0.9$ ,  $\varepsilon_f = 0.9$  and  $\varepsilon_s = 0.9$ . According to the theory of fire scaling introduced in Chapter 2, the effect of convection and radiation should be scaled, such that  $h_c \sim s^{1/2}$  and  $\varepsilon_f \sim s^{1/2}$ . However, this might be difficult or impracticable in applications. In the numerical simulation, they are kept constant. This procedure is expected to generate some error, but they are relatively insignificant since the effect of conduction dominates for the heat transfer through solids.

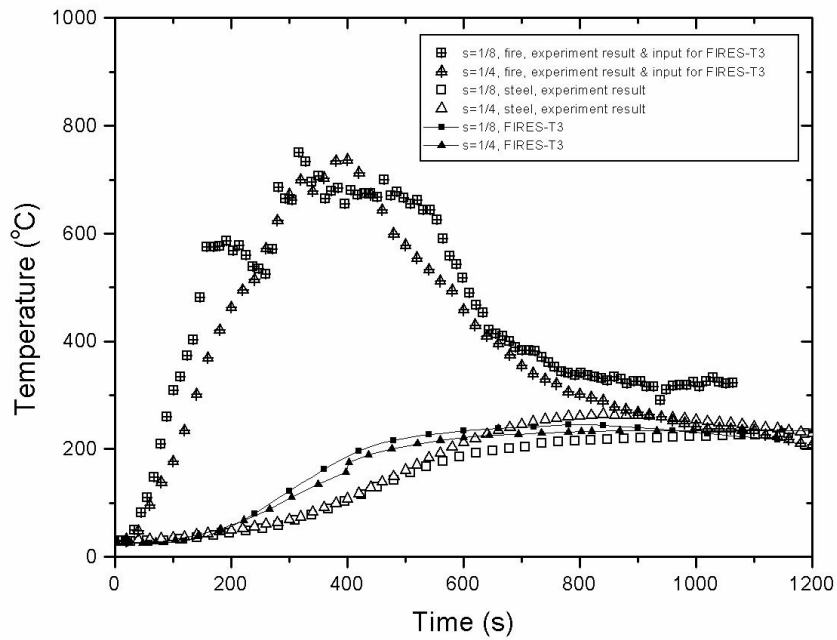
The temperature profiles measured in the experiments represent the high temperature environment in actual fires. As shown in Figure 3.9 and Figure 3.10, the temperature curves of the scaled models are not identical. This is different from the ASTM E119 curves used in previous numerical simulation in which the temperature curves are identical if they are plotted in the same time scale.

The difference of compartment fire temperature profiles is reflected in the steel temperature. However, another significant factor that generates some error is the increase of the surface area in scaled models. When the thickness follows  $\delta_i \sim s^{-1/2}$ , the smaller model has a thicker insulation. If the insulation thickness is relatively big

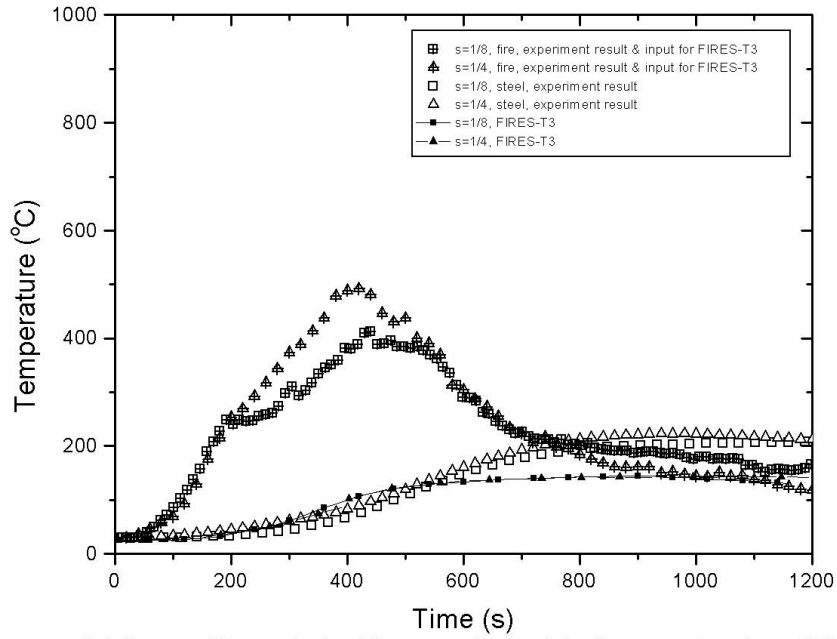
compared to the size of the steel member, the assumption,  $A_s \sim s^2$ , used in Equation 3.15 is less accurate. Since the assumption  $A_s \sim s^2$  is used in this paper, the error due to the change of the surface area of insulated steel member needs to be noted. Table 3.3 shows the relative difference of temperature between 1/4-scale and 1/8-scale models, which is calculated by  $\left| \frac{T_{1/4} - T_{1/8}}{T_{1/4}} \right|$ . Since the difference of the fire temperature at the beginning of the burning can be due to the ignition differences, only the fire temperature measurement in the peak temperature range is used to calculate the average relative difference: t=200 to 600 seconds for the small fire and t=800 to 1800 seconds for the large fire. The relative difference of the steel temperature is calculated for t=600 to 1000 seconds for the small fire and t=1800 to 2800 seconds. The results show that the relative difference of the steel temperature is within the difference of the fire temperature.



(a) Fire profile and steel temperature at the top region (small fire)

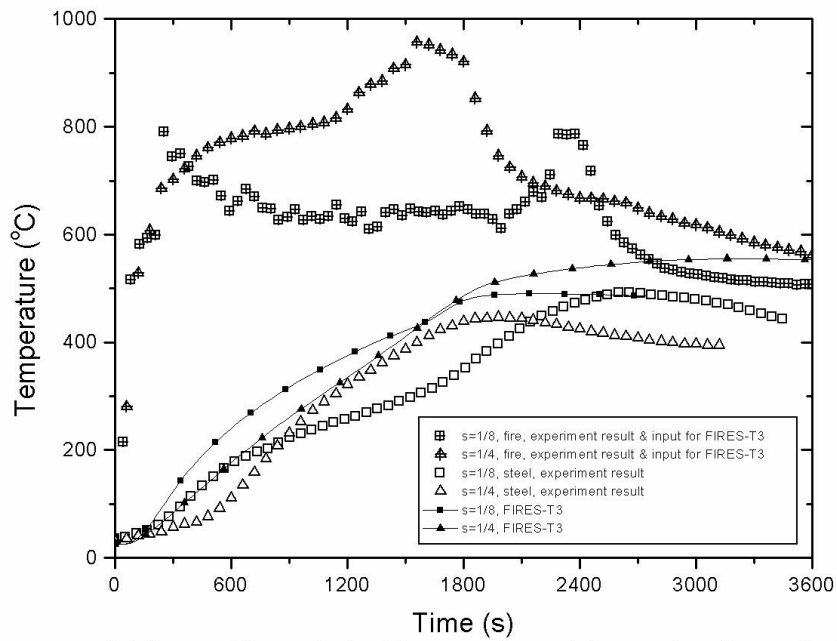


(b) fire profile and steel temperature at middle region (small fire)

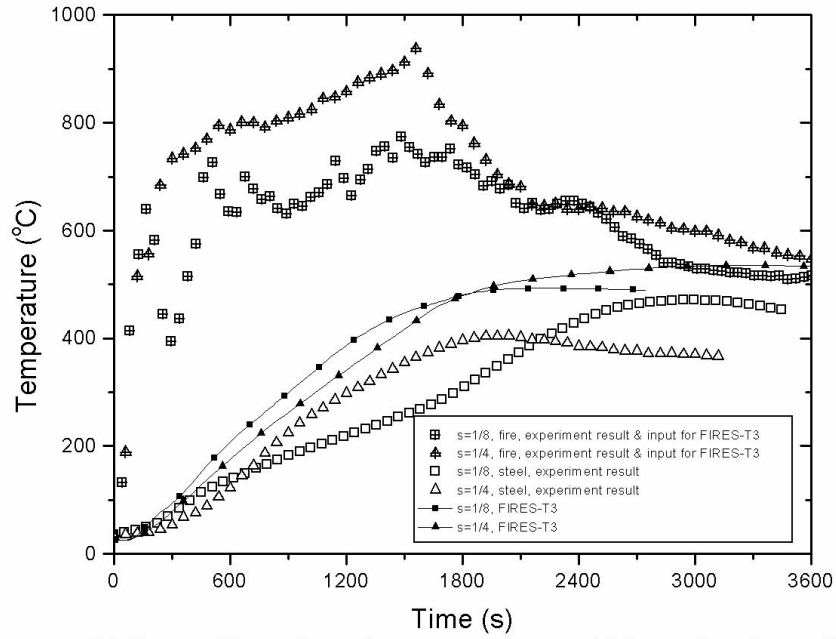


(c) fire profile and steel temperature at bottom region (small fire)

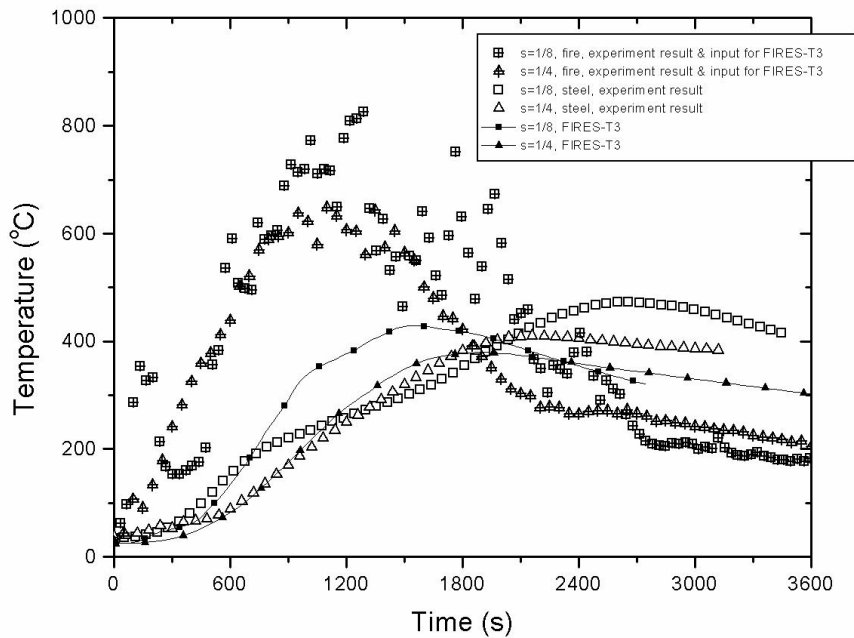
Figure 3.9 Fire temperature profile and steel temperature in the small fire



(a) fire profile and steel temperature at top region (large fire)



(b) fire profile and steel temperature at middle region (large fire)



(c) fire profile and steel temperature at bottom region (large fire)

Figure 3.10 Fire temperature profile and steel temperature in the large fire

Table 3.3 Relative differences of fire and steel temperature between 1/4-scale and 1/8-scale models

Average relative temperature difference		Small fire	Large fire
Top region	Fire (experiment)	14.7%	35.2%
	Steel (experiment)	5.0%	12.1%
	Steel (FIRES-T3)	5.2%	12.7%
Middle region	Fire (experiment)	16.8%	21.5%
	Steel (experiment)	15.9%	13.8%
	Steel (FIRES-T3)	4.5%	11.0%
Bottom region	Fire (experiment)	16.0%	14.3%
	Steel (experiment)	9.5%	9.4%
	Steel (FIRES-T3)	0.8%	4.3%

### 3.5.2 Test of insulated steel tubes: comparison of two approaches

In the previous section, test of insulated steel rods was conducted to validate the scaling rules proposed. Only approach 1 was used in the experiment to design the insulating material on the steel rods. In approach 1, the same insulation as prototype is used, and the thickness of insulation is adjusted to obtain the similar effect of heating. This approach is the easiest one of the three approaches proposed. The experimental data show that satisfactory results are obtained.

In this section, instead of steel rods, tests of insulated tubes are conducted. The same steel tubes will be used to construct framed structures, and the frames will be tested in scaled fires which will be discussed in the next chapter. Two approaches (Approach 1 and 2) will be used to design the insulation on steel tubes, and their

results will be compared. This experiment provides guide and support to determine the approach which will be used for the structural fire testing of frames.

In Approach 1, the insulating material and thickness are determined according to “ $k_i \sim \rho_i \sim s^0$  and  $\delta_i \sim s^{-1/2}$ ”. In Approach 2, the insulating material and thickness are determined according to “ $k_i \sim \rho_i \sim s^{3/4}$  and  $\delta_i \sim s^{1/4}$ ”. The sectional size of a full-scale steel tube is  $101.6\text{mm} \times 101.6\text{mm}$  with thickness of  $12.7\text{ mm}$ . The dimensions cross sections of 1/4-scale and 1/8-scale tubes are shown in Figure 3.11. For approach 1, same insulation (Saffil LD mat) is used for both scaled models. The thickness for the 1/8-scale and 1/4-scale models is  $18\text{ mm}$  and  $12.7\text{ mm}$  respectively. For approach 2, Saffil LD mat is used for the 1/8-scale model, and Kaowool 3000 is used for the 1/4-scale model. The thickness for the 1/8-scale and 1/4-scale models is  $18\text{ mm}$  and  $21.1\text{ mm}$  respectively. The scaled tube columns are placed to the back corners in the compartments as shown in Figure 3.12. For each column, three K-type thermocouples are attached to the steel columns (denoted as top, middle and middle) to measure the steel temperature.

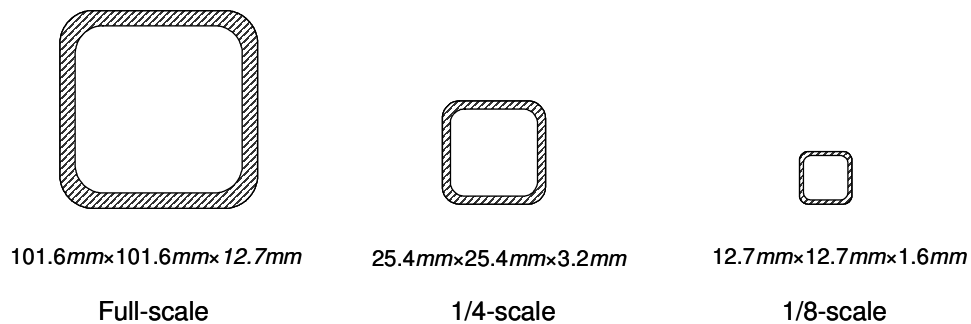


Figure 3.11 Dimensions of cross sections of scaled tubes



Figure 3.12 Experimental set-up of scaled insulated tubes

The temperature profiles of the steel tubes are shown in Figure 3.13, Figure 3.14, Figure 3.15 and Figure 3.16 for both small fires and large fires. They are plotted in the full-scale time ( $t_p = t_s / s^{1/2}$ ) for clear comparison. The results show that both Approach 1 and 2 result similar steel temperature profiles. Approach 2 requires a change of insulation materials in the scaled models. However, the required insulating material is not always available in practice. Approach 1 uses the same insulation for all scales, so this approach is more convenient in engineering practice. Only the insulation thickness is adjusted in the scaled models. For the structural fire testing discussed in the next chapter, Approach 1 will be used to determine the insulation on frames.

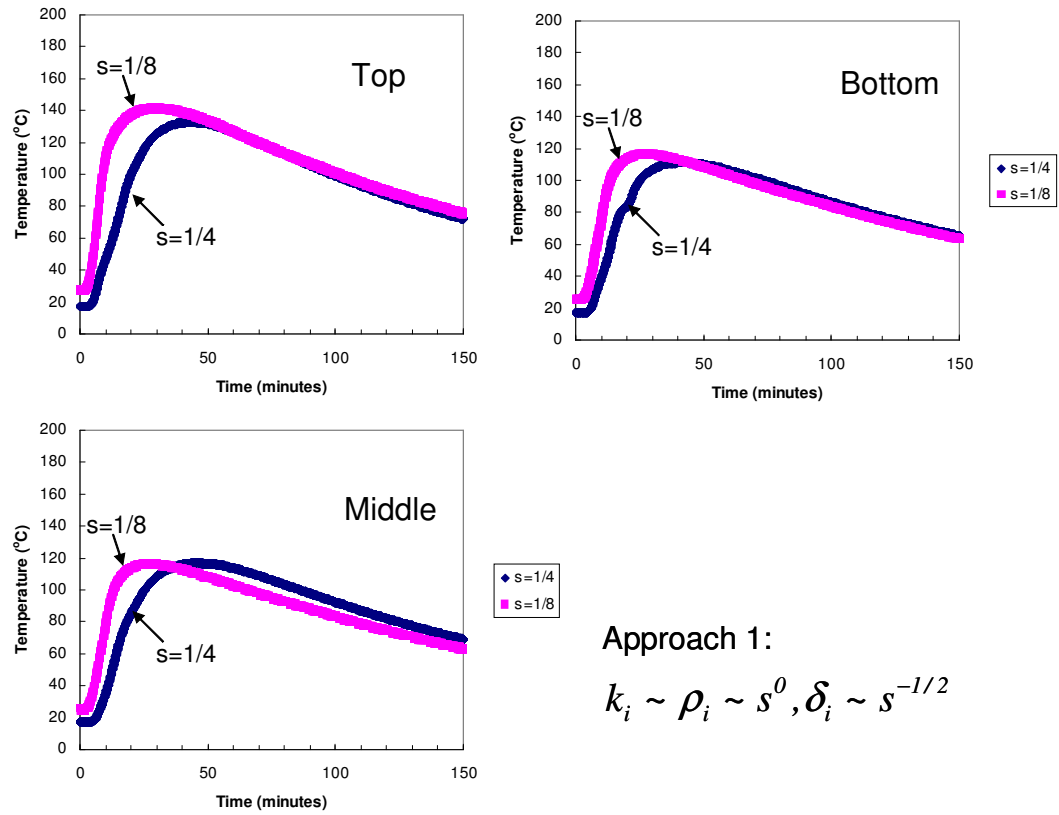


Figure 3.13 Temperature profiles of steel tubes for small fire (Approach 1)

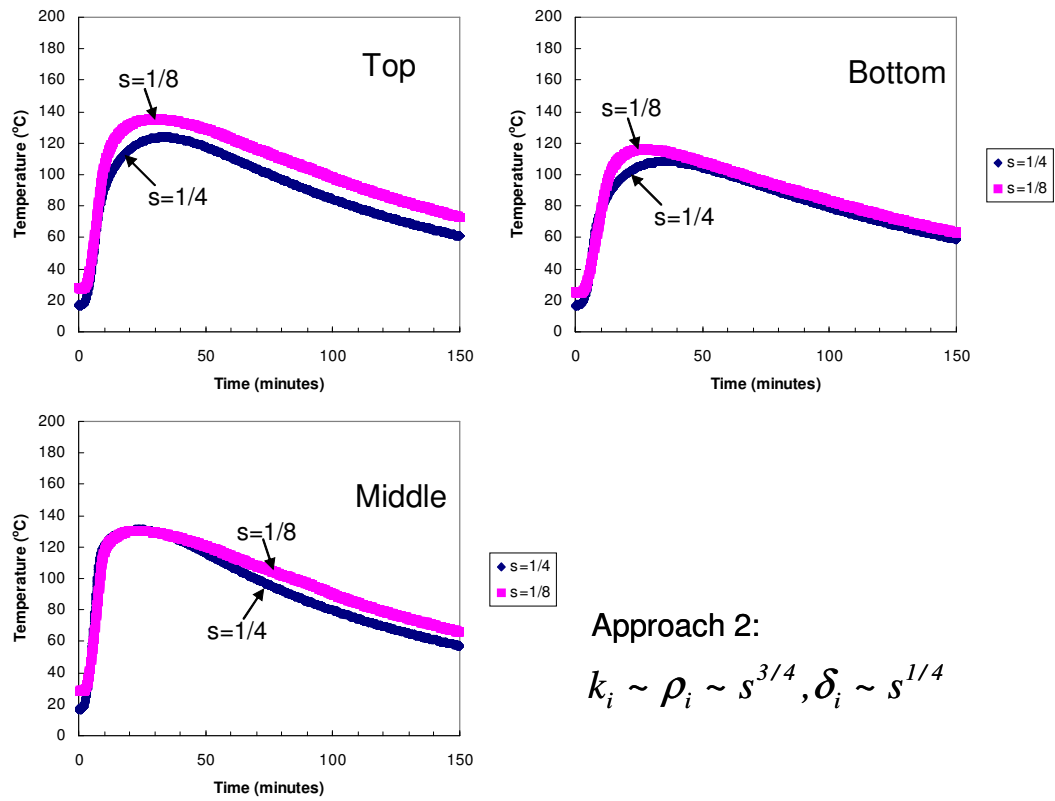


Figure 3.14 Temperature profiles of steel tubes for small fire (Approach 2)

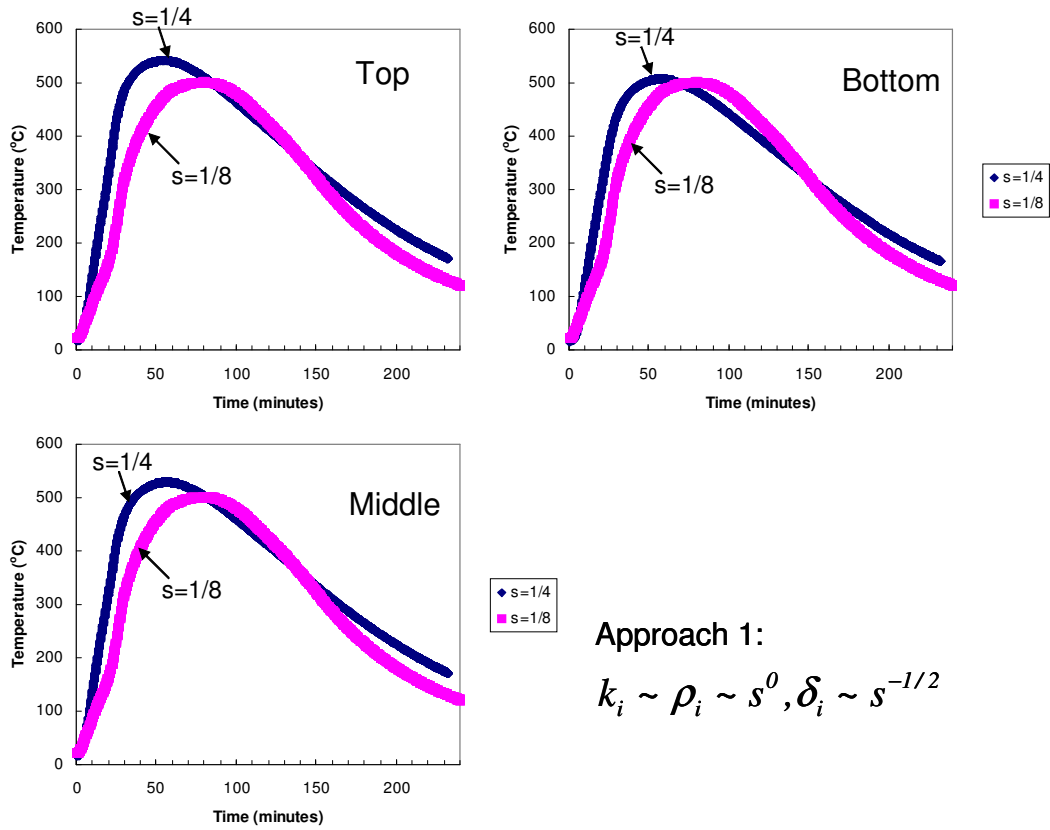


Figure 3.15 Temperature profiles of steel tubes for large fire (Approach 1)

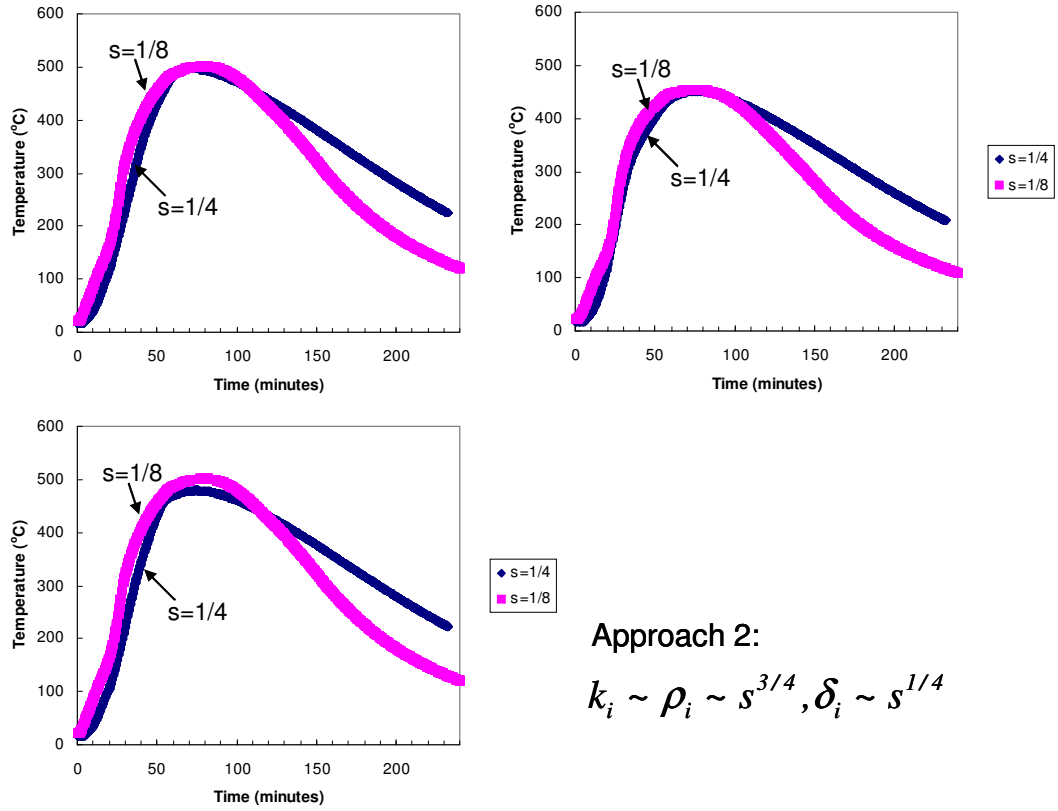


Figure 3.16 Temperature profiles of steel tubes for large fire (Approach 2)

## Chapter 4: Scaled model experiments of structures subjected to fire and gravity load

In this chapter, small-scale steel frame models are used to simulate the behavior of the full-scale structures exposed to fire as the utility of such an approach is significantly easier and more cost effective to perform than full-scale tests. Both fire and structure related parameters of the scaled models are designed based on length scale relationships derived from the governing equations of heat transfer. The wood crib fuel and the compartment wall materials are chosen properly in order to achieve a similar temperature profile as that of the prototype. The modeling of the wood crib fires in enclosures requires the burning time to be scaled by  $t \sim s^{1/2}$  ( $s$  is the scale factor), which is suitable for the compartment fires where the heat flow is driven by gravity or buoyancy force. Based on this time scale, specific requirements for the scaled structural and thermal modeling are developed. Some simplifying processes are adopted to make the scaled experiment possible. For example, the heating of the insulated steel frame is considered to be quasi-steady and the steel temperature is uniform. Moreover, the conduction is considered to be the dominant thermal resistance for heat transfer at solid boundaries over radiation and convection. Based on these assumptions, the scaling rules for the insulation on steel are obtained, in which the insulating material and the thickness are scaled rationally. Insulated steel frames are built and placed into the scaled compartment fires. Scaled structural loadings are applied to the frames externally in order to achieve similar strain and

stress. The structural response, such as the deflection of the beams, is also measured and observed.

#### 4.1 Construction of steel frames with insulation

A steel framed structure built with square tube members is considered as the prototype. The dimensions of steel tubes are shown in Figure 3.11. The small-scale frames are geometrically scaled as shown in Table 4.1. The insulation thickness and material are chosen according to Approach 1 discussed in Chapter 3. The same insulation is used for all scales. SAFFIL Alumina LD mat [89] with thermal conductivity  $k_0 = 0.11W / mK @ 400^\circ C$  and density  $\rho_0 = 40kg / m^3$  is considered as the insulation material used in the prototype. Figure 4.1 and Figure 4.2 show the steel frame before and after it is wrapped with insulation. The detail of the beam-to-column connection is illustrated in Figure 4.3. Angle plates are used as connections in order to limit the beam end rotation. Similar connection design is used for frames at different scales.

Table 4.1 Dimension of prototype and scaled models, and insulation applied

Scale	L (mm)	H (mm)	b (mm)	$\delta_t$ (mm)	$\delta_i$ (mm)	Insulation
1	3560	2440	101.6	12.7	6.4	SAFFIL LD mat
1/4	890	610	25.4	3.2	12.7	SAFFIL LD mat
1/8	445	305	12.7	1.6	18.0	SAFFIL LD mat

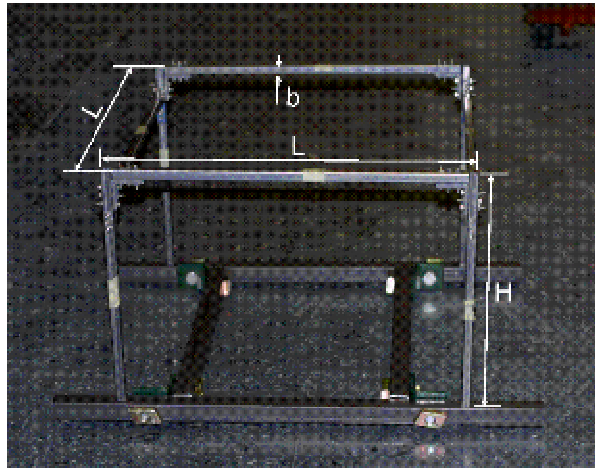


Figure 4.1 Typical steel frame before insulation is applied



Figure 4.2 Steel frame with insulation applied

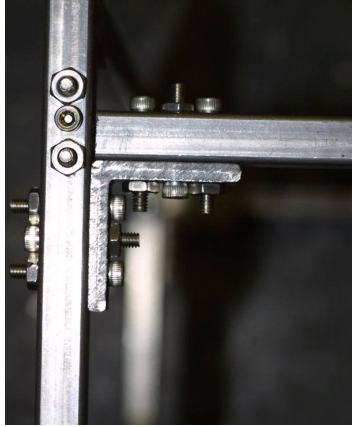


Figure 4.3 Detail of beam-to-column connection



Figure 4.4 Insulated frame placed in compartment

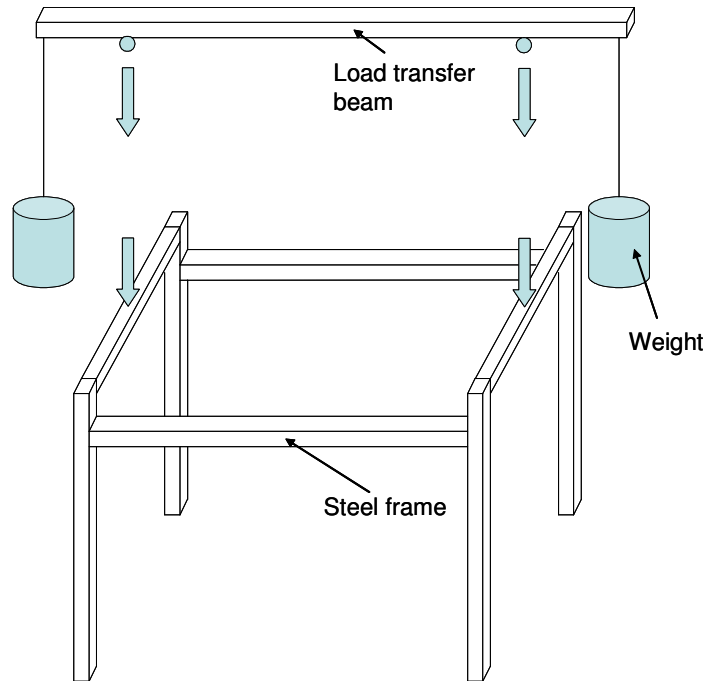


Figure 4.5 Schematic drawing of structural loading on the frame



Figure 4.6 Vertical loading applied to frame by hanging weight

The steel frames with insulation are placed into fire compartments as shown in Figure 4.4. Gravity load is applied externally to the two parallel beams of the frame by hanging weight to an external beam as shown in Figure 4.5 and Figure 4.6. Total 127 kg weight is applied to the 1/4-scale model, and 31.8 kg is applied to the 1/8-scale model. Figure 4.7 shows the experimental set-up of the insulated steel frames with

structural loading. The steel temperature of both beams and columns is measured, and twenty K-type thermocouples are installed in each frame. Both small and large fires are conducted in each compartment, and beam deformation is recorded.

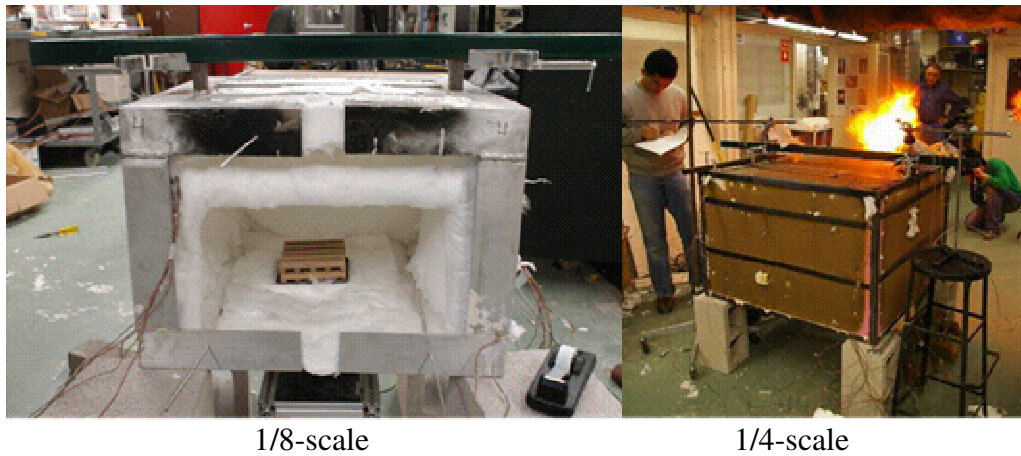


Figure 4.7 Experimental set-up of tests of steel frames

#### 4.2 Experimental results of frame testing in fire

In addition to the gravity loads on the structure, the effect of temperature is the predominant effect that results from the fire. Both maximum steel temperature and temperature-time curves play important roles on the structural response of a structure exposed to fire. Figure 4.8 shows the typical temperature profiles of the beam and column in both small and large fires. The steel temperature is plotted in the full-scale time ( $t_p = t_s / s^{1/2}$ ) for clear comparison. Steel temperature profiles are obtained in 1/8 and 1/4 scales experiments. Note that the steel temperature profiles of the 1/8-scale model in the large fire are shifted to the right compared to that of the

1/4-scale model. This shift can be traced back to the hot gas temperature profiles as shown in Figure 2.20 which shows a similar shift. The lower hot gas temperature in the 1/8-scale model reduces the rate of steel temperature change. Consequently, the steel temperature profiles in the 1/8-scale model drifted, and the time to reach the peak steel temperature is delayed. The hot gas temperature profiles in the small fire in Figure 2.19 show good agreement with results at different scales, and the time to reach peak temperature at different scales is also very close. As expected, the steel temperature profiles in the small fire at different scales compare very well as shown in Figure 4.8 (a).

Figure 4.9 shows the deflection of the beams under combined gravity load and temperature. The positive value of beam deflection in the plots indicates downward deflection. The results show that the deflection profiles at different scales compare very well in the small fire as shown in Figure 4.9(a). The maximum steel temperature in the small fire (Figure 4.8(a)) is less than 200 °C. The deflection is elastic as there is no permanent deflection after the room temperature is restored. The upward beam deflection is due to the thermal expansion of columns.

The maximum steel temperature in the large fire (Figure 4.8(b)) is about 500 °C. Figure 4.9(b) shows the deflection profiles in the large fire. The deflection in the beams is upward at the early stage and it becomes downward when the effect of steel degradation becomes greater than the effect of the thermal expansion of the columns. Unrecoverable deflection is formed in the beams in the large fires.

### 4.3 Conclusion

The experimental results show that the tests of scaled structures in scaled fires can be used to simulate the behavior of a prototype exposed to fire. Steel temperature profiles under both the small and large fire scenarios at different scales compare well. Similar structural response (deformation of beams) is obtained in the two scaled frames subjected to combined gravity and fire loads.

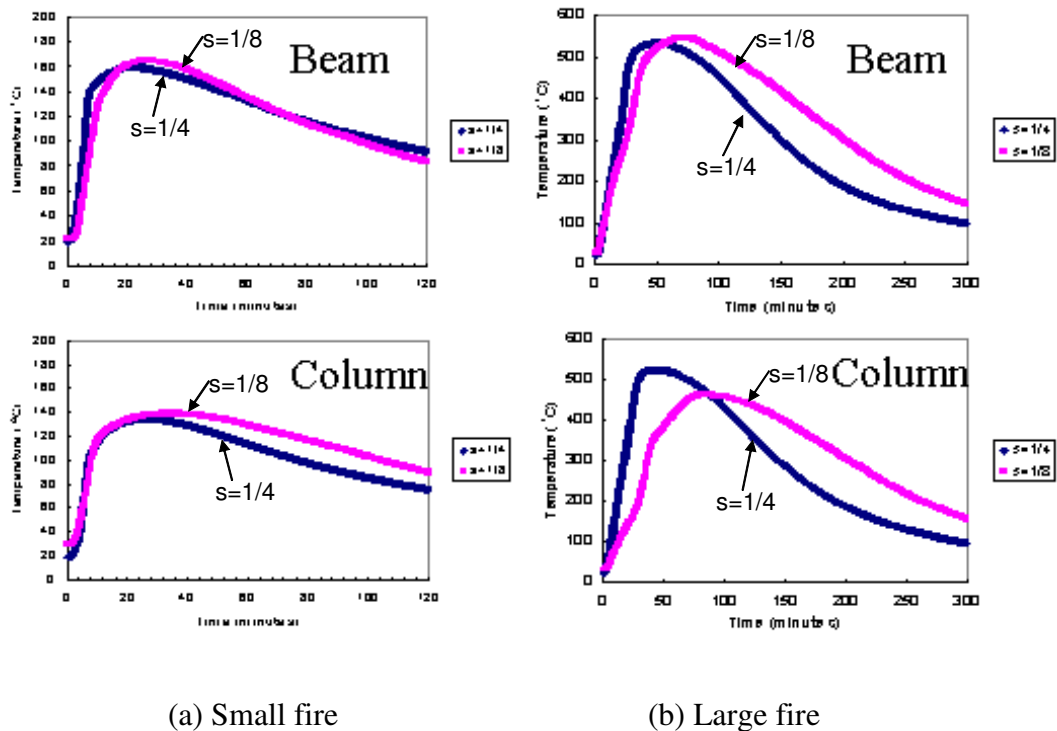
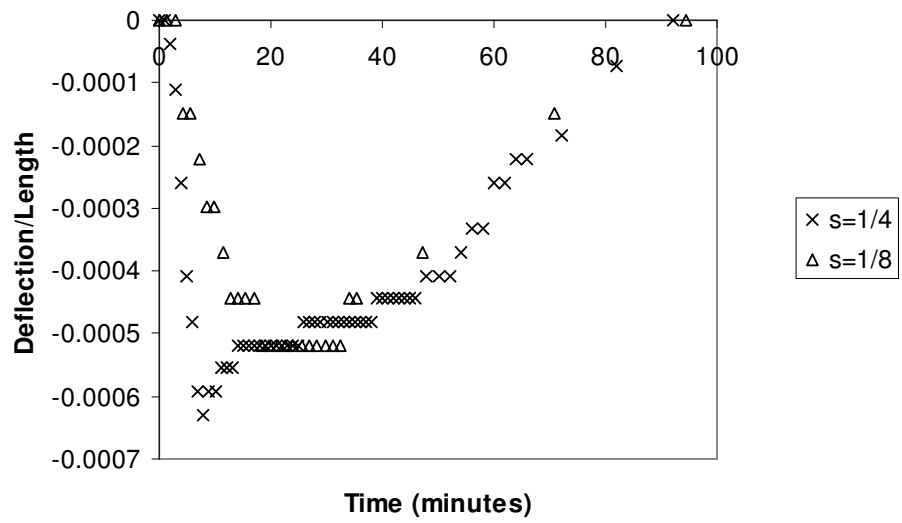
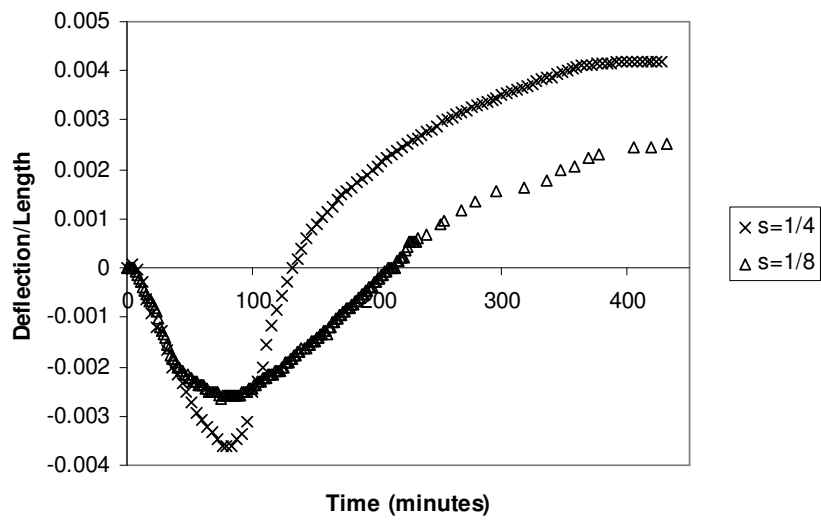


Figure 4.8 Typical steel temperature profiles in the frames, temperature vs. full-scale time



(a) Measurement in small fire



(b) Measurement in large fire

Figure 4.9  $\Delta y/L$  of steel beams vs. full-scale time

## Chapter 5: Failure prediction by use of scaled models

The previous chapters proposed scaling rules for design of scaled compartment fires, scaled structures, and insulating materials on structural members. Numerical simulation and fundamental experiments are conducted to validate the proposed scaling rules. Results show that scaled models can be used to simulate the behavior of a prototype by following proper scaling rules. This chapter focuses on the feasibility of using scaled models to predict structural failure in fire.

Fully-developed fires in a building can be disastrous. The collapse of World Trade Center Tower 1, 2 and 7 shows that the global stability and failure of a tall building can result from fire and structural configurations. The investigation of the performance of the buildings in the World Trade Center site conducted by Federal Emergency Management Agency (FEMA) [1] suggested that the behavior of a structural system under fire conditions should be considered as an integral part of the structural design. The bottom line of structural fire safety design is to provide sufficient fire resistance so that the global collapse of a building under an extreme fire disaster can be prevented. Therefore, one critical question needs to be answered is “whether and how long a structure is going to survive in a fire?” The current Fire Resistance Rating (FRR) based design method can not give a convincing answer. An integrated design tool is needed to predict the heating conditions in a fire, the heating process in structural members, and the response of structural systems. Sophisticated computational models are usually used for this purpose. However, the computing effort and the lack of experimental validation limit its use in practice. Numerical

modeling of structural failure can also be difficult at times because of convergence problems, differentiating between local and global failures in numerical models, modeling of fire-induced phenomena (concrete spalling, insulation burned-off, and movement of flame and smoke). Physical modeling is a good alternative to mitigate these difficulties, especially when small-scale models are used, because of the reduced cost and the relative easy of operation.

This chapter investigates the feasibility of a new technique based on scale modeling that is used to predict the failure in a structure exposed to fire. A methodology of conducting small-scale structural fire testing is provided. Small-scale tests of insulated steel beams exposed to fires are conducted at two different scales.

### 5.1 Scale modeling of structural failure

In order to predict structural failure in fire, one needs to understand the important factors in a fire disaster. First, the fuel load needs to be determined in the prototype. For example, the fuel in an office building is mainly wood or plastic furniture which is very different from the fuel in a warehouse where various combustible materials may be stocked. Therefore, the possible fuel load needs to be estimated because it determines the fire profile in the prototype. Another important factor involved in the fire growth is the configuration of ventilation which is usually related to the size and number of windows and doors in a building. Ventilation may change over time in a fire disaster as some of the covering is compromised. For example, the amount of oxygen can be limited in a room at the beginning stage of a fire when the windows and doors are closed. As temperature rises in the room, the

increasing pressure and heat may break the glass windows, so that fresh air can enter the room and contribute to the fire growth. The third factor important to model the fire correctly is the boundary condition of a fire. For a fire in a building, the boundary condition includes the wall and floor materials and their thickness. The heat loss through the boundaries can affect fire temperature in a compartment significantly. Another factor is water spray from sprinklers if they are assumed to be working normally, and the effect can also be taken into account in scale modeling [85, 92].

The most severe type of structural failure is a global collapse which is usually initiated by the loss of some load bearing structural members. A progressive collapse then follows if the structure is not appropriately designed. A successful scaled model should replicate the behavior of the prototype. In order to evaluate the similarities between the scaled model and the prototype, five failure criteria are defined: failure mode, failure mechanism, critical temperature, critical loading and failure time.

*Failure mode* in the scaled model should be similar to that of the prototype. It represents the status of structural failure. For example, a portal frame may fail in sidesway or vertical modes. The sidesway collapse in the prototype should be reproduced in the scaled model. With similar structural loading and constraint conditions, the failure mode in the model and prototype should be consistent. That means that the weak points discovered in the testing of scaled models should suggest the existence of similar weak points in the prototype.

*Failure mechanism:* The global failure of a structure in fire can sometimes be caused by a series of local damage such as local yielding, connection failure, and

column buckling. The failure mechanism is the cause and effect relationship involved in the structural failure.

*Critical temperature* at which the scaled model starts to fail globally should be similar to that of the prototype. The prediction of critical temperature in structural members helps engineers to determine appropriate protections for a structural system.

*Critical loading* is the combined maximum loading from gravity and fire. The critical gravity load is the maximum structural loading which can be applied to a structural system in addition to a designed fire. The critical fire loading indicates the extreme fire scenario under which a structural system can still survive in addition to a designed gravity load.

*Failure time* is the time at which a structural system reaches its failure, critical temperature or critical loading. Since the time from the starting of global failure to the totally demolition is usually short, the failure time can be defined as the time global failure initiates. For example, the failure time of World Trade Center 1 can be identified as the time at which the exterior columns at the Southwest corner started to buckle inward and the upper part of the tower above 98<sup>th</sup> floor started to tilt to Southwest corner. The failure time in the models and the prototype should follow a consistent scaling rule.

The structural response of a structural system in fire is relatively complex. Fire-induced physical phenomena (e.g. concrete spalling) have not yet been well understood. And the loading and constraint conditions applied to the structural system change dynamically. One significant factor in structural response in fire is the change in boundary restraints [36, 93]. For example, local buckling of lower flanges may

occur at very low temperature in an I-shape steel beam if the axial constraint is high. Lateral bracing on a beam can be critical to prevent global buckling (bending and lateral torsional buckling). Connection failure can initiate significant change of boundary restraint of the adjacent structures. Occurrence of catenary or membrane action in a beam or floor can generate high pulling forces on columns or walls so that the load capacity of vertical members will be greatly reduced. Therefore, boundary conditions similar to those of the prototype should be applied to scaled models in order to pursue a similar structural behavior as that of the prototype.

## 5.2 Similitude relation of structural failure

### 5.2.1 Local buckling

The failure of a structure in fire is usually a progressive process which may involve a series of failure of individual structural members and connections before the structure reaches the status of global failure. Local buckling can occur at a very early stage of fire. The critical stress of local buckling can be written as [94]:

$$\sigma_{lb} = \frac{k\pi^2 E}{12(1-\mu^2)(b_f/t_f)^2} \quad (5.1)$$

$k$  is a constant which depends on supporting conditions, length/width ratio and the nature of loading [94]. If the structural member is geometrically scaled

( $b_f/t_f \sim s^l/s^l \sim s^0$ ) and its material is the same as that in the prototype ( $E \sim s^0$ ),

the local buckling stress should be scaled according to  $\sigma_{lb} \sim s^0$ . Therefore, the

occurrence and the location of local buckling in the scaled model and the prototype

should be consistent. The occurrence of local buckling in a structural member does not necessarily indicate a global structural failure. However, the effect due to local buckling should be included since it may initiate the development of large curvature and deflection.

### 5.2.2 Elastic buckling

The critical load of elastic buckling can be written as:

$$F_{eb} = \frac{\pi^2 E_T I}{L^2} \quad (5.2)$$

$E_T$  is the elastic modulus at elevated temperatures which can be obtained from ASTM E119 standard [13]:

$$E_T = \begin{cases} \left[ 1 + \frac{T}{2000 \ln(T/1000)} \right] E_0 & \text{for } T \leq 600^\circ C \\ \left[ \frac{690 - 0.69T}{T - 53.5} \right] E_0 & \text{for } T > 600^\circ C \end{cases} \quad (5.3)$$

The external loading on a scaled model is scaled according to  $P \sim s^2$ . If same material is used for all scaled, and structural models are geometrically scaled,

$E_T \sim s^0$  and  $I \sim s^4$ . From Equation 5.3, the critical temperature at which a structural member fails due to elastic buckling is scaled according to:

$$T_{eb} \sim s^0 \quad (5.4)$$

That means the failure temperature in the scaled model should represent the failure time in the prototype.

### 5.2.3 Lateral torsional buckling

Figure 5.1 shows a beam model with lateral torsional buckling. The bending moments at both ends of the beam are the only external loads. The equilibrium relations of bending and torsional moment can be written as [94]:

$$-E_T I_x \frac{d^2 v}{dz^2} = M_x \quad (5.5)$$

$$-E_T I_y \frac{d^2 u}{dz^2} = M_x \sin \beta \approx M_x \beta = M_x \frac{du}{dz} \quad (5.6)$$

$$GJ \frac{d\beta}{dz} - E_T C_w \frac{d^3 \beta}{dz^3} = M_x \frac{du}{dz} \quad (5.7)$$

$C_w$  is the warping stiffness.  $M_x$  is the moment around x-axis.  $u$  and  $v$  are the deflections in lateral and vertical directions, respectively.  $\beta$  is the section rotation in the x-y plane. From Equations 5.5 to 5.7, the governing equation for lateral torsional buckling can be written as:

$$E_T C_w \frac{d^4 \beta}{dz^4} - GJ \frac{d^2 \beta}{dz^2} - \frac{M_x^2}{E_T I_y} \beta = 0 \quad (5.8)$$

The external bending moment is scaled according to  $M_x \sim s^3$ . The dimensional relation in Equation 5.8 is preserved if  $\beta \sim s^0$ . Therefore, the buckling shape in the scaled model should be similar to that in the prototype.

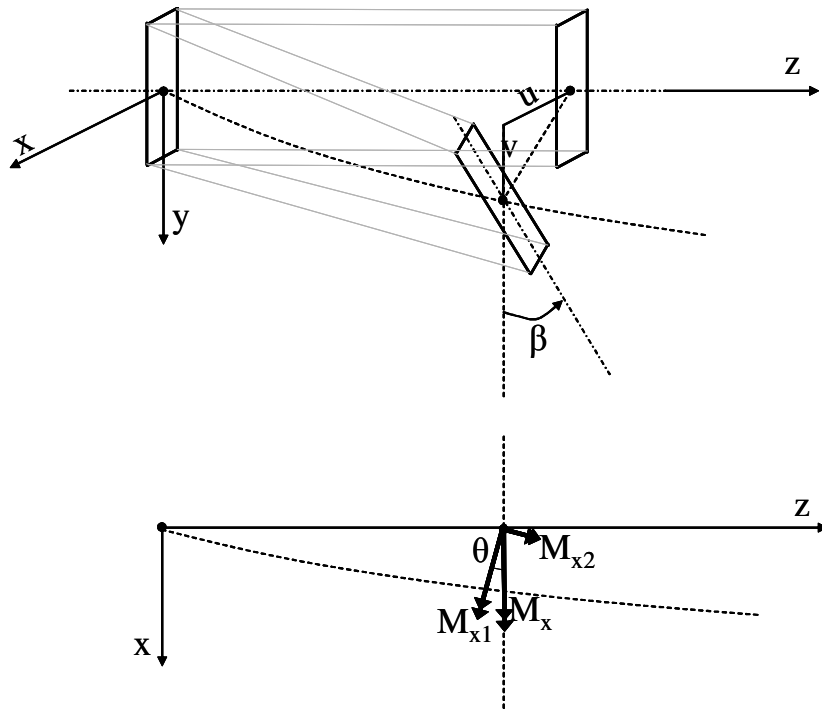


Figure 5.1 Beam model with lateral torsional buckling

### 5.3 Similitude relation of fire, structures, and insulation

Scale modeling of fire and its use for structural fire testing have been presented in Chapters 2, 3 and 4. A summary of scaling rules for the design of a structural fire testing is listed in Table 5.1. The fire compartment and the structure are both geometrically scaled, and the time is scaled according to  $t \sim s^{1/2}$  (Equation 2.10). The scaling rules in Table 5.1 can be followed to design fire and structures, and the results from the test of the scaled model should be similar to that of the prototype.

Table 5.1 Scaling rules for fire, insulation and structures

Design parameters	Scaling rules	Preserved groups
Scaling rules for fuel design (wood cribs)		
Thickness of wood sticks, $b_c$	$b_c \sim s^{1/3}$	
Spacing between wood sticks, $s_c$	$s_c \sim s^{1/3}$	
Length of wood sticks, $L_c$	$L_c \sim s^{7/6}$	$\Pi_{los} = \frac{\dot{q}}{\rho_\infty c_p T_\infty \sqrt{g} s^{5/2}}$
Number of layers, $N_c$	$N_c \sim s^{1/3}$	
Number of wood sticks per layer, $n_c$	$n_c \sim s^{5/6}$	
Scaling rules for compartment design		
Wall material, $k_w$ and $\rho_w$	$k_w \rho_w \sim s^{3/2}$	$\Pi_{w,k} = \frac{(k_w \rho_w c_w)^{1/2} s^2 T_\infty}{\rho_\infty c_p T_\infty \sqrt{g} s^{5/2}}$
Thickness of wall, $\delta_w$	$\delta_w \sim s^{1/4} \left( \frac{k_w}{\rho_w c_w} \right)^{1/2}$	$\Pi_{w,\delta} = \frac{\delta_w}{\left[ \left( \frac{k_w}{\rho_w c_w} \right) s^{1/2} \right]^{1/2}}$
Scaling rules for insulation on steel structures		
Properties of insulation, $k_i$ and $\rho_i$	$k_i \sim \rho_i \sim s^0$	$\Pi_i = \frac{k_i}{\delta_i^2 \rho_i} s^{1/2}$
Thickness of insulation, $\delta_i$	$\delta_i \sim s^{-1/2}$	$\Pi_s = \left( \frac{k_i}{\delta_i} \right) \left( \frac{1}{s^{1/2}} \right)$
Scaling rules for structures		
Structural loadings, $P$ and $M$	$P \sim s^2, M \sim s^3$	
Boundary constrain, $K$	$K \sim s$	

#### 5.4 Methodology of failure prediction by using scaled models

Figure 5.2 shows the schema of the methodology of using scaled model to predict structural failure in fire. The first task is to assess the conditions of the prototype which includes determining a fire scenario and obtaining information of structures and insulating material on structural members. The fire scenario can be determined based on the information of the combustible contents, ventilation configuration, and structural types. The ventilation can change over time during a fire, and it has to be taken account of in the scaled model. The structural loading on a structure needs to be determined according to the real loading condition in a fire disaster. Boundary constraints on a structural system need to be evaluated carefully, and their conditions changing over time during a fire should also been taken into account. By using the scaling rules, a scaled model can be built and tested. Both fire behavior and structural response can thereby be obtained. These results should represent the behavior of the prototype. Therefore, the structural performance and structural failure can be simulated and predicted by conducting a scaled model testing.

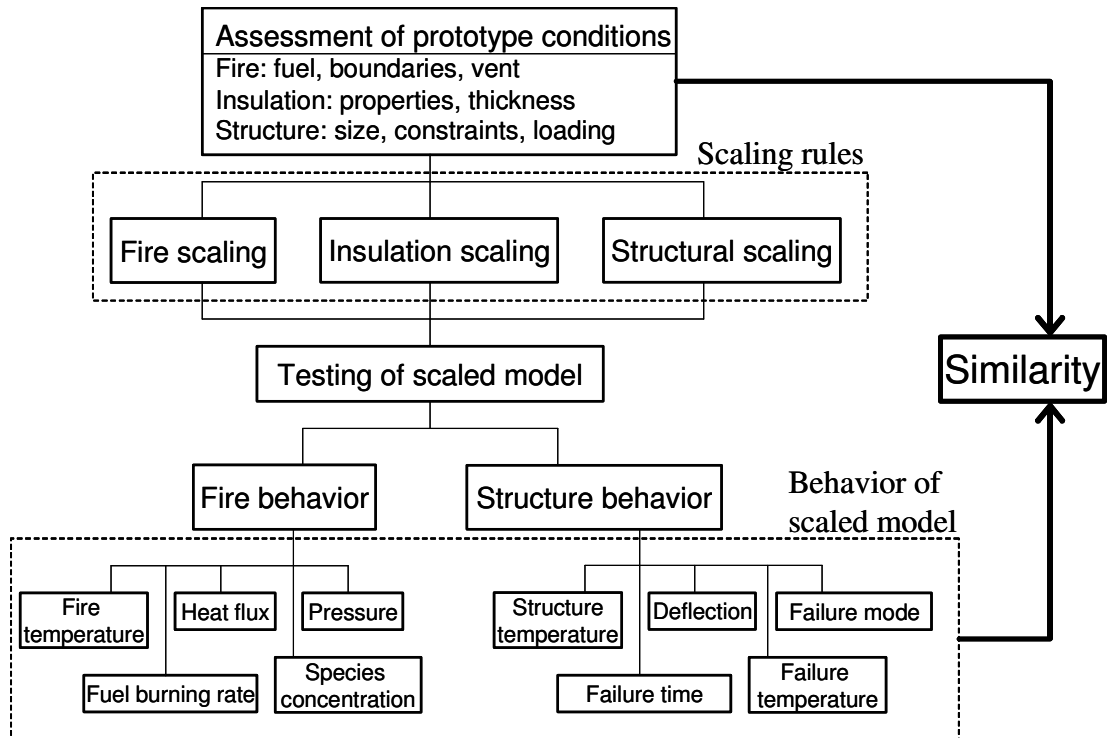


Figure 5.2 Schema of methodology for failure prediction

### 5.5 Failure tests of beams in scaled compartment fires

A building room with  $3.7\text{m} \times 3.7\text{m}$  floor and  $2.44\text{ m}$  height is considered as the prototype. The burning of wood cribs in the two small scales ( $1/8$ -scale and  $1/4$ -scale) is to simulate a one-hour burning of the prototype. Two compartment fires are conducted at  $1/8$  and  $1/4$  scales. Scaling rules as shown in Table 5.1 are used to design the wood cribs and to determine the properties and thickness of compartment walls. Saffil LD mat [89] was used as the wall material to built the  $1/8$ -scale compartment and Kaowool 3000 [90] for  $1/4$ -scale compartment. The density of Saffil LD mat is  $208\text{ kg/m}^3$ , and the density of Kaowool 3000 is  $40\text{ kg/m}^3$ . The

thickness of the compartment wall of 1/8-scale model is 34 *mm*, and the thickness of the compartment wall of 1/4-scale is 13 *mm*.

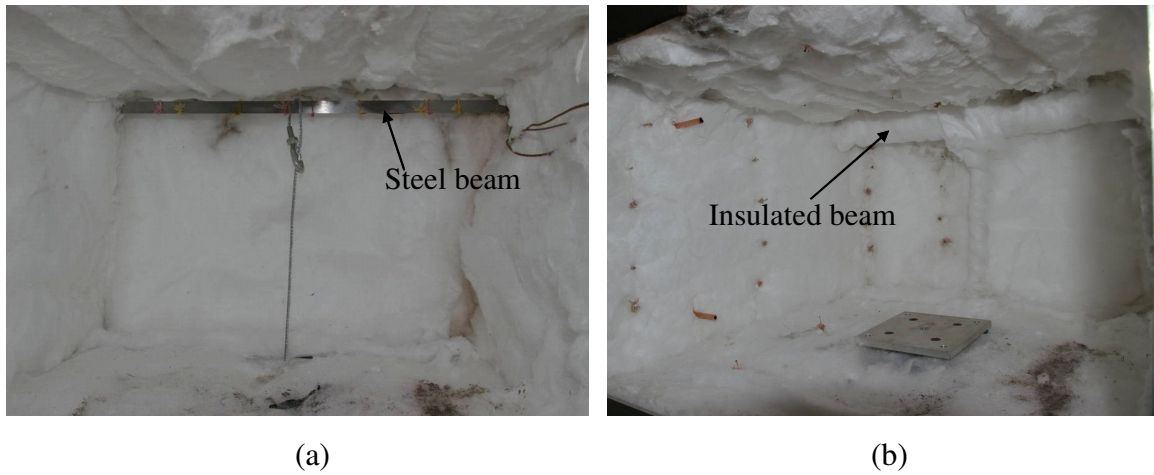


Figure 5.3 Steel beam before and after insulation applied

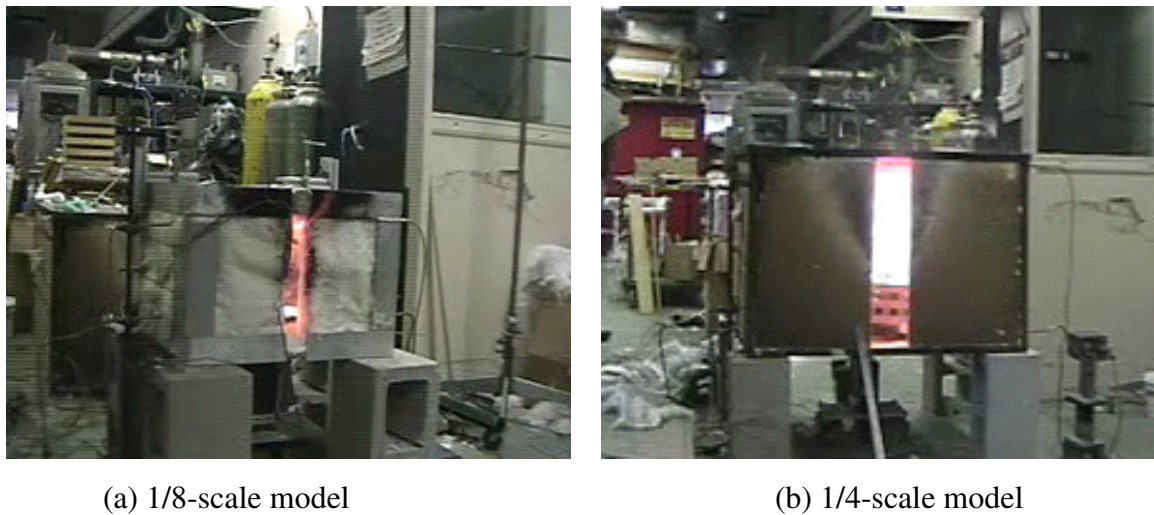


Figure 5.4 Experimental set-up of failure testing

Steel with rectangle sections are used in the experiment. The dimension of the 1/4-scale beam is 3.2 $mm$  $\times$ 25.4 $mm$  $\times$ 1067 $mm$  (width $\times$ depth $\times$ length), and the dimension of the 1/8-scale beam is 1.6 $mm$  $\times$ 12.7 $mm$  $\times$ 533 $mm$ . The beams are simply-supported, and they are loaded by a vertical point force at mid-span. The external load is scaled according to Equation 3.10. 4.5 *kg* (10 *lbs*) weight is applied on the 1/8-scale

beam, and 18.1 kg (40 lbs) weight is applied on the 1/4-scale beam. The steel beams are insulated, and the thickness of the insulation is determined according to the scaling rules shown in Table 5.1. Figure 5.3 shows the steel beam placed in the compartment. Both steel temperature and hot gas temperature are measured by using K-type thermocouples. The experimental set-up of the tests of scaled models is shown in Figure 5.4. The time and the temperature at which the steel beams reach the status of lateral torsional buckling are also recorded.

Figure 5.5 shows the typical hot gas temperature profiles in compartments at two different scales. They are plotted in the prototype time scale ( $t_p = t_m / s^{1/2}$ ). Lateral torsional buckling was observed in both 1/8-scale and 1/4-scale testing, and the failure time and failure temperature were recorded. Figure 5.6 shows the steel temperature profiles, and they are plotted in the prototype time. The 1/8-scale beam failed at 27 minutes (prototype time) and 550 °C. The 1/4-scale beam failed at 18 minutes (prototype time) and 565 °C. The results show that the failure temperatures at two scaled models compared well. The difference in failure temperature is within 3% of each other. However, the failure times for the two scaled models are not very close, and the relative difference is approximately 50%. This difference is due to the error of the scaled fires as shown in Figure 5.5 where the fire temperature of 1/8-scale model is lower than that of 1/4-scale model before 30 minutes. This corresponds to the lower steel temperature of the 1/8-scale model from  $t = 0$  to  $t = 35$  minutes as shown in Figure 5.6. So the time to reach the failure temperature in the 1/8-scale beam is delayed.

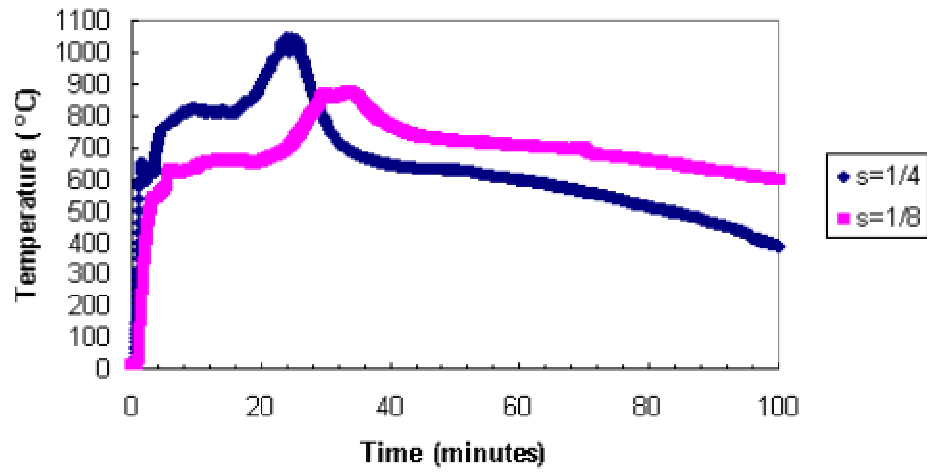


Figure 5.5 Typical hot gas temperature profiles in two compartment fires

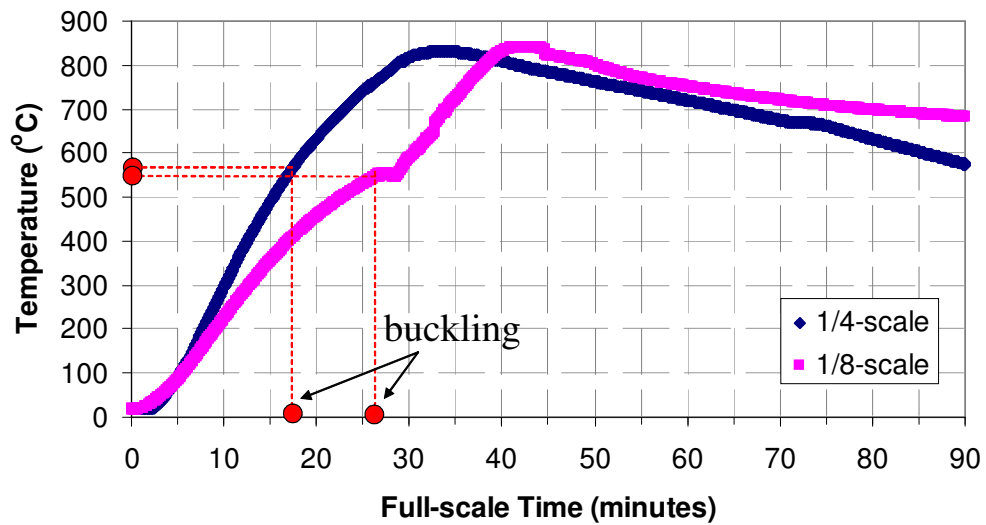


Figure 5.6 Steel beam temperature profiles v.s. full-scale time

## 5.6 Conclusion

This chapter focuses on the feasibility of using scaled model to predict structural failure in a fire disaster. The important factors involved in fire behavior and structural response are discussed, and their scaling rules are presented. The similarity relations for structural failure such as local buckling, elastic buckling, and lateral torsional buckling are discussed. This chapter gives a big picture of implementation of scale modeling in structural fire testing, and the methodology is discussed in details.

Tests of steel beams are conducted in two scaled compartment fires (1/8-scale and 1/4-scale) with vertical loading applied, and both steel beams at two scales reached the failure of lateral torsional buckling during the fire. The failure temperatures of tests at two different scales compare well and the relative difference is within 3%. The relative difference of the failure times is approximately 50%. This difference can be traced back to the difference of the fire temperature profiles of the two compartment fires. Although the results are not quantitatively perfect, the experimental results show that it is feasible to use scaled models to predict structural failures.

## Chapter 6: Investigation of World Trade Center Tower 1

### collapse based on tests of scaled model

The September 11 event showed that the combined effects of fire and structural loading on a high-rise building can be disastrous. Understanding the mechanism of structural damage caused by fire will help engineers design safer infrastructures and reduce the loss from fire disasters. The catastrophic collapse of the towers and the possible collapse hypotheses have been studied and discussed by a number of studies. Bažant and Zhou [95, 96] have presented a simplified analysis of the overall collapse of the World Trade Center towers and proposed a dynamics consequence of the buckling of heated columns. Quintiere *et al.* [97] have analyzed a single web member of the floor truss system and concluded that the insufficiency of the insulation on the floor trusses appear to be the root cause of the collapses. Astaneh-Asl [98] has proposed the hypothesis for the cause of collapses based on his field investigation and analysis and also pointed out that the collapses could be avoided or delayed if there had been better fireproofing applied on the structural systems. Usmani *et al.* [99] focused on the structural mechanisms that initiated the failure of the towers and concluded that the collapse was triggered by the instability of the structural systems under the combined effects of the thermal expansion and the material degradation at high temperature. They conducted 2D finite-element numerical analyses of the floor and exterior column systems to study the behavior of the structural systems subjected to generalized exponential fire temperature-time curves with an arbitrary ‘rate of heating’ parameter, and the authors pointed out that

the structures would not have survived in a similar fire even if there had been no initial structural damage caused by the airplane impact. The extended results from a nonlinear analysis and the findings on collapse mechanism have been presented by Usmani [100] who concluded that the insufficient lateral support capacity of the floor system could have triggered the collapse. Quintiere [101] reviewed the hypothesis of the collapses and estimated the fire conditions in the towers. Moreover, he performed an analysis of insulated steel elements with consideration of the possible lost insulation due to impact.

Federal Emergency Management Agency (FEMA) [1] conducted investigations to study the performance of the buildings at the World Trade Center site and developed an understanding of the response of each affected building. Recommendations on improving design guidance and tools have also been given by FEMA. National Institute of Standards and technology (NIST) has completed a more thorough investigation to “determine why and how WTC1 and WTC2 collapsed following the initial impacts of the aircraft and why and how WTC7 collapsed” and to “identify areas in current building and fire codes, standards, and practices that warrant revision” [79]. The NIST study concluded that “the collapses of the towers were initiated by the combined effects of structural and fireproofing damage from aircraft impact and the subsequent intense fires,” and either the impact damage or the fire alone would not have caused the collapse of the towers.

Studies in references [1, 95-101] have applied comprehensive analytical simulations and calculations, and the results obtained have been compared to the field investigation or visual evidences recorded during the September 11 events. Since all

the hypotheses for collapse of the WTC towers are based on the elevated temperature in the structural members when they were exposed to the fire, the analysis for predicting the steel temperatures of floor trusses and columns is particularly important. In references [1, 97, 99, 101], the steel temperatures have been estimated based on the characterized fire conditions (temperature vs. time curves), and these results provided an understanding on the effects of insulation and fire scenarios. However, the time-temperature profiles in these analyses do not compare well to the actual time scale of the September 11 events, especially if the fire spreading in the towers were to be considered. One way to reduce questions on the fire loading and heating time is to conduct a physical model to reconstruct the World Trade Center fire. NIST conducted a series of large-scale tests to study the thermal response of floor trusses and exterior columns under fires ranging between 1.9 MW and 3.4 MW by burning liquid hydrocarbon fuels [79]. These tests provided valuable data to assess the accuracy of the computational models developed in NIST Fire Dynamic Simulator (FDS), NIST Fire-Structure Interface (FSI) and finite-element software package ANSYS. However, fire propagation was not in the scope of these tests and the time in the fire and steel temperature profiles is not necessarily representative to the actual time scale in the September 11 events. NIST has also conducted investigation and tests to estimate the fuel load in the tenant spaces. NIST's estimation of the fuel load is approximately  $20 \text{ kg/m}^2$  which is considered to be too low by the authors. Stewart [102] has done a thorough analysis of the fuel load calculation for the 96<sup>th</sup> floor of the WTC1, and  $50 \text{ kg/m}^2$  has been suggested.

Physical modeling approach was undertaken as an alternative to computational models used by other investigators. A small-scale model was built to simulate the fire and the structural response of the 96<sup>th</sup> floor of the WTC1. The fire propagation on the 96<sup>th</sup> floor is demonstrated. The thermal environment and the associated heating of structural members in the scaled model represent the fire conditions and the thermal response of the structural systems in the 96<sup>th</sup> floor of the WTC1 under the actual time scale of the September 11 events. Law of similarity was used to design and determine the enclosure boundaries of the floor compartment, the fuel loading on the floor, the structural systems, and the fire-proof materials on the structures.

### 6.1 Construction of scaled model

In the previous chapters, the scaling rules used for structural fire testing are proposed and validated by experiments. In this chapter, the design of the test follows the scaling rules to pursue the similarity between the small-scale model and the prototype.

The 1/20-scale model used in the experiment is geometrically scaled according to the dimension of the 96<sup>th</sup> floor of the WTC1. The final dimension of the model is  $3m \times 3m \times 0.15m$  ( $10ft \times 10ft \times 0.5ft$ ). The damage areas of the north exterior wall, floor and core caused by airplane crash are determined according to the estimates of damaged areas in WTC1 reported by FEMA [1] and NIST [79]. Figure 6.1 shows the 1/20-scale floor model. The initial damage caused by airplane crash is represented by an opening in the exterior walls, floor and core. This opening is

important in the fire propagation because the initial ventilation conditions play a significant role on the growing and spreading of the fire.

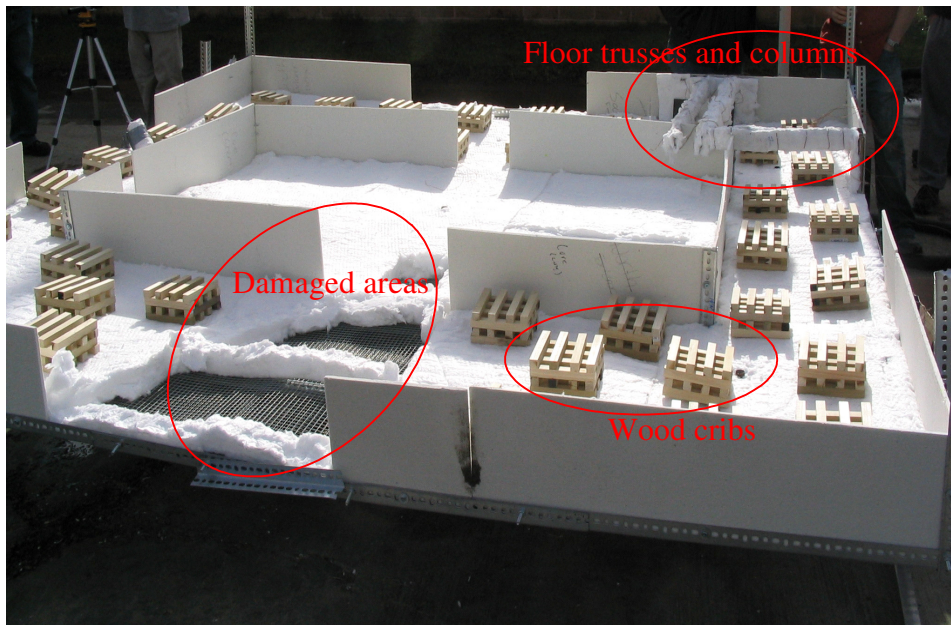


Figure 6.1 The 1/20-scale floor model

### 6.1.1 Wood cribs and jet fuel

The fire power in a scaled model should be scaled according to  $\dot{Q} \sim s^{5/2}$ . A typical office fuel load ranges from  $20 \text{ kg/m}^2$  to  $60 \text{ kg/m}^2$  or higher for storage areas.  $50 \text{ kg/m}^2$  was assumed based on the survey of the 96<sup>th</sup> floor and the fact that 170 4-drawer lateral files should be included [102], and this is used to determine the total amount of the wood used in the scaled model. The burning time of WTC1 is estimated to be approximately 120 *minutes* based on the evidence that flame was observed at the time of collapse (102 *minutes*), and based on the estimation by Quintiere [101]. Using the floor area of  $2873 \text{ m}^2$  (without the core area), the approximate burning rate in WTC1 is estimated to be

$$\dot{m} \approx \frac{m}{t} = \frac{50 \text{ kg/m}^2 \times 2873 \text{ m}^2}{120 \text{ min} \times 60 \text{ s/min}} = 20 \text{ kg/s} .$$

The average burning rate is scaled according to  $\dot{m} \sim s^{5/2}$ . Therefore the burning rate of the fuel in the 1/20-scale model is approximately  $11.2 \text{ g/s}$  and the burning time ( $t \sim s^{1/2}$ ) is approx  $26.8 \text{ minutes}$ . Wood cribs made of pine with a density of  $530 \text{ kg/m}^3$  are used as the fuel in the model. The total mass of the fuel is  $11.2 \text{ g/s} \times 26.8 \text{ min} \times 60 \text{ s/min} = 18 \text{ kg}$ . Wood sticks with square cross-sections are used. In all, 638 wood sticks with  $19 \text{ mm} \times 19 \text{ mm}$  cross section are used to build 40 wood cribs as shown in Figure 6.2.

Jet fuel is essentially kerosene, and the total fuel in the American Airline Flight #11 was about  $30,000 \text{ kg}$  [79] when the aircraft impacted the WTC1. About  $9400 \text{ kg}$  jet fuel was burned outside of the tower [101]. An estimation of  $20,000 \text{ kg}$  jet fuel was burned in the building. Here, we estimated that  $10,000 \text{ kg}$  jet fuel was spread on the 96<sup>th</sup> floor and distributed over 10% of the floor area, and the burning rate per unit area  $39 \text{ g/m}^2 \text{ s}$  was used for the jet fuel. So the burning rate of the jet fuel is estimated to be  $39 \text{ g/m}^2 \text{ s} \times 10\% \times 2873 \text{ m}^2 \times 1 \text{ kg} / 1000 \text{ g} = 11 \text{ kg/s}$ , and the total burning time of the jet fuel can be estimated to be  $10000 \text{ kg} / 11.2 \text{ kg/s} = 892 \text{ s}$ .

Therefore, the burning rate for the fuel in the 1/20-scale model is

$$11 \text{ kg/s} \times (1/20)^{5/2} \times 1000 \text{ g/kg} = 6 \text{ g/s},$$

and the burning time is  $892 \text{ s} \times (1/20)^{1/2} = 200 \text{ s}$ . Five round pans with  $0.2 \text{ m}$  diameter were distributed in the north floor, and  $322 \text{ ml}$  mixture of kerosene and heptanes was used to ignite in order to achieve the required burning rate and burning time. Heptanes was used to ensure rapid ignition.



Figure 6.2 Wood cribs used as the fuel in the model

### 6.1.2 Wall and floor materials

Equation 2.16 and 2.17 show that both the heat release from fuels and the heat loss through enclosure boundaries are important in order to obtain similar hot gas temperature profiles in a scaled model. By preserving  $\Pi_{w,k}$  and  $\Pi_{w,\delta}$ , the wall and floor material properties can be chosen and the corresponding thickness can be determined. Therefore, the heat loss rate through the floors and walls are scaled according to  $\dot{q} \sim s^{5/2}$ . Table 6.1 shows the materials used in the WTC and corresponding materials used in the scaled model.

Table 6.1 Wall and floor materials in WTC and scaled model

	Wall material		Floor material	
	<u>WTC</u>	<u>Model</u>	<u>WTC</u>	<u>Model</u>
	Gypsum board	Duroboard	Concrete	FiberFrax
Thermal conductivity @ 200 °C (W/mK)	0.5	0.06 <sup>a</sup>	0.42	0.05 <sup>a</sup>
Density (kg/m <sup>3</sup> )	2700	336 <sup>b</sup>	1750	128 <sup>b</sup>
Specific heat (kJ/kgK)	0.84	1.1 <sup>c</sup>	0.96	1.1 <sup>c</sup>
Thickness (m)	0.0158	0.0064 <sup>d</sup>	0.102	0.051 <sup>d</sup>

<sup>a</sup> Thermal conductivity is scaled according to  $k_w \sim s^{3/4}$ .

<sup>b</sup> Density is scaled according to  $\rho_w \sim s^{3/4}$ .

<sup>c</sup> Specific heat usually doesn't change much for insulation material, so  $c_w \sim s^0$ .

<sup>d</sup> Thickness is scaled according to  $\delta_w \sim s^{1/4}$ .

### 6.1.3 Insulation on steel

Passive fire protection materials were applied to the structural members of WTC towers. NIST conducted an investigation on the insulating materials used in WTC's structural members based on the review of archived documents, photographs, and videos. The results were reported in the NIST final report [79]. The insulation thickness applied in the floor trusses of the tower varied from 0 to 63.5 mm (2.5 inches) at different floor levels. In this paper, both 25.4 mm (1 inch) and 50.8 mm (2 inches) CAFCO DC/F are chosen as the thicknesses of the truss insulation in the prototypes. Vermiculite plaster was used to protect the interior faces of the exterior

columns, and 22.2 mm (0.875 inch) is used as the insulation thickness in the prototype.

Scaling of insulation material of the experimental model is developed from the heat transfer governing equation. The scaling rules for insulation are discussed in chapter 3. Let us recall the scaling of insulation here. Two dimensionless terms can be derived from the governing equations:

$$\Pi_{insulation} = \left( \frac{k_i}{\delta_i} \right) \left( \frac{s^{1/2} A_S}{m_i c_i} \right) \sim \left( \frac{k_i}{\delta_i} \right) \left( \frac{s^{5/2}}{\delta_i C L \rho_i c_i} \right) \sim \frac{k_i}{\delta_i^2 \rho_i} s^{1/2} \quad (6.1)$$

$$\Pi_{steel} = \left( \frac{k_i}{\delta_i} \right) \left( \frac{s^{1/2} A_S}{m_s c_s} \right) \sim \left( \frac{k_i}{\delta_i} \right) \left( \frac{1}{s^{1/2}} \right) \quad (6.2)$$

In Equation 6.1 and 6.2,  $A_S \sim s^2$ ,  $L \sim C \sim s$ , and  $m_s \sim s^3$  are applied as geometry is preserved. By preserving  $\Pi_{insulation}$  and  $\Pi_{steel}$ , the insulating material can be selected and the thickness of insulation can be determined. One solution is to use insulation with the following properties,  $k_i \sim \rho_i \sim s^{3/4}$ , and thickness,  $\delta_i \sim s^{1/4}$ . If the scale factor  $s$  is very small, for example,  $s = 1/20$  as used in the WTC model used herein, the thermal conductivity and the density required in the scaled model can be so small that insulation with such properties may not be available.  $m_s$  may become relatively small if the scale factor,  $s$ , is very small since  $m_s \sim s^3$ . In this case,  $m_s c_s$  may be relatively small comparing to  $m_i c_i$ . That means the heat stored in the steel will be relatively insignificant comparing to the heat stored in the insulation. Under this circumstance, we can preserve  $\Pi_{insulation}$  of the model and allow  $\Pi_{steel}$  to vary as it is not possible to keep both  $\Pi_{insulation}$  and  $\Pi_{steel}$  constant.

FiberFrax blanket [89] is used as the insulation for the scaled model. Its thermal conductivity is  $0.15W / mK$  at  $600^{\circ}C$ . So the thickness of the insulation in the 1/20-scale model can be obtained by preserving  $\Pi_{insulation}$  as shown in Equation

$$6.1: \sqrt{\frac{(50.8mm)^2 \times 251kg / m^3}{0.21W / mK} \times (1/20)^{1/2} \times \frac{0.15W / mK}{96kg / m^3}} = 32.8mm . \text{ Hence, } 32.8$$

$mm$  corresponds to the insulation thickness in the prototype of  $50.8 mm$  ( $2 inches$ ).

The total height of the 1/20-scale floor truss model is only  $38.1 mm$  ( $1.5 inches$ ). The size of the truss model made it not feasible to wrap each floor truss member with insulation which is  $32.8 mm$  thick. Alternatively the entire truss model may be wrapped with the insulation, using an adjusted thickness to keep the effect of conduction similar. Figure 6.3 shows the schema of the insulation thickness adjustment.

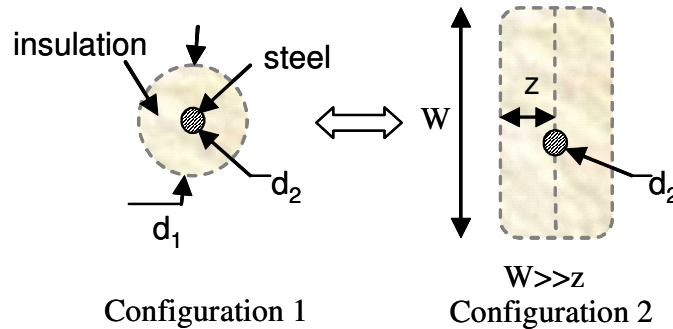


Figure 6.3 Schema of insulation thickness adjustment

In the configuration #1, the thickness of the insulation is determined by preserving  $\Pi_{insulation}$  and using the material properties of FiberFrax Blanket. In order to keep the effect of heat conduction similar between the configuration #1 and configuration #2, a shape factor  $S$  [103] is adopted here. Then

$$\left(\frac{S}{L}\right)_1 = \frac{2\pi}{\cosh^{-1}\left(\frac{d_1^2 + d_2^2}{2d_1d_2}\right)}; \left(\frac{S}{L}\right)_2 = \frac{2\pi}{\ln\left(\frac{8z}{\pi d_2}\right)}. \text{ Equating } \left(\frac{S}{L}\right)_1 \text{ and } \left(\frac{S}{L}\right)_2 \text{ results the}$$

equivalent thickness  $z$ :

$$z = \frac{\pi d_2}{8} e^{\cosh^{-1}\left(\frac{d_1^2 + d_2^2}{2d_1d_2}\right)} \quad (6.3)$$

A summary of the strategies used in this paper to determine the insulation thickness in the scaled model is as follows. First, an available insulating material with a relatively low thermal conductivity is chosen. Second, the required insulation thickness in Configuration #1 is determined by preserving  $\Pi_{insulation}$  and substituting the material properties into  $\Pi_{insulation}$ . Finally, the practical thickness  $z$  to be used in the scaled model is calculated by using Equation 6.3. Table 6.2 shows the insulation properties and thickness used in the 1/20-scale model.

Table 6.2 Insulation materials and thickness used in WTC and scaled model

	Floor trusses	
	<u>WTC</u>	<u>Model</u>
Insulation material	CAFCO DC/F	FiberFrax Configuration #2
Thermal conductivity @ 600 °C(W/mK)	0.21	0.15
Density (kg/m <sup>3</sup> )	251	96
Thickness (m)	0.0254	0.0127
Thickness (m)	0.0508	0.0254
	Exterior columns	
	<u>WTC</u>	<u>Model</u>
Insulation material	Vermiculite plaster	FiberFrax
Thermal conductivity @ 400 °C(W/mK)	0.14	0.09
Density (kg/m <sup>3</sup> )	311	96
Thickness (m)	0.0222	0.0152

## 6.2 Test of 1/20-scale model

Floor trusses including two long-span trusses and one short-span truss and exterior column panel system are built according to geometric scaling as shown in Figure 6.4. The structural members are insulated and placed in the model as shown in Figure 6.5. K-type thermocouples are used to measure the upper layer hot gas temperature. Three heat flux gauges are used to measure the heat flux at the south-west, north-west and south-east corners. All structural models are put in the south-west corner of the floor model. Figure 6.6 shows the schematic representation of

locations of structures and temperature measurement. Two long-span trusses are placed in the south-west corner with one end standing on the north wall. One short-span truss is placed in the south-west corner with one end resting on the west wall. Exterior columns are connected to the trusses and placed in the south and west walls. Temperature of the trusses and the columns are measured. The fire is started by igniting the five pans of liquid fuel (mix of kerosene and heptanes) simultaneously. The fire spreads through the floor by burning the wood cribs. The burning of the scaled model is shown in Figure 6.7. The ventilation change during the fire due to the breakage of windows is simulated by removing part of the walls at East, South and West at 20, 40 and 60 *minutes*, respectively. This change of ventilation is based on the visual evidence reported in the NIST report [79].

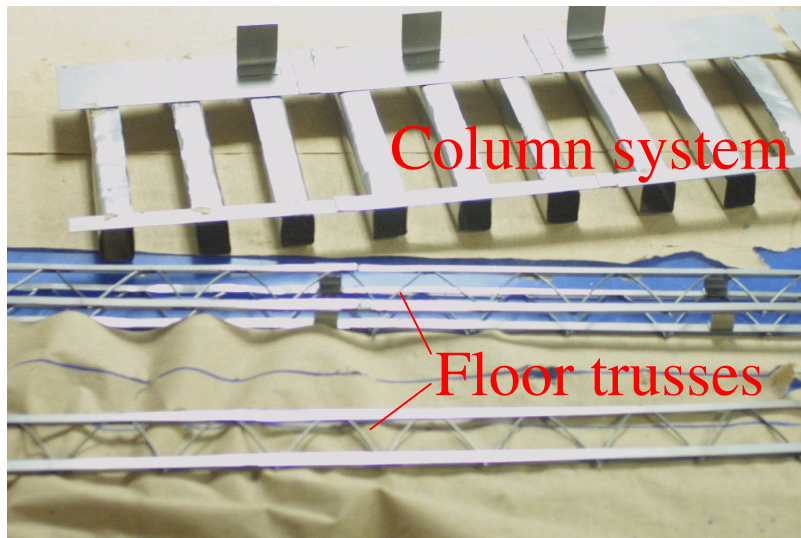


Figure 6.4 Scaled truss and column models

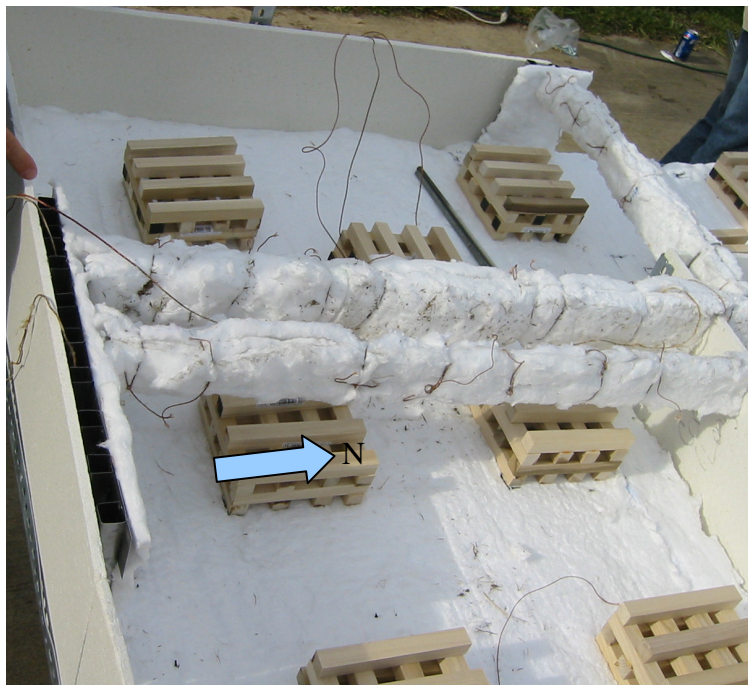


Figure 6.5 Insulated structural models

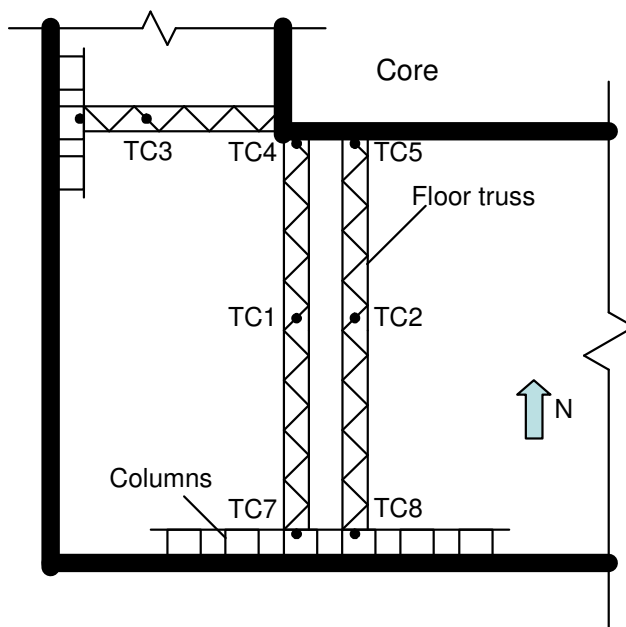


Figure 6.6 Layout of locations of structures and temperature measurement



Figure 6.7 Burning of the 1/20-scale model

### 6.3 Results and analysis

Figure 6.8 shows the temperature profiles of upper layer hot gas from the scaled model plotted in the prototype time scale. Time zero is the time of the aircraft impact. The fire at the North-East and South-East areas begins to extinguish at about *65 minutes*, however the fire at the South-West area continues to about *110 minutes*. The total burning time of the fuels in the scaled model is about *25 minutes* which is close to the predicted time of *26.8 minutes*. The average peak fire temperature measured is  $900\text{ }^{\circ}\text{C}$  which agrees with the estimation in Quintiere [101]. The heat flux measurement shown in Figure 6.9 indicates that the heat flux at the South-West area reaches peak value at about *110 minutes* while the heat flux at other areas reaches peak value at approximately *65 minutes*. As described in NIST report [79] based on

the visual evidences, at about 60 *minutes*, very little fire was visible on the north face where intensive flames were visible from 17 *minutes* to 45 *minutes*, and an intensive fire grew on the 98<sup>th</sup> floor near the west face was started at about 70 *minutes* [79].

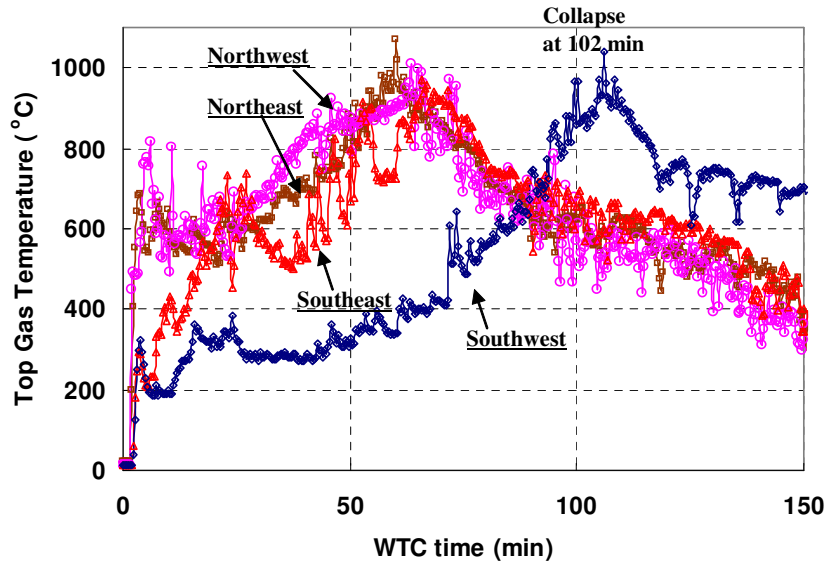


Figure 6.8 Upper layer hot gas temperature profiles plotted in WTC time

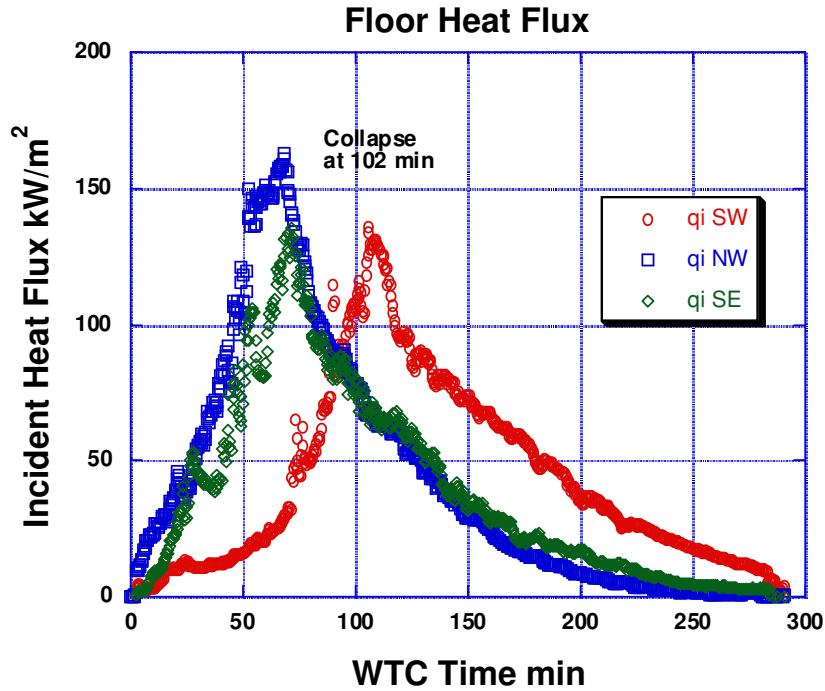


Figure 6.9 Floor heat flux measurement

LT1 denotes the long-span truss with 12.7 mm thick insulation, and LT2 denotes the long-span truss with 25.4 mm thick insulation. ST denotes the short-span truss with 12.7 mm thick insulation. SC1 and SC2 denote the exterior columns in the south wall connected to LT1 and LT2, respectively, and WC denotes the exterior column in the west wall connected to ST. The steel temperature profiles of the two long-span trusses and exterior columns in the south wall are plotted in the prototype time scale and shown in Figure 6.10. The maximum steel temperature of the trusses in the scaled model exceeds 900 °C and the maximum steel temperature of the exterior columns is approximately 600 °C. At the time of 102 minutes, which corresponds to the WTC1 collapse, the trusses in the scaled model reached 800 °C and the columns reach 350 °C. Figure 6.11 shows the temperature profiles of the short-span truss and exterior column in the west wall. The short-span truss reaches its maximum

temperature ( $800^{\circ}\text{C}$ ) at about 110 *minutes*, and the column temperature exceeds  $500^{\circ}\text{C}$  at about 68 *minutes*. The result in Figure 6.10 also shows that the time that steel temperature in the LT2 reached the maximum value is delayed by 10 *minutes* comparing to the time of maximum temperature of LT1. However, the maximum steel temperature in both trusses approximates the same.

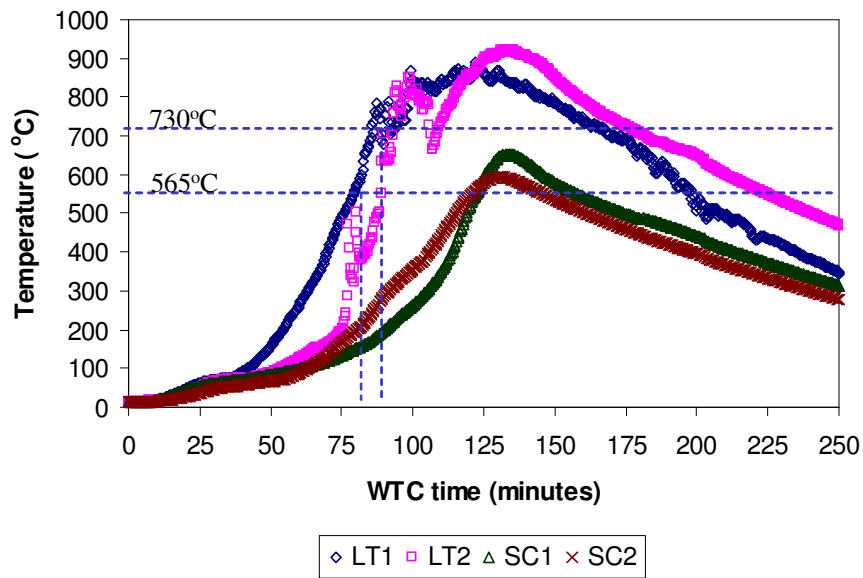


Figure 6.10 Steel temperature profiles of long-span trusses (LT) and exterior columns (SC)

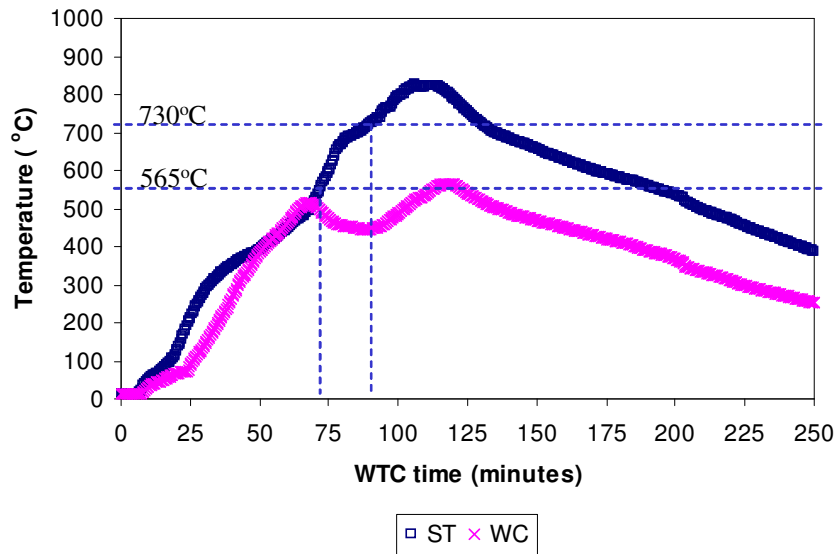


Figure 6.11 Steel temperature profiles of short span truss and exterior column

The NIST report on WTC [79] showed a comprehensive structural analysis to investigate the structural performance of components, connections and subsystems subjected to high temperature. The NIST report shows that the diagonal webs in the floor trusses buckled when the steel temperature reaches  $565^{\circ}\text{C}$ . The scale experimental result in Figure 6.10 shows that the truss reached  $565^{\circ}\text{C}$  at around 80 to 90 minutes (prototype time). This result indicates that the floor trusses would begin sagging significantly at 80 to 90 minutes. Visual record shows that “the inward bowing of the south exterior wall was first observed at 10:23am [79]” which is 96 minutes from the airplane impact. Hence, the scale experiment results match the WTC observation. Numerical study performed at NIST indicates that the floor trusses would begin falling off the truss seats when the truss temperature reached  $730^{\circ}\text{C}$  and

“instability of an exterior wall subsystem could occur when at least three floors are disconnected [79]”. The scale experiment result in Figure 6.10 shows that the truss reached  $730^{\circ}\text{C}$  at around 85 to 95 *minutes* (prototype time). That indicates that the long-span trusses at southwest corner would begin falling off at 85 to 95 *minutes*, and furthermore, the instability of the exterior columns could occur at around 95 *minutes*. This result matches the collapse time of World Trade Center tower 1 of 102 *minutes*.

#### 6.4 Conclusion and discussion

The fire and structures on the 96<sup>th</sup> floor of World Trade Center tower 1 were re-constructed in a 1/20 scale. The choice of floor and wall materials and insulating material on structural system were based on the scaling rules to produce similarity between the scaled model and prototype. The testing of the scaled model shows a vivid example of using a scaled model to simulate a real-world disaster, and the results obtained help us to understand the failure mechanism involved in the disaster.

The testing of the scaled model provides the hot gas temperature profile and the heat flux measurements at different locations. The total burning time of the fuels in the scaled model is about 25 *minutes* which corresponds to the 120 *minutes* burning of the WTC1. Based on the structural analysis of WTC structural system at elevated temperature conducted by NIST, the experimental results in the scaled model provide a timeline of structural response of WTC1 during the disaster. The results are summarized as following:

1. Fire was spread from the north to the south. The hot gas temperature reached the peak at 65 *minutes* in the north area and 110 *minutes* in the south area.

2. The peak hot gas temperature in the model reached 1000 °C.
3. The peak temperature of trusses reached 900 °C and the peak temperature of exterior columns is about 600 °C.
4. The time to reach the maximum steel temperature in the truss with 25.4 mm thick insulation is delayed about 10 *minutes* comparing to the truss with 12.7 mm insulation. However, the peak steel temperature in both trusses is similar.
5. The scale experiment result reproduced a timeline of the prototype. Along with the numerical simulation results conducted by NIST [79], the scale experiment results indicate that the long-span floor trusses at southwest corner would begin sagging significantly at 80 to 90 *minutes* (prototype time). This corresponds to the visual record which shows that the inward bowing of the south exterior wall was first observed at 96 *minutes* from the airplane impact. The scale experiment result indicates that the long-span floor trusses at southwest corner would begin falling off the truss seats at around 85 to 95 *minutes* and the instability of the exterior columns could therefore occur at around 95 *minutes*. This matches the fact that WTC1 collapsed at 102 *minutes*.
6. A better understanding of the fire spreading and fire temperature profiles at different locations of the 96<sup>th</sup> floor has been built based on the scale experiment results.
7. The results show that the testing of scale model can replicate the prototype behavior in a satisfactory manner.

## Chapter 7: Modeling of restrained steel beam in fire with consideration of local yielding

The behavior of a structure exposed to fire is relatively complex since the temperature and boundary restraint play important roles for the stress distribution and magnitude in the structure. Steel weakens as the temperature increases, and the properties of construction steel at elevated temperature have been well studied. Additional stress is produced when the thermal expansion of the structure is constrained because of the boundary restraint provided by the adjacent elements. The stress in the structure is therefore increased, and at the same time, the yielding strength of the material decreases as temperature rises. This combination of loading and material degradation results in local yielding that differs from the typical yield zone created by bending moment at room temperature.

Usmani *et al* [36] presented a useful means of estimating forces and deflections in idealized structures. Moss *et al* [93] provided a detailed analytical investigation into support conditions of steel and composite beams at elevated temperature, and their results show that the beam behavior in fire is highly dependent on support conditions. Steel beams with boundary restraint in fire has been studied numerically [11, 53, 104, 105] and experimentally [44]. Simplified hand calculation method has also been proposed [62, 63]. However, very little work has been conducted on modeling the effect of local yielding developed in a steel beam with boundary restraints.

Finite element plastic zone method has the capability to simulate the gradual spreading of plasticity in elements. Generally a 3-D geometric models with small elements are needed. This type of analysis requires large computational efforts, and it is not always practical in engineering practice to perform such an analysis on individual members. Al-Mashary and Chen [106] proposed a practical method for steel frame design in which the gradual bending stiffness degradation was simulated by decreasing the stiffness of two pseudo rotational springs at the ends of a beam. Furthermore, Chen and Chan [107] developed an efficient method for inelastic large-deflection analysis of steel frames by using elements with both member-end and mid-span rotational springs so that a beam can be modeled as a single element. The model with pseudo springs can significantly reduce the complexity of computation while obtaining reasonable accuracy [106, 107]. However, no discussion on modeling fire-induced local yielding by using pseudo springs in a beam model has been done. Moreover, the relationship between the development of local yielding and beam temperature needs to be determined with consideration of changing boundary constraints.

In this chapter, a simplified calculation method is proposed in order to estimate the boundary conditions of a beam in a frame structure. Simulation of a steel beam at elevated temperature with different boundary conditions is conducted using finite element software to investigate the effect of the boundary restraint on the beam deflection and development of local yielding in the beam. Simplified method is proposed to determine the temperatures at which the end sections and the mid-span section start to yield, and a beam model with pseudo springs is used to simulate the

effect of local yielding in the beam under high temperature environment. The results from the proposed simplified method are compared to the results obtained using the finite element plastic zones method. This proposed simplified method is a simpler alternative to a 3-D finite element analysis to evaluate the structural performance of a beam exposed to a fire.

### 7.1 Development of local yielding and deflection

This research starts with the analysis of an I-shape steel beam exposed to fire. The stress on a beam in a structure subjected to fire is a combination of mechanical stress ( $\sigma_m$ ) that is induced by gravity load, and thermal stress ( $\sigma_t$ ) that is induced by the boundary restraint and temperature change that provides resistance to thermal expansion; *i.e.*  $\sigma_{tot} = \sigma_m + \sigma_t$ . The thermal induced stress ( $\sigma_t$ ) is directly related to the boundary restraint of a beam. When rigid lateral restraints are present, thermal-induced force in the beam can be dominant. If a beam is also slender, buckling may occur early when structural temperature is not significantly high [36]. Therefore boundary restraint plays an important role for the stress development in the beam that is subjected to high temperature, and a rational analytical technique is needed to model it.

In order to investigate the development of local yielding and deflection in a restrained steel I-shape beam at elevated temperature, a non-linear finite element simulation is conducted using ANSYS [14], as shown in Figure 7.1. W8×48 steel beam is considered, and the length of the beam is 5 m. The elastic modulus of steel at

room temperature is  $200 \text{ GPa}$ . The elastic-plastic relation of steel is idealized as shown in Figure 7.2. 5% tangent modulus is assumed in the simulation. SHELL181 [14] is chosen as the element as it admits plasticity and large strain. Axial springs are represented by COMBIN14 [14]. Coupled degrees of freedom [14] are applied in the end sections to ensure the same displacement in axial direction so that the two springs at each end have the same displacement and forces. Uniform transverse loading of  $30 \text{ kN/m}$  is applied to the beam. The beam is braced in the lateral direction of the beam so that the lateral torsional buckling is prevented. The degradation ratios for Young's modulus and yield strength of the steel are obtained from ASTM E119 standard [13]. The behaviors of the beam under five different axial restraints ( $0$ ,  $0.02EA/L$ ,  $0.2EA/L$ ,  $2EA/L$ , and infinite) are investigated.

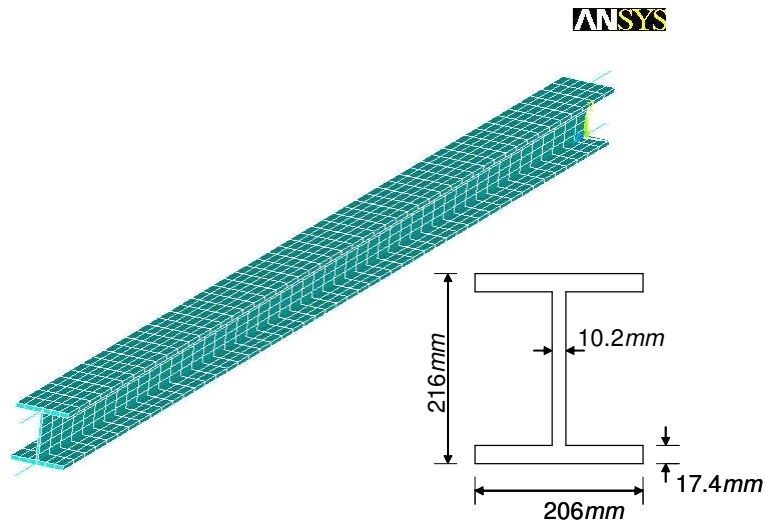


Figure 7.1 3D restrained beam model and section dimension

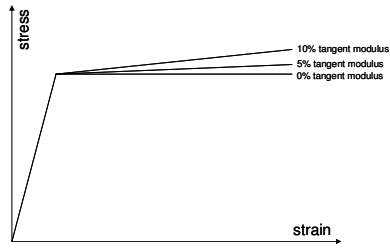


Figure 7.2 Elastic-plastic model of steel

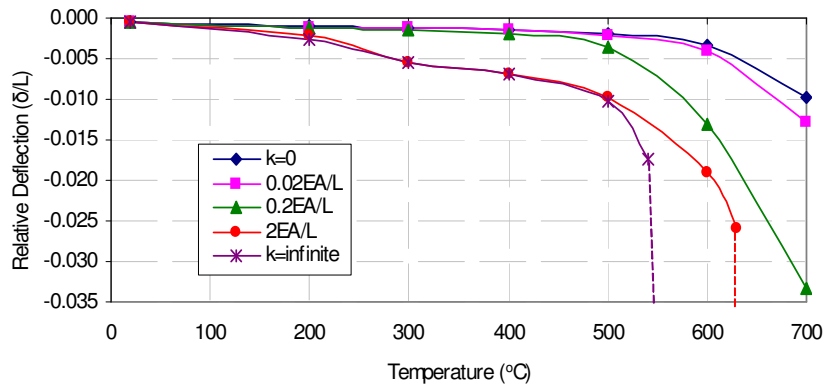


Figure 7.3 Beam deflection with different axial restraints

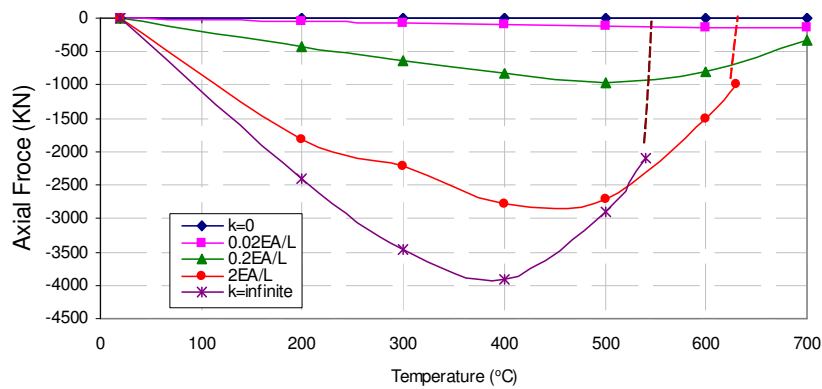


Figure 7.4 Axial forces in the beam with different axial restraints

The effect of axial restraints on the deflection is shown in Figure 7.3, in which the mid-span deflection of the beam in the transverse direction is plotted as a function

of steel temperature. The results show that the restraint conditions at the ends of the beam play an important role on the deflection. For fully restrained beam, the deflection starts to increase rapidly at a relatively low temperature ( $300\text{ }^{\circ}\text{C}$ ). However, for the beam with smaller axial resistance, the beam does not deform significantly until the steel reaches a relatively high temperature of  $600\text{ }^{\circ}\text{C}$ . In Figure 7.3, the dashed lines indicate that the FE model of the beam failed at this temperature. Figure 7.4 shows the axial forces of the beam. As the beam deforms more, the beam shortening due to the transverse deformation becomes more important. That is why the compression in the beam reduces as the beam deformation increases. The tension force developed due to the beam shortening can become greater than the compressive force due to the thermal expansion. When this occurs, the beam behaves like a catenary.

An element carries no more force when its stress exceeds the yielding strength. The development of the yielding zones in a restrained beam is investigated by examining its axial stress distribution at elevated temperature, as shown in Figure 7.5. The beam with axial boundary restraints of  $0.2EA/L$  is used as an example here. Figure 7.5 shows that the stress pattern is not changed significantly at temperature below  $500\text{ }^{\circ}\text{C}$ . As temperature increases, the yielding zones at ends and at mid-span sections are developed gradually. At  $600\text{ }^{\circ}\text{C}$ , the end sections are partially yielded. When temperature goes up to  $700\text{ }^{\circ}\text{C}$ , an expanded yield zone appears in the upper part of the middle span of the beam. The yield zones developed at high temperature are different from the plastic hinges typically results from bending moment at room temperature. As shown in Figure 7.5, the yield zones at both the ends and mid-span

do not extend through the depth of the beam section. The beam with partially yielded zones at high temperature should be similar to a beam with reduced sections at those locations. The sections with yield zones permit more rotation and deformation than regular sections so that the transverse deflection of the beam increases significantly. Therefore, the effect of the local yielding has to be considered when the behavior a restrained beam at high temperature is to be studied.

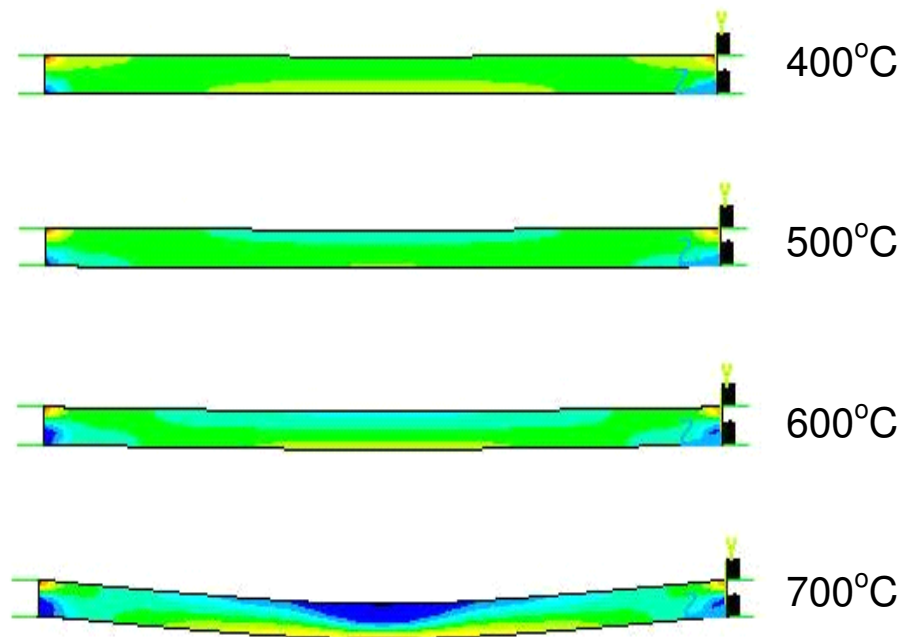


Figure 7.5 Axial stress distribution patterns in the beam at elevated temperature

## 7.2 Estimation of axial boundary restraint

Since most structural members are connected to other load-bearing structures, the boundary restraint on a member depends on the stiffness of the adjacent members. For a frame structure, the axial restraint can be calculated by removing the beam from the structure, and applying a unit forces to the remaining structure. The axial restraint

on the beam can be represented as one translational spring at each end with stiffness  $k_{1L}$  and  $k_{1R}$ . The assumption here is that the beam expands axially when it is subject to fire. The values of  $k_{1L}$  and  $k_{1R}$  can be determined by  $k_{1L} = 1/\Delta_L$  and  $k_{1R} = 1/\Delta_R$ , respectively.  $\Delta_L$  and  $\Delta_R$  are the deflection induced by unit forces in the beam at its axial direction. For a beam with elevated temperature in a frame, the unit loads should be applied to in pair because the thermal expansion of the beam induces forces at both ends of the beam.

Applying the unit force method to each member of a structure is not practical for engineering practices for large frame structures. For such structures, a simplified method would be more efficient to obtain an approximate stiffness value. Huang and Tan [54] developed a method to calculate the stiffness of columns in a frame structure. This research modifies this method by including bracing members. It can be used to estimate the boundary stiffness of a steel beam in a frame structure.

Steel frames with different bracing design are shown in Figure 7.6. W8×48 steel members are used for both beams and columns in the frame models. The length of all beams is 5 m, and the height of all columns is 4 m. The cross sectional area of bracing members is  $1.96 \times 10^3 \text{ mm}^2$ . The elastic modulus of steel is 200 GPa. Sidesway is inhibited in the plane of the frame. The beam (highlighted) in the second floor is considered. The boundary restraint is represented as translational springs at both ends of the beam, which provide resistance to the thermal expansion when the beam is subject to a fire. Figure 7.7 shows that column AC, column CB and brace CD are subjected to a horizontal force  $P$  at point C due to the thermal expansion of the

beam.  $\Delta$  is the horizontal deflection at point C. The axial force in the brace  $F_{br}$  can be related to  $\Delta$ , hence

$$\Delta = \frac{F_{br} L_{br}}{EA_{br} \cos \theta} \quad (7.1)$$

where  $\cos \theta = L_b / L_{br}$ .  $L_b$  is the length of the beam, and  $L_{br}$  is the length of the bracing member.  $A_{br}$  is the sectional area of the bracing member. Considering the column AB under a horizontal force, its horizontal deflection can be written as:

$$\Delta = \frac{(P - F_{br} \cos \theta) L_c^3}{24EI_c} \quad (7.2)$$

where  $L_c$  is the height of the columns, and  $P$  is the horizontal force due to thermal expansion of the beam.  $I_c$  is the moment of inertia of the columns. From Equation 7.1 and 7.2, the axial force in the brace CD can be obtained:

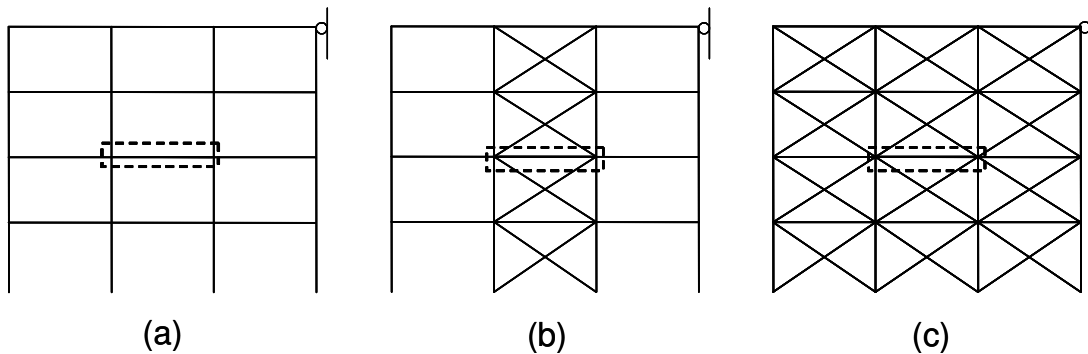


Figure 7.6 Restrained steel beam in frames

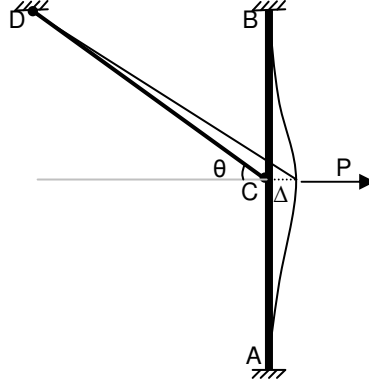


Figure 7.7 Columns and brace subjected to a horizontal force

$$F_{br} = \frac{PL_c^3}{24EI_c} \left( \frac{I}{\frac{L_{br}}{EA_{br} \cos \theta} + \frac{L_c^3 \cos \theta}{24EI_c}} \right) \quad (7.3)$$

Substitute Equation 7.3 into Equation 7.2,  $\Delta$  can be written in terms of  $P$  :

$$\Delta = \frac{PL_c^3}{24EI_c} \left( 1 - \frac{L_c^3}{24EI_c} \left( \frac{I}{\frac{L_{br}}{EA_{br} \cos^2 \theta} + \frac{L_c^3}{24EI_c}} \right) \right) \quad (7.4)$$

Therefore, the stiffness of the axial restraint of the beam at point C can be written as:

$$k_c = \frac{P}{\Delta} = \left( \frac{24EI_c}{L_c^3} \right) / \left( 1 - \frac{L_c^3}{24EI_c} \left( \frac{I}{\frac{L_{br}}{EA_{br} \cos^2 \theta} + \frac{L_c^3}{24EI_c}} \right) \right) \quad (7.5)$$

Consider a beam in a frame such as those shown in Figure 7.6 exposed to a fire. Assume that the fire is local, and it affects one beam in the frame only, we may assume that all columns and bracing members of the floors above and below the beam contribute to the restraints of the beam; *i.e.*, the far ends of the columns are assumed

to be fixed. The axial restraint of the beam in a frame can be obtained by generalizing Equation 7.5:

$$k_c = \left( \frac{24EI_c n_c}{L_c^3} \right) / \left( 1 - \frac{L_c^3}{24EI_c n_c} \left( \frac{I}{\frac{L_{br}}{EA_{br} n_{br} \cos^2 \theta} + \frac{L_c^3}{24EI_c n_c}} \right) \right) \quad (7.6)$$

$n_c$  is the number of pairs of columns which provide restraints to the beam at one end.

$n_{br}$  is the number of bracing members needed to be included. For example,  $n_c = 2$ ,

$n_{br} = 0$  for Figure 7.6(a).  $n_c = 2$ ,  $n_{br} = 2$  for Figure 7.6(b);  $n_c = 2$ ,  $n_{br} = 6$  for

Figure 7.6(c). Table 7.1 lists the values of the axial restraints of the beams in Figure

7.6, and the results are compared to those obtained by the unit-load method.

Table 7.1 Estimation of axial restraints of steel beams in Figure 7.6

Frames in Figure 6	Estimation of the axial restraint, $k$		
	Approx. method	Unit-load method	Relative difference
(a)	$1.1 \times 10^7 N/m$	$0.9 \times 10^7 N/m$	22 %
(b)	$0.9 \times 10^8 N/m$	$1.1 \times 10^8 N/m$	18 %
(c)	$2.4 \times 10^8 N/m$	$2.3 \times 10^8 N/m$	4 %

The approximate method provides an easy way to estimate the axial boundary restraint of a typical beam in a frame structure. The approximated estimation is acceptable when it compares to the values obtained from the unit-load method. As shown in Table 7.1 the error is less than 22% compared to the more rigorous unit-load method.

### 7.3 Simplified beam model with pseudo rotational springs

#### 7.3.1 Beam behavior at small transverse deflection

Figure 7.8 shows a beam with partial axial restraint and full rotational restraint. The beam is subjected to a uniformly distributed loading,  $w$ . The assumptions used in this analysis are plane sections remain plane; springs deform linearly; lateral torsional buckling of the beam is restrained; local buckling of flanges is also prevented. The deflection of the beam is assumed to be small at beginning stage of heating, so the beam shortening due to transverse deflection can be neglected. However, the beam shortening cannot be neglected when the transverse deflection becomes significant.

As the temperature of a beam increases, the beam expands axially. The equilibrium equations for axial force and axial deformation can be written as:

$$P = k_{1L}\Delta_L = k_{1R}\Delta_R \quad (7.7)$$

$$\alpha L(T - T_\infty) = \Delta_L + \Delta_R + \frac{P}{E_T A} L \quad (7.8)$$

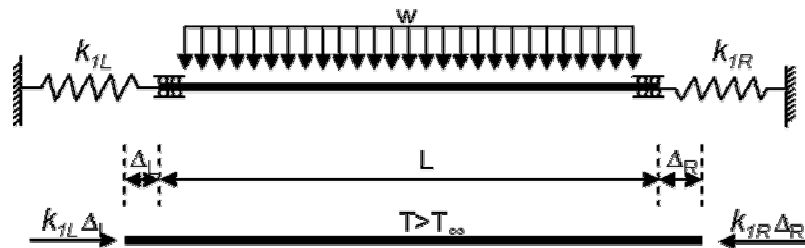


Figure 7.8 Restrained beam model

$$\text{where } E_T = \begin{cases} \left[ 1 + \frac{T}{2000 \ln(T/1000)} \right] E_0 & \text{for } T \leq 600^\circ \text{C} \\ \left[ \frac{690 - 0.69T}{T - 53.5} \right] E_0 & \text{for } T > 600^\circ \text{C} \end{cases} \quad [13]. \quad E_T \text{ is the elastic}$$

modulus of steel at elevated temperature.  $\Delta_L$  and  $\Delta_R$  are positive when the beam expands and the translational springs are in compression.  $\Delta_L$  and  $\Delta_R$  are negative when the beam contracts and the translational springs are in tension. From Equation 7.7 and 7.8, the axial deflection at left and right ends can be obtained:

$$\Delta_L = \frac{\alpha L (T - T_\infty)}{1 + \frac{k_{1L}}{k_{1R}} + \frac{k_{1L} L}{E_T A}} \quad (7.9)$$

$$\Delta_R = \frac{\alpha L (T - T_\infty)}{1 + \frac{k_{1R}}{k_{1L}} + \frac{k_{1R} L}{E_T A}} \quad (7.10)$$

From Equation 7.7 and 7.9, the compressive axial stress due to the thermal expansion can be written as

$$\sigma_t = \frac{P}{A} = \frac{k_{1L} \Delta_L}{A} = \frac{\alpha L (T - T_\infty)}{\left( \frac{L}{E_T A} + \frac{1}{k_{1L}} + \frac{1}{k_{1R}} \right) A} \quad (7.11)$$

The total stress in the beam ( $\sigma_{tot}$ ) consists of two parts: initial mechanical stress,  $\sigma_m$ , and thermal stress,  $\sigma_t$ . Figure 7.9 shows the stress distribution at the end sections of the beam where compression is negative and tension is positive. With temperature increasing, the bottom extreme fiber of the beam sections reaches the yielding strength of steel first. So, the temperature at which end sections of the beam start to yield can be determined from the following equation:

$$\sigma_{tot} = \frac{M_{1,2}h/2}{I} + \frac{\alpha L(T - T_{\infty})}{\left(\frac{L}{E_T A} + \frac{1}{k_{1L}} + \frac{1}{k_{1R}}\right)A} = \sigma_{y,T} \quad (7.12)$$

where  $\sigma_{y,T} = \begin{cases} \left[1 + \frac{T}{900 \ln(T/1700)}\right] \sigma_{y,20^{\circ}C} & \text{for } T \leq 600^{\circ}C \\ \left[\frac{340 - 0.34T}{T - 240}\right] \sigma_{y,20^{\circ}C} & \text{for } T > 600^{\circ}C \end{cases}$  [13].  $\sigma_{y,T}$  is the yield

strength of steel at elevated temperature.  $M_{1,2}$  is the moment at the ends due to external loading.

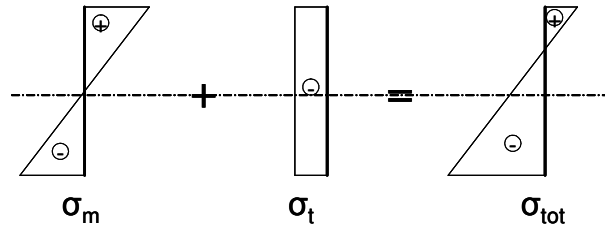


Figure 7.9 Stress distribution on the sections at ends

The temperature at which global elastic buckling occurs can be determined by equating the axial force and the critical loading:

$$\sigma_t A = \frac{\alpha L(T - T_{\infty})}{\frac{L}{E_T A} + \frac{1}{k_{1L}} + \frac{1}{k_{1R}}} = \frac{\pi^2 E_T I}{AL^2} \quad (7.13)$$

Solving Equation 7.13 for  $E_T$ , the critical temperature of elastic buckling can be obtained.

The total stress at the middle section consists of three parts: initial mechanical stress,  $\sigma_m$ , thermal stress,  $\sigma_t$ , and stress due to  $P - \delta$  effect,  $\sigma_{P-\delta}$ , as shown in

Figure 7.10.

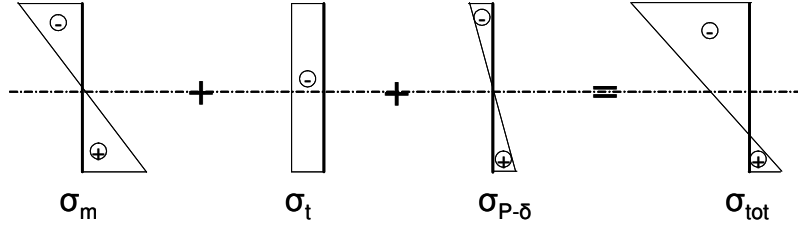


Figure 7.10 Stress distribution on the section at mid-span

For a beam with uniformly distributed loading, as shown in Figure 8, the total moment at the middle section can be written as [94]:

$$M_{tot} = \left( \frac{1 - 0.384P/P_E}{1 - P/P_E} \right) M_0 \quad (7.14)$$

where  $M_0 = wL^2 / 24$  and  $P_E = \frac{\pi^2 E_T I}{L^2}$ .  $M_0$  is the moment at the middle due to external loading.  $P_E$  is the elastic buckling load. The total stress in the middle section is the summation of  $\sigma_t$  and  $M_{tot}c / I$ . As temperature increases, the upper extreme fiber of the middle section reaches the yield strength. Therefore, the temperature at which the middle section starts to yield can be determined by equating the maximum compressive stress to the steel yield strength:

$$\frac{\alpha L (T - T_\infty)}{\left( \frac{L}{E_T A} + \frac{1}{k_{IL}} + \frac{1}{k_{IR}} \right) A} + \left( \frac{1 - 0.384P/P_E}{1 - P/P_E} \right) \frac{M_0 h}{2I} = \sigma_{y,T} \quad (7.15)$$

### 7.3.2 Beam behavior with large transverse deflection

As the stiffness of both end rotational springs and the middle rotational spring decrease, the transverse deflection of the beam can increase significantly. Under such circumstance, the beam shortening due to the transverse deflection generally cannot

be neglected. The equilibrium equations of axial force and axial deformation can now be written as:

$$k_{iL}\Delta_L = k_{iR}\Delta_R \quad (7.16)$$

$$\alpha L(T - T_\infty) = \Delta_L + \Delta_R + \frac{k_{iL}\Delta_L}{E_T A} L + d \quad (7.17)$$

where  $d$  is the beam shortening due to transverse deflection and it is a function of deflection profile,  $y$ . From Equation 7.16 and 7.17, the deformation of the axial springs at left and right ends can be obtained:

$$\Delta_L = \frac{\alpha L(T - T_\infty) - d}{1 + \frac{k_{iL}}{k_{iR}} + \frac{k_{iL}L}{E_T A}} \quad (7.18)$$

$$\Delta_R = \frac{\alpha L(T - T_\infty) - d}{1 + \frac{k_{iR}}{k_{iL}} + \frac{k_{iR}L}{E_T A}} \quad (7.19)$$

and the stress due to thermal effects is

$$\sigma_t = \frac{P}{A} = \frac{k_{iL}\Delta_L}{A} = \frac{\alpha L(T - T_\infty) - d}{\left( \frac{L}{E_T A} + \frac{1}{k_{iL}} + \frac{1}{k_{iR}} \right) A} \quad (7.20)$$

When the beam shortening due to transverse deflection becomes large,  $\Delta_L, \Delta_R$  can become negative. That means the translational springs at both ends are in tension and the axial force in the beam changes from compression to tension. Such catenary action has been observed and discussed by Newman *et al.* [3], Yin and Wang [62, 63], and Moss *et al.* [93].

The beam shortening due to transverse deflection can be written as function of maximum transverse deflection,  $y_{max}$ , and a deflection profile factor,  $\lambda$ .  $\lambda$  is defined in Equation 7.21:

$$d(y_{max}, \lambda) = \int [L + (y'')^2]^{1/2} - L = \lambda \frac{y_{max}^2}{L} \quad (7.21)$$

So the determination of  $d(y)$  requires an assumed beam deflection profile. For a beam with full end rotational restraint, a fourth order polynomial can be used as the transverse deflection profile [63]:

$$y = \frac{16 y_{max}}{L^2} \left( \frac{x^4}{L^2} - \frac{2x^3}{L} + x^2 \right) \quad (7.22)$$

The corresponding deflection profile factor using Equation 7.21 is  $\lambda = 2.44$ .

Let  $\chi$  be defined as the section yielding index [106], which denotes the percentage of yielding along the depth of the beam.  $\chi$  varies between 0 and 1. “ $\chi = 0$ ” indicates the section does not yield, and “ $\chi = 1$ ” indicates the whole section yields. By equating the total stress and the yield strength of steel, the relationship between the yielding index at end sections ( $\chi_{L,R}$ ) and temperature ( $T$ ) can be formed:

$$\frac{\alpha L(T - T_{\infty}) - d}{\left( \frac{L}{E_T A} + \frac{1}{k_{1L}} + \frac{1}{k_{1R}} \right) A} + \frac{M_{1,2}(1/2 - \chi_{L,R})h}{I} = \sigma_{y,T} \quad (7.23)$$

Similarly, the relationship between the yielding index at mid-span section ( $\chi_M$ ) and temperature ( $T$ ) can be determined in the following equation:

$$\frac{\alpha L(T - T_{\infty}) - d}{\left(\frac{L}{E_T A} + \frac{1}{k_{1L}} + \frac{1}{k_{1R}}\right)A} + \frac{\left(\frac{1 - 0.384P/P_E}{1 - P/P_E}\right)M_0(1/2 - \chi_M)h}{I} = \sigma_{y,T} \quad (7.24)$$

By solving Equation 7.23 and 7.24, the yielding index of end and mid-span sections can be determined.

### 7.3.3 Determination of stiffness of rotational springs

A partially yielding zone in a beam can be represented by a hinge and a rotational spring. Three pseudo rotational springs are applied to the ends and the middle of the beam as shown in Figure 7.11. The relationship between the stiffness of the rotational springs and the yielding index from Al-Mashary and Chen [106], and Chen and Chan[107] is adopted here:

$$k_{2L,R} = \frac{E_T I}{L} \left[ \frac{2}{1/(1 - \chi_{L,R}) - 1} \right] \quad (7.25)$$

$$k_{2M} = \frac{E_T I}{L} \left[ \frac{8}{1/(1 - \chi_M) - 1} \right] \quad (7.26)$$

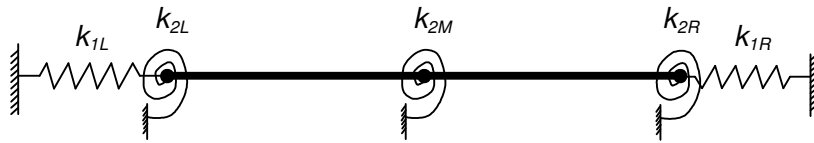


Figure 7.11 Beam model with pseudo springs

At a known temperature, the yielding index at both ends and the middle sections can be determined from Equation 7.23 and 7.24. Using this index, the stiffness of the rotational springs can be obtained from Equation 7.25 and 7.26. Hence a beam in a

frame subjected to a room fire may be represented by the simplified model shown in Figure 7.11.

Figure 7.12 shows the flow chart for using the beam model with pseudo springs to represent the partially yielded zone at elevated temperatures. An iteration process is used until the difference between the initial value ( $\tilde{y}_{max}$ ) and the output value ( $y_{max}$ ) is less than a tolerance, *i.e.*  $|\tilde{y}_{max} - y_{max}| \leq \varphi$ . The following steps can be used to implement this iteration process:

*Step 1.* Assume an initial value of  $\tilde{y}_{max}$  at temperature  $T_i$ .

*Step 2.* Determine the beam shortening due to transverse deflection ( $d(y_{max}, \lambda)$ ) from Equation 7.21. Based on the value of  $d$ , solve Equation 7.23 and 7.24 to obtain the yielding indexes ( $\chi_{L,R}$  and  $\chi_M$ ).

*Step 3.* Calculate the stiffness of the rotational springs from Equation 7.25 and 7.26.

*Step 4.* Analyze the simplified beam model with springs to obtain the deflection and axial force of the beam.

*Step 5.* If the maximum transverse deflection  $y_{max}$  from *Step 4* is close to the initial value of  $\tilde{y}_{max}$ , *i.e.*,  $|\tilde{y}_{max} - y_{max}|$  is less than a tolerance, go back to *Step 1* with

$T_{i+1} = T_i + dT$ . If  $|\tilde{y}_{max} - y_{max}|$  is more than a tolerance, go back to *Step 1* with a new initial value of  $\tilde{y}_{max}$  at temperature  $T_i$ .

For each iteration, the initial value of  $\tilde{y}_{max}$  at temperature  $T_i$  can be assumed to be the value of  $y_{max}(T_{i-1})$  at a previous temperature  $T_{i-1}$ . If the temperature

incremental increment  $dT$  is small,  $y_{max}(T_{i-1})$  can be a good approximation of  $y_{max}(T_i)$ .

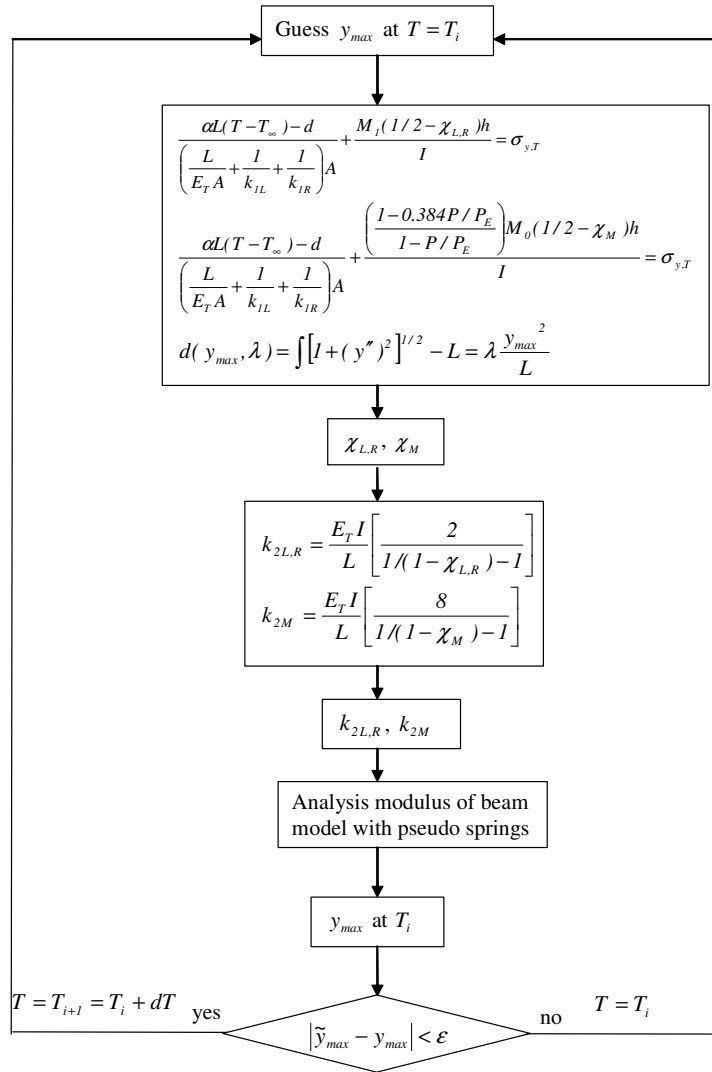


Figure 7.12 Flow chart of analysis of simplified beam model with pseudo springs

#### 7.4 Validation of simplified method

Two validation examples are conducted: one using a 5 m W8×48 beam and the other using an 8 m W8×48 beam. Elastic modulus of the steel is  $2 \times 10^{11} \text{ GP}_a$ . The

elastic modulus of the beam at elevated temperature is obtained from ASTM E119 standard [13]. Both beams are assumed to have an axial boundary restraint of a translational spring with  $k_{IL} = k_{IR} = 0.2EA/L$ . A transverse uniformly distributed load of  $30\text{KN/m}$  is applied to the beams. The beam model with rotational springs as shown in Figure 7.11 is used. The stiffness of the three rotational springs is assigned to be infinite at room temperature. As temperature increases, the stiffness of the rotational springs decreases when a local yielding zone forms in the beam. Figure 7.13 and Figure 7.14 show the mid-span deflection and axial force of the  $5\text{ m}$  beam at elevated temperature obtained from the simplified method from section 7.3 compared to the results of a nonlinear FE analysis. The relative difference of the maximum deflection at  $700^\circ\text{C}$  from the two methods is 9.9%. The FE analysis stopped at  $700^\circ\text{C}$  because the axial force in the beam exceeds the elastic buckling load. The mid-span deflection and axial force of the  $8\text{ m}$  beam are shown in Figure 7.15 and Figure 7.16, respectively. The relative difference of the maximum deflection at  $800^\circ\text{C}$  is 14.8%. Figure 7.16 shows that the axial force in the beam changes from compression to tension at about  $700^\circ\text{C}$ , and the beam behaves as a catenary. The proposed simplified method successfully predicts the catenary action in the beams.

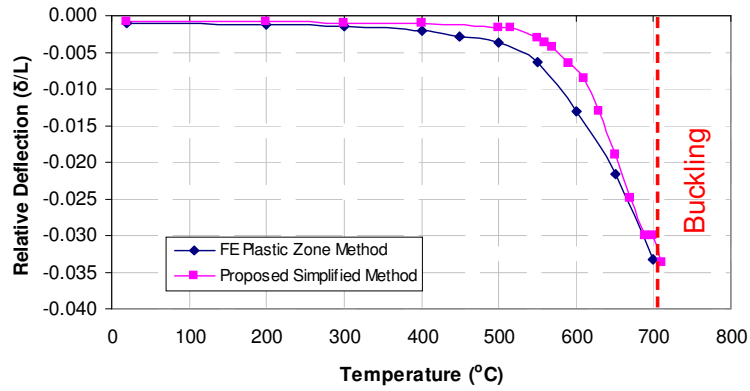


Figure 7.13 Mid-span deflection of 5 m steel beam at elevated temperature

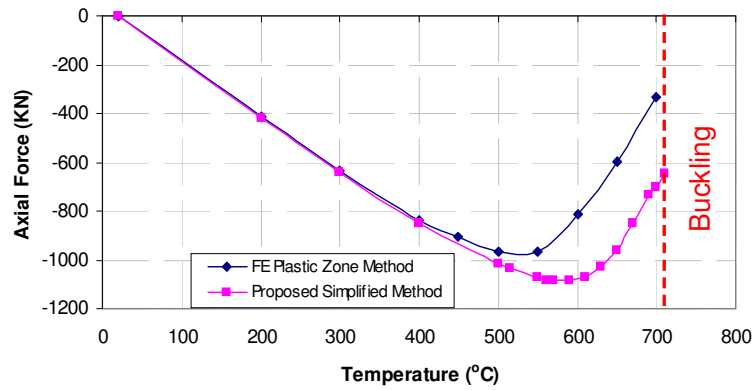


Figure 7.14 Axial force of 5 m steel beam at elevated temperature

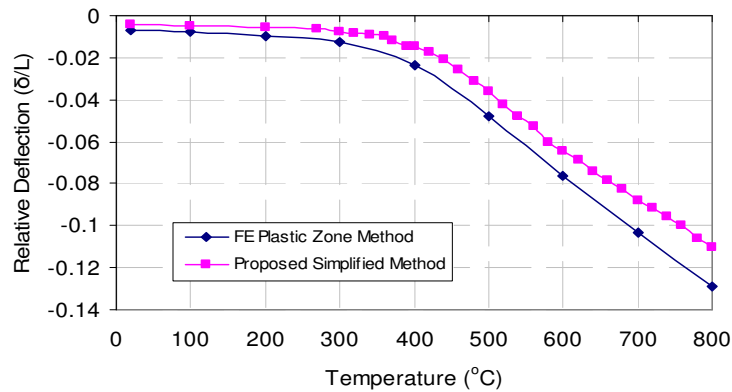


Figure 7.15 Mid-span deflection of 8 m steel beam at elevated temperature

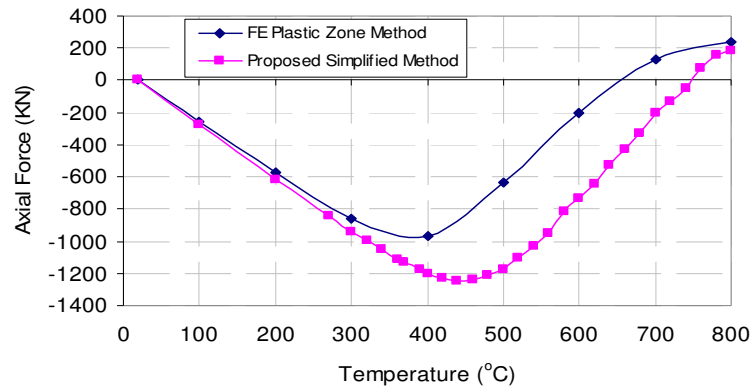


Figure 7.16 Axial force of 8 m steel beam at elevated temperature

### 7.5 Conclusion

An approximate method is introduced to estimate the axial restraint of a beam subjected to a local fire. Comparison with the unit-load method shows that this method can be used to estimate the axial boundary restraints of a beam in a frame structure, and the relative difference between the approximate method and the unit-load method is within 22%.

The structural behavior of a restrained steel beam at elevated temperature is investigated using nonlinear 3-D finite element analysis. The analysis shows that the yield zones of the beam under the combined gravity and temperature load are different from the plastic hinges developed due to bending moment at room temperature. A simplified beam model with pseudo rotational springs is proposed. The change of stiffness of three pseudo rotational springs in the beam model is related to the yielding index of the beam sections at these locations. The simplified beam model can be used in engineering practice to predict the structural performance of a

steel beam in a frame structure, and it can greatly dispense with computational efforts which are ineluctable in the finite element plastic zone method. Beam shortening due to transverse deflection is also considered when the transverse deflection is large as often observed in structures subjected to fire. Catenary action of the beam obtained by using the simplified beam model compares well with the results of a 3-D nonlinear finite element analysis.

## Chapter 8: Conclusions and future work

### 8.1 Conclusions

Techniques to simulate insulated steel structural testing in fire by using small-scale models are explored. Scale modeling offers an economical way of testing that can reveal the behavior of structures in a fire. The scaling rules for designing scaled compartment fires, structures with structural loading and insulation materials on structures are developed and presented. The proposed scaling rules are validated by both the numerical simulations and experiments. The following conclusions can be made from this research:

- The time scale ( $t \sim s^{1/2}$ ) is an appropriate and fundamental scaling relation for developing scaling rules involved in fire phenomena.
- Based on the time scale ( $t \sim s^{1/2}$ ), the proposed scaling rules for designing openly packed wood cribs and determining compartment boundaries are validated by tests of wood cribs burning in enclosures at two scales (1/8-scale and 1/4-scale). Results from the two scaled models compare well, and that indicates that the strategy of partially scaling used in the research is appropriate and effective. Similar hot gas temperature profiles can be obtained from the compartment fires at different scales.
- The theory of structural scaling holds true at elevated temperature if the same material is used in both the prototype and models. Structural strain at high

temperature can be simulated by conducting small-scale tests in a controlled high temperature environment.

- The practical approaches for insulation scaling proposed in this dissertation are validated by both the numerical simulations and experiments. The approach in which only the insulation thickness needs to be adjusted is the easiest one to be used in practice. Satisfactory results are obtained from the scaled tests by using this approach to maintain the similar thermal response in scaled models as that of the prototype. Moreover, the results show that the relative difference of the steel temperature is within the difference of the fire temperature.
- The tests of insulated steel frames in scaled compartment fires show the similar steel temperature profiles and structural deformations. This offers an economical way of testing that can reveal the behavior of spatial steel structures in a fire.
- The testing of steel beams in scaled fires shows that it is feasible to use small-scale models to predict fire-induced failures. The failure temperatures compare well and the relative difference is within 3%. The relative difference of the failure time is approximately 50%. Although the results are not quantitatively perfect, the failure mode, failure time and temperature, and failure mechanism in a small-scale model can represent those of the prototype.
- The test of the small-scale floor model of the World Trade Center Tower 1 demonstrates the use of scaled models to investigate a real-world fire disaster. This study helps engineers and researchers build a better understanding of the fire behavior and the associated structural response in the WTC1, and more convincing collapse hypothesis can therefore be pursued

- A beam model with translational and rotational springs is proposed, and it can be used to simulate the nonlinear behavior in a beam that yields as a result of the combination of mechanical and fire loadings. This beam model allows the user to study the load-temperature-deflection behavior of the steel beams considerably simpler than the traditional finite element (FE) plastic zone method.

## 8.2 Suggestion on future work

- The fire-induced structural performance is sensitive to the temperature. The accuracy of fire scaling becomes crucial in order to predict the structural behaviors accurately. Research on improving the accuracy of the techniques of conducting scaled fires is necessary.
- Physical modeling can differentiate global failure and local failure. Scale testing of complex structures (other than individual member testing) designed to simulate both local and global failures will be desirable.
- The fire boundaries (*e.g.* ventilation) and structural boundaries (*e.g.* damage of bracing and connecting members) change dynamically during a fire. These effects should be considered in order to model a real fire disaster more accurately.
- Research on scale modeling of more structural types (*e.g.* concrete, timber, and masonry) exposed to fire should be conducted.
- Scale testing of some fire-induced phenomena (*e.g.* concrete spalling, fire-induced local failure) will be valuable because current computational tools do not model those phenomena accurately.

- Scale testing of structures in furnace requires research on both scaling theory and experimental validation.

## Bibliography

- [1] FEMA, *World Trade Center Building Performance Study: Data Collection, Preliminary Observations, and Recommendations*, in *FEMA 403*, T. McAllister, Editor. 2002, Federal Emergency Management Agency: Washington D.C.
- [2] D. B Moore. *Full Scale Fire Tests on Complete Buildings*. in *Proceedings of 2nd Cardington Conference*. 1996. Garston, U.K.
- [3] G.M. Newman, J.T. Robinson, and C.G. Bailey, *Fire Safe Design: A New Approach to Multi-Storey Steel-Framed Buildings*, in *SCI Publication P288*. 2000, The Steel Construction Institute.
- [4] B.R. Kirby, *The behaviour of a multi-storey steel framed building subject to fire attack - Experimental data*. 1998, British Steel Swindon Technology Centre, United Kingdom.
- [5] T. Lennon and D. Moore, "The natural fire safety concept - full-scale tests at Cardington," *Fire Safety Journal*, 2003. **38**: p. 623-643.
- [6] P.J. Moss and G.C. Clifton, "Modeling of the Cardington LBTF steel frame building fire tests," *Fire and Materials*, 2004. **28**: p. 177-198.
- [7] *Behaviour of steel framed structures under fire conditions*. PIT Project Main Report. 2000, Edinburgh: School of Civil & Environmental Engineering, The University of Edinburgh.
- [8] Y.C. Wang, "An analysis of the global structural behaviour of the Cardington steel-framed building during the two BRE fire tests," *Engineering Structures*, 2000. **22**: p. 401-412.
- [9] M. Gillie, A.S. Usmani, and J.M. Rotter, "A structural analysis of the first Cardington test " *Journal of Constructional Steel Research*, 2001. **57**: p. 581-601.
- [10] M. Gillie, A.S. Usmani, and J.M. Rotter, "A structural analysis of the Cardington British Steel Corner Test," *Journal of Constructional Steel Research*, 2002. **58**: p. 427-442.
- [11] A.S. Usmani and S. Lamont, "Key Events in the Structural Response of a Composite Steel Frame Structure in Fire," *Fire and Materials*, 2004. **28**: p. 281-297.
- [12] B. Zhao and J. Kruppa, "Structural behaviour of an open car park under real fire scenarios," *Fire and Materials*, 2004. **28**: p. 269-280.
- [13] ASTM, *Standard test methods for fire tests of building construction and materials*. E119-05. 2005: American Society for Testing and Materials.
- [14] Inc. ANSYS, "<http://www.ansys.com>."
- [15] K. McGrattan and G. Forney, *Fire Dynamics Simulator (Version 4) User's Guide*, *NIST Special Publication 1019*, ([http://fire.nist.gov/fds/docs/fds\\_users\\_guide\\_4.pdf](http://fire.nist.gov/fds/docs/fds_users_guide_4.pdf)). 2006, Fire Research Division, National Institute of Standards and Technology.
- [16] C. Bilello, L.A. Bergman, and D. Kuchma, "Experimental investigation of a small-scale bridge model under a moving mass," *Journal of Structural Engineering*, 2004. **130(5)**: p. 799-804.

- [17] D.J. O' Connor, G.W.H. Silcock, and B. Morris, "Furnace Heat Transfer Processes Applied to a Strategy for the Fire Testing of Reduced Scale Structural Models," *Fire Safety Journal*, 1996. **27**: p. 1-22.
- [18] R.J. Fay. *Scale Model Tests of Vehicle Motions*. in *International Congress and Exposition*. 1993. Detroit, MI, USA SAE Special Publications.
- [19] B.J. Wallace and H. Krawinkler, "Small-scale Model Tests of Structural Steel Assemblies," *Journal of Structural Engineering*, 1989. **115(8)**: p. 1999-2015.
- [20] ASCE Aerospace Division Task Committee on Wind Tunnel Studies of Buildings and Structures, "Wind-Tunnel Studies of Buildings and Structures," *Journal of Aerospace Engineering*, 1996. **9(1)**: p. 19-36.
- [21] M. Wang, P.C. Chang, and J. G. Quintiere. *Scale Modeling of Insulated Steel Framed Structural Testing in Fire*. in *Proceeding of The 4th International Workshop Structures in Fire (SiF'06)*. 2006. Aveiro, Portugal.
- [22] B. Samali, K.C.S. Kwok, G.S. Wood, and J.N. Yang, "Wind Tunnel Tests for Wind-Excited Benchmark Building," *Journal of Engineering Mechanics*, 2004. **130(4)**: p. 447-450.
- [23] J. Zhou, G. Lin, T. Zhu, A.D. Jefferson, and F.W. Williams, "Experimental investigation into seismic failure of high arch dams," *Journal of Structural Engineering*, 2000. **126(8)**: p. 926-935.
- [24] E. Buckingham, "On physically similar systems; Illustrations of the use of dimensional equations," *Physical Review*, 1914(4): p. 345-376.
- [25] V. Hogg and B.S. Choo, "A study of scale effects in masonry arch bridges: is testing of large-scale structures still necessary?," *The Structural Engineer*, 2000. **78(5)**: p. 24-29.
- [26] A. Raman and M. Annamalai, "Structural scale modeling in buckling," *Computers & Structures*, 1988. **28(2)**: p. 201-205.
- [27] D. Vassalos, "Physical modelling and similitude of marine structures," *Ocean Engineering*, 1999. **26**: p. 111-123.
- [28] V. Ungbhakorn and P. Singhatanadgid, "Similitude and physical modeling for buckling and vibration of symmetric cross-ply laminated circular cylindrical shells," *Journal of Composite Materials*, 2003. **37(19)**: p. 1697-1716.
- [29] J.J. Wu, "The complete-similitude scale models for predicting the vibration characteristics of the elastically restrained flat plates subjected to dynamic loads," *Journal of Sound and Vibration*, 2003. **268**: p. 1041-1053.
- [30] A.N. Dancygier, "Quantitative evaluation of effect of gravity on small-scale modeling," *Journal of Engineering Mechanics*, 1995. **121(7)**: p. 773-778.
- [31] Inc. ABAQUS, "<http://www.hks.com>."
- [32] Z. Huang, I.W. Burgess, and R.J. Plank, "Nonlinear Analysis of Reinforced Concrete Slabs Subjected to Fire," *ACI Structural Journal*, 1999. **96**: p. 127-135.
- [33] Vulcan Solutions Limited, "<http://www.vulcan-solutions.com>."
- [34] D.I. Nwosu, V.K.R. Kodue, J.M. Franssen, and J.K. Hum, *User Manual for SAFIR: A Computer Program for Analysis of Structures at Elevated Temperature Conditions*, in *Internal Report 782*. 1999, Institute for Research in Construction, National Research Council of Canada.

- [35] J.M. Franssen, V.K.R. Kodur, and J. Mason, *User's manual for SAFIR: a computer program for analysis of structures submitted to fire, Internal Report SPEC/2000\_03*. 2000: University of Liege, Belgium.
- [36] A.S. Usmani, J.M. Rotter, S. Lamont, A.M. Sanad, and M. Gillie, "Fundamental Principles of Structural Behaviour under Thermal Effects," *Fire Safety Journal* 2001. **36**: p. 721-744.
- [37] A.M. Sanad, S. Lamont, A. S. Usmani, and J.M. Rotter, "Structural behaviour in fire compartment under different heating regimes - Part 1 (slab thermal gradients)," *Fire Safety Journal*, 2000. **35**: p. 99-116.
- [38] A.M. Sanad, S. Lamont, A. S. Usmani, and J.M. Rotter, "Structural behaviour in fire compartment under different heating regimes - part 2: (slab mean temperatures)," *Fire Safety Journal*, 2000. **35**: p. 117-130.
- [39] C.G. Bailey, "Membrane action of slab/beam composite floor systems in fire," *Engineering Structures*, 2004. **26**: p. 1691-1703.
- [40] Y.C. Wang and V.K.R. Kodur, "Research toward use of unprotected steel structures," *Journal of Structural Engineering*, 2000. **126(12)**: p. 1442-1450.
- [41] C. Wastney, *Performance of unprotected steel and composite steel frames exposed to fire*, in *Department of Civil Engineering*. 2002, University of Canterbury: Christchurch.
- [42] J.T. Gerlich, P.C.R. Collier, and A.H. Buchanan, "Design of light steel-framed walls for fire resistance," *Fire and Materials*, 1996. **20**: p. 79-96.
- [43] J. Ding, G.Q. Li, and Y. Sakumoto, "Parametric studies on fire resistance of fire-resistant steel members," *Journal of Constructional Steel Research*, 2004. **60**: p. 1007-1027.
- [44] T.C.H. Liu, M.K. Fahad, and J.M. Davies, "Experimental investigation of behaviour of axially restrained steel beams in fire," *Journal of Constructional Steel Research*, 2002. **58**: p. 1211-1230.
- [45] K.C. Yang, S.J. Chen, C.C. Lin, and H.H. Lee, "Experimental study on local buckling of fire-resisting steel columns under fire load," *Journal of Constructional Steel Research*, 2005. **61**: p. 553-565.
- [46] M. Sarraj, I.W. Burgess, J.B. Davison, and R.J. Plank. *Finite element modeling of fin plate steel connections in fire*. in *Fourth International Workshop Structures In Fire "SiF06"*. 2006. Aveiro, Portugal.
- [47] G.B. Lou and G.Q. Li. *Nonlinear finite element modeling of behavior of extended end-plate bolted moment connections in fire*. in *Fourth International Workshop Structures In Fires "SiF06"*. 2006. Aveiro, Portugal.
- [48] G.Q. Li and S.C. Jiang, "Prediction to nonlinear behavior of steel frames subjected to fire," *Fire Safety Journal*, 1999. **32**: p. 347-368.
- [49] A. Landesmann, E.M. Batista, and J.L.D. Alves, "Implementation of advanced analysis method for steel-framed structures under fire conditions," *Fire Safety Journal*, 2005. **40**: p. 339-366.
- [50] Richard J.Y. Liew and K.Y. Ma, "Advanced analysis of 3D steel framework exposed to compartment fire," *Fire and Materials*, 2004. **28**: p. 253-267.
- [51] K.Y. Ma and Richard J.Y. Liew, "nonlinear plastic hinge analysis of three-dimensional steel frames in fire," *Journal of Structural Engineering*, 2004. **130(7)**: p. 981-990.

- [52] C.K. Iu, S.L. Chan, and X.X. Zha, "Nonlinear pre-fire and post-fire analysis of steel frames," *Engineering Structures*, 2005. **27**: p. 1689-1702.
- [53] K.H. Tan and Z.F. Huang, "Structural responses of axially restrained steel beams with semirigid moment connection in fire," *Journal of Structural Engineering*, 2005. **131(4)**: p. 541-551.
- [54] Z.F. Huang and K.H. Tan, "Analytical fire resistance of axially restrained steel columns," *Journal of Structural Engineering*, 2003. **129(1)**: p. 1531-1537.
- [55] L.A. Bisby, M.F. Green, and V.K.R. Kodur, "Modeling the behavior of fiber reinforced polymer-confined concrete columns exposed to fire," *Journal of Composites for Construction*, 2005. **9(1)**: p. 15-24.
- [56] L. Lim, A.H. Buchanan, and P.J. Moss, "Restraint of fire-exposed concrete floor systems," *Fire and Materials*, 2004. **28**: p. 95-125.
- [57] A.M. Sanad, J.M. Rotter, A. S. Usmani, and M.A. O' Connor, "Composite beams in large buildings under fire - numerical modelling and structural behaviour," *Fire Safety Journal*, 2000. **35**: p. 165-188.
- [58] Z. Huang, I.W. Burgess, and R.J. Plank, "Non-linear structural modelling of a fire test subject to high restraint," *Fire Safety Journal*, 2001. **36**: p. 795-814.
- [59] Z.C. Ma and P. Makelainen, "Behaviour of composite slim floor structures in fire," *Journal of Structural Engineering*, 2000. **126(7)**: p. 830-837.
- [60] A. Nadjai, M. O'Garra, F.A. Ali, and D. Laverty, "A numerical model for the behaviour of masonry under elevated temperatures," *Fire and Materials*, 2003. **27**: p. 163-182.
- [61] F. Block, I.W. Burgess, J.B. Davison, and R.J. Plank. *The development of a component-based connection element for endplate connections in fire*. in *Fourth International Workshop Structures In Fire (SiF06)*. 2006. Aveiro, Portugal.
- [62] Y.Z. Yin and Y.C. Wang, "Analysis of catenary action in steel beams using a simplified hand calculation method, Part 1: theory and validation for uniform temperature distribution," *Journal of Constructional Steel Research*, 2005. **61**: p. 183-211.
- [63] Y.Z. Yin and Y.C. Wang, "Analysis of catenary action in steel beams using a simplified hand calculation method, Part 2: validation for non-uniform temperature distribution," *Journal of Constructional Steel Research*, 2005. **61**: p. 213-234.
- [64] T.T. Lie, *Fire temperature-time relations*. SFPE handbook of fire protection engineering, 2nd Edition. . 1995: Society of Fire Protection Engineers, USA.
- [65] C.R. Barnett, "BFD curve: a new empirical model for fire compartment temperatures," *Fire Safety Journal*, 2002. **37**: p. 437-463.
- [66] DD ENV 1991-2-2, *Eurocode 1: basis of design and actions on structures: Part 2.2 actions on structures exposed to fire*. 1996: British Standards Institution.
- [67] J.A. Milke, "Analytical methods to evaluate fire resistance of structural members," *Journal of Structural Engineering*, 1999. **125(10)**: p. 1179-1187.
- [68] U. Wickstrom, "Heat transfer by radiation and convection in fire testing," *Fire and Materials*, 2004. **28**: p. 411-415.

- [69] S. Lamont, A. S. Usmani, and D.D. Drysdale, "Heat transfer analysis of the composite slab in the Cardington frame fire tests," *Fire Safety Journal*, 2001. **36**: p. 815-839.
- [70] H.C. Huang and A. S. Usmani, *Finite element analysis for heat transfer, 1st Edition*. 1994, Berlin: Springer.
- [71] M.B. Wong and J.I. Ghajel, "Sensitivity analysis of heat transfer formulations for insulated structural steel components," *Fire Safety Journal*, 2003. **38**: p. 187-201.
- [72] Z.H. Wang and K.H. Tan, "Sensitivity study of time delay coefficient of heat transfer formulations for insulated steel members exposed to fire," *Fire Safety Journal*, 2006. **41(1)**: p. 31-38.
- [73] Y.C. Wang, "Composite beams with partial fire protection," *Fire Safety Journal*, 1998. **30**: p. 315-332.
- [74] U. Wickstrom and E. Hadziselimovic, "Equivalent concrete layer thickness of a fire protection insulation layer," *Fire Safety Journal*, 1996. **26**: p. 295-302.
- [75] E. Sterner and U. Wickstrom, *TASEF: temperature analysis of structures exposed to fire - user's manual*. 1990, Boras: SP Report.
- [76] N.L. Ryder, S.D. Wolin, and J.A. Milke, "An investigation of the reduction in fire resistance of steel columns caused by loss of spray-applied fire protection," *Journal of Fire Protection Engineering*, 2002. **12**: p. 31-44.
- [77] R.H. Iding, Z. Nizamuddin, and B. Bresler, *FIRES-T3 A Computer Program for the Fire Response of Structures – Thermal (Three-Dimensional Version)*, in *NIST-GCR-95-682*. 1977, National Institute of Standards and Technology: Gaithersburg, MD. Issued June 1996.
- [78] S. Lamont, A. S. Usmani, and M. Gillie, "Behaviour of a small composite steel frame structure in a "long-cool" and a "short-hot" fire," *Fire Safety Journal*, 2004. **39(5)**: p. 327-357.
- [79] NIST, *Final Report on the Collapse of the World Trade Center Towers, (NIST NCSTAR 1) Federal Building and Fire Safety Investigation of the World Trade Center Disaster*. 2005, National Institute of Standards and Technology.
- [80] A. F. Gross and D. Robertson, "Experimental Fires in Enclosures," *Combustion Institute Symposium on Combustion*, 1965: p. 931-942
- [81] G. Heskestad, "Modeling of Enclosure Fires," *Journal of Fire and Flammability*, 1975. **6(3)**: p. 253-273.
- [82] J.A. Block. *A theoretical and experimental study of nonpropagating free-burning fires*. in *Proceedings of the 13th Symposium on Combustion*. 1971: The Combustion Institute.
- [83] P. A. Croce, *Modeling of Vented Enclosure Fire Part 1. Quasi-Steady Wood-Crib Source Fire*. 1978, Norwood, Massachusetts: Factory Mutual Research Corporation.
- [84] P.A. Croce and Y. Xin, "Scale Modeling of Quasi-steady Wood Crib Fires in Enclosures," *Fire Safety Journal*, 2005. **40**: p. 245-266.
- [85] J.G. Quintiere, *Fundamentals of Fire Phenomena*. 2006: John Wiley & Sons, Inc.

- [86] T.Z. Harmathy, *Properties of building materials at elevated temperatures*. 1983, National Research Council of Canada, Division of Building Research: Ottawa, Canada.
- [87] J. A. Perricone, *Scale Modeling of the Transient Behavior of Wood Crib Fires in Enclosures*, MS thesis. 2005, University of Maryland.
- [88] P.H. Thomas and J.M. Heselden, *C.I.B. International Co-operative Programme on Fully-Developed Fires in Single Compartment: Comprehensive Analysis of Results*.
- [89] <<http://www.unifrax.com>> Unifrax Corporation.
- [90] Thermal Ceramics, [www.thermalceramics.com](http://www.thermalceramics.com).
- [91] P.S. Veloo, *Scale Modeling of the Transient Behavior of Heat Flux in Enclosure Fires*, MS thesis. 2006, University of Maryland: College Park.
- [92] G. Su, J. G. Quintiere, and N. Schultz. *Physical scaling of fire suppression by water mist*. in *ASME International Mechanical Engineering Congress and Exposition*. 2001. New York, NY.
- [93] P.J. Moss, A.H. Buchanan, J. Seputro, C. Wastney, and R. Welsh, "Effect of support conditions on the fire behaviour of steel composite beams," *Fire and Materials*, 2004. **28(2-4)**: p. 159-175.
- [94] E.H. Jr. Gaylord, C.N. Gaylord, and J.E. Stallmeyer, *Design of steel structures*. 1992: McGraw-Hill, Inc.
- [95] Z. P. Bažant and Y. Zhou, "Why did the World Trade Center collapse?--- Simple Analysis," *Journal of Engineering Mechanics*, 2002. **128(1)**: p. 2-6.
- [96] Z. P. Bažant and Y. Zhou, "Addendum to 'Why did the World Trade Center collapse?---Simple Analysis'," *Journal of Engineering Mechanics*, 2002. **128(3)**: p. 369-370.
- [97] J.G. Quintiere, M. di Marzo, and R. Becker, "A suggested cause of the fire-induced collapse of the World Trade Towers," *Fire Safety Journal* 2002. **37** p. 707-716.
- [98] Abolhassan Astabeh-Asl. *World Trade Center Collapse, Field Investigations and Analyses*. in *9th Arab Structural Engineering Conference*. 2003. Abu Dhabi, UAE.
- [99] A.S. Usmani, Y.C. Chung, and J.L. Torero, "How did the WTC towers collapse: a new theory," *Fire Safety Journal* 2003. **38** p. 501-533.
- [100] A.S. Usmani, "Stability of the World Trade Center Twin Towers Structural Frame in Multiple Floor Fires," *Journal of Engineering Mechanics*, 2005. **131(6)**: p. 654-657.
- [101] J.G. Quintiere. *A predicted timeline of failure for the WTC towers*. in *InterFlam, 10th International Fire Science & Engineering Conference*. 2004. Edinburgh, Scotland.
- [102] K. Stewart, *Analysis of the Fuel Load Calculations for the 96<sup>th</sup> Floor of the WTC North Tower: Private Discussion and Report for Dr. J.G. Quintiere*. 2005, Department of Fire Protection Engineering, University of Maryland College Park.
- [103] F.P. Incropera and D.P. DeWitt, *Fundamentals of Heat and Mass Transfer, 5th Edition*. 2001: John Wiley & Sons Inc.

- [104] Y.Z. Yin and Y.C. Wang, "A numerical study of large deflection behaviour of restrained steel beams at elevated temperatures," *Journal of Constructional Steel Research*, 2004. **60**: p. 1029-1047.
- [105] G.Q. Li and S.X. Guo. *Analysis of restrained steel beams subjected to temperature increasing and decreasing*. in *The third international symposium on steel structures*. 2005. Korea.
- [106] F. Al-Mashary and W.F. Chen, "Simplified second-order inelastic analysis for steel frames," *The Structural Engineer*, 1991. **69(23)**: p. 395-399.
- [107] W.F. Chen and S.L. Chan, "Second-order inelastic analysis of steel frames using element with midspan and end springs," *Journal of Structural Engineering*, 1995. **121**: p. 530-541.